2022

An Investigation into the Plate Fixation for Periprosthetic Femoral Fractures

Xiang Chen
University of Denver

An Investigation into the Plate Fixation for Periprosthetic Femoral Fractures

Abstract

Periprosthetic femoral fractures are the third most reason for reoperation after the total hip arthroplasty with an incident rate of approximately 6%. The Vancouver type B periprosthetic femoral fractures account for over 70% of all cases, while the sub-type B1 fracture (when the total hip stem is stable) has remained a clinical challenge due to incidences of severe complications after the standard plate-screw fixation. To seek biomechanically sound fixations for the Vancouver type B1 fracture, this dissertation developed a combined modeling and testing framework to investigate the efficacy of fixation for a Vancouver type B1 fracture using different construct lengths and different plating systems. Specifically, the coupled musculoskeletal and finite element model of total hip stem and plate implanted femurs were developed to simulate the physiological bone strain and the plate stress under loads of common activities of daily living. The modeling results were shown to be able to effectively evaluate and compare the mechanics of different plating systems and construct lengths but were also able to shed light on the mechanisms of mechanical pathogenesis of PFFs. The models also showed good fidelity in predictions of bone strain and bone remodeling stimuli as compared with the previous clinical and biomechanical studies. The results of the coupled models were used as a basis for developing several new mechanical tests, which were shown to match the simulated physiological bone strain and plate stress in the coupled musculoskeletal and finite element models.

Document Type

Dissertation

Degree Name

Ph.D.

Department

Mechanical Engineering

First Advisor

Paul J. Rullkoetter

Second Advisor

Schuyler van Engelenburg

Third Advisor

Peter Laz

Keywords

Biomechanics, Total hip arthroplasty, Femoral fracture, Vancouver type B1 fracture

Subject Categories

Biomechanics and Biotransport | Biomedical Engineering and Bioengineering

An Investigation into the Plate Fixation for Periprosthetic Femoral Fractures

---

A Dissertation

Presented to

the Faculty of the Daniel Felix Ritchie School of Engineering and Computer Science

University of Denver

In Partial Fulfillment

of the Requirements for the Degree

Doctor of Philosophy

---

by

Xiang Chen

November 2022

Advisor: Paul J. Rullkoetter

Author: Xiang Chen
Title: An Investigation into the Plate Fixation for Periprosthetic Femoral Fractures
Advisor: Paul J. Rullkoetter
Degree Date: November 2022

ABSTRACT

Periprosthetic femoral fractures are the third most reason for reoperation after the total hip arthroplasty with an incident rate of approximately 6%. The Vancouver type B periprosthetic femoral fractures account for over 70% of all cases, while the sub-type B1 fracture (when the total hip stem is stable) has remained a clinical challenge due to incidences of severe complications after the standard plate-screw fixation. To seek biomechanically sound fixations for the Vancouver type B1 fracture, this dissertation developed a combined modeling and testing framework to investigate the efficacy of fixation for a Vancouver type B1 fracture using different construct lengths and different plating systems. Specifically, the coupled musculoskeletal and finite element model of total hip stem and plate implanted femurs were developed to simulate the physiological bone strain and the plate stress under loads of common activities of daily living. The modeling results were shown to be able to effectively evaluate and compare the mechanics of different plating systems and construct lengths but were also able to shed light on the mechanisms of mechanical pathogenesis of PFFs. The models also showed good fidelity in predictions of bone strain and bone remodeling stimuli as compared with the previous clinical and biomechanical studies. The results of the coupled models were used as a basis for developing several new mechanical tests, which were shown to match the simulated physiological bone strain and plate stress in the coupled musculoskeletal and finite element models.

ACKNOWLEDGMENTS

First and foremost, I would like to thank Dr. Rullkoetter for his continuous support, his crucial advice, and his constant help during the four years of my study. I would like to thank Dr. Chadd Clary for his advice and help in both the experimental and the modeling studies of my thesis. I would like to thank Dr. Peter Laz for his support and advice, and the knowledge and optimization techniques that were taught in his courses, which were applied in the studies of this thesis. I would like to thank Dr. Casey Myers for his advice and support, as well as his original work on motion analysis and musculoskeletal modeling of THA patients, whose data was used as a basis for studies in this thesis. I would like to thank Thor Andreassen for his help and involvement during both experimental testing and manuscript drafting. I would like to thank Brittany Marshall for her help during preliminary experimental testing. I would like to thank my peer students Mohsen Sharifi Renani, William Burton, and Gary Doan for their help and support during my studies.

I would like to thank the support from DePuy Synthes throughout the projects of my study. Especially, I want to thank Bryan Fritz for his continuous coordination, support, and involvement in all the studies. I would like to thank Ryan DeWall for his involvement in the experimental testing and his help during the drafting of manuscripts for this thesis. I would like to thank Dr. Dana Coombs for his support and advice throughout the drafting of manuscripts in my thesis. I would like to thank Dr. Michael Blauth for his surgical help during experimental testing and his advice in manuscript drafting. I would like to thank Michael Brace for his advice during manuscript drafting. I would like to thank my parents for their constant support not only during my studies, but also throughout my life.

TABLE OF CONTENTS

LIST OF TABLES

LIST OF FIGURES

CHAPTER ONE. THE CLINICAL RAMIFICATIONS OF PERIPROSTHETIC FEMORAL FRACTURES AFTER A TOTAL HIP ARTHROPLASTY

1.1 BACKGROUND

Periprosthetic femoral fractures (PFFs) are severe complications after a total hip arthroplasty (THA). PFF is the third most frequent reason for reoperation after a THA (Abdel et al., 2016). Incidences of PFFs after a THA have been continuously rising during the past two decades (Miettinen et al. reported a 3-fold increase of surgically treated PFFs) and are expected to keep increasing in the future (Abdel et al., 2016; Miettinen et al., 2021). The increased rate of PFFs has been associated with the increased usage of cementless THA stems and a higher level of post-operational activity in THA patients (Abdel et al., 2016; Lindahl et al., 2006; Miettinen et al., 2021). To help determine appropriate treatment, PFFs are typically classified using the Vancouver classification system based on the location of the fracture (Fig. 1.1) (Marsland and Mears, 2012). The Vancouver type B PFFs are the fractures located around or just beneath the tip of the implanted THA stem, which account for over 70% of all PFF cases (Abdel et al., 2016; Laurer et al., 2011; Marsland and Mears, 2012). If the type B fracture is concomitant with a loose THA stem, it is categorized as B2 or B3 fracture, which often requires a revision of the loosened stem with a longer stem (Abdel et al., 2016; Laurer et al., 2011; Marsland and Mears, 2012). Type

B1 PFFs are those with a well-fixed stem, therefore the standard treatment is Open Reduction and Internal fixation (ORIF) (Laurer et al., 2011). Implantation of a periprosthetic plate-screw construct can preserve the stem, therefore stem revision is not necessary. This thesis will focus on the investigation of the mechanical mechanisms that may cause type B1 PFFs, and the fixation mechanics of type B1 PFF.

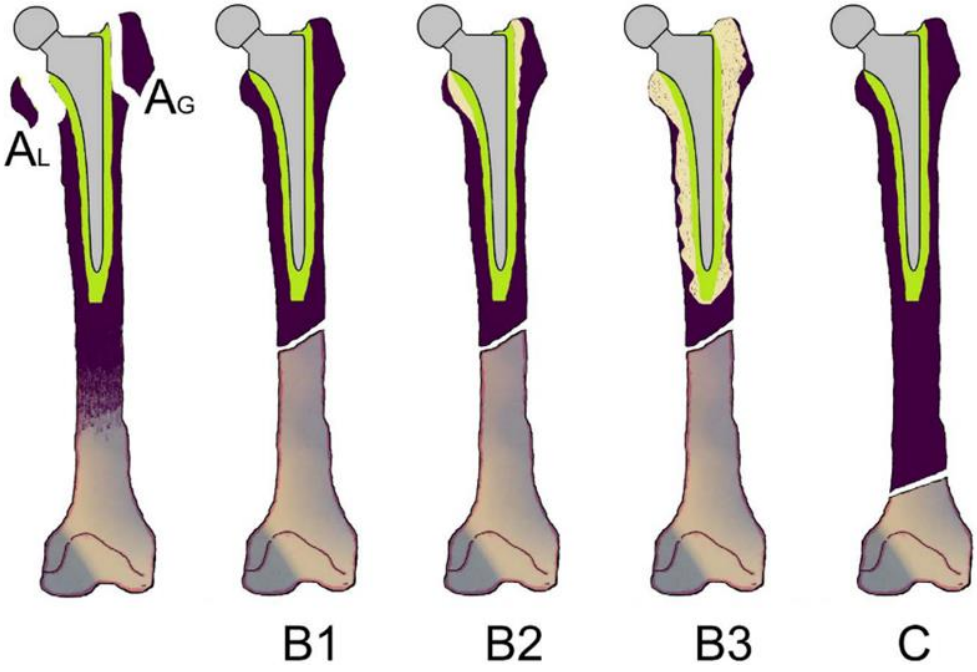

Fig. 1.1. Vancouver classification of PFFs based on locations of fracture (Marsland and Mears, 2012).

Trauma has been reported to cause a majority of cases of type B1 PFFs. Notably, over 75% of the type B1 PFFs were due to a low-energy trauma, such as a fall from a standing height (Abdel et al., 2016; Miettinen et al., 2021). Furthermore, over 20% of B1 PFFs were nontraumatic stress fractures (Abdel et al., 2016). High incidences of low-energy fractures and nontraumatic stress fractures are clear indications that bone strength may play a key

role in the pathogenesis of type B1 PFFs (Giovanni et al., 2020a; Randelli et al., 2018). Patients with osteoporosis account for over 25% of all THA patients, osteoporosis has been associated with increased risks of fractures (Franklin and Malchau, 2007). Clinically, the high prevalence of stress fracture has been associated with the recently increased usage of uncemented THA stems (Abdel et al., 2016; Marsland and Mears, 2012; Miettinen et al., 2021). Meanwhile, incidences of nontraumatic stress fractures may indicate that physiological loads during activities of daily living (ADLs) may reach the critical level to initiate microcracks and later develop into stress fractures. Due to degraded bone strength, patients with osteoporosis may be prone to stress fractures (Franklin and Malchau, 2007; Glowacki et al., 2003; Karachalios et al., 2020; Labuda et al., 2008; Mäkinen et al., 2007; Reid, 2020; Sidler-Maier and Waddell, 2015).

Though the stress/state of the bone-implant system may be used to assess the risks of PFFs, it is inherently difficult to measure the *in vivo* stress/strain state of the bone-implant system. Finite element (FE) models have been increasingly used to estimate the stress and strain in bone and implant (Chen et al., 2022b, 2022a, 2021; Moazen et al., 2011; Speirs et al., 2007a; Wang et al., 2019). Especially, the coupled musculoskeletal and FE models enable the simulation of physiological muscle forces, thereby have become a useful tool for the simulation of loading of ADLs (gait, stair-climbing, stair-descent, etc.) in both native and THA-implanted femurs (Chen et al., 2022b, 2022a, 2021; Duda et al., 1998; Kersh et al., 2018; Speirs et al., 2007b). However, modeling studies of osteoporotic femurs are limited, and information on the mechanics of THA-implanted osteoporotic femurs is lacking.

The efficacy of plate fixation for type B1 PFFs has been studied extensively. To date, fixation using a laterally implanted locking compression plate has been proven to be successful surgery to promote the healing of type B1 PFFs (Bryant et al., 2009; Moazen et al., 2014; Moloney et al., 2014). Fixation using a locking compression plate can minimize bone-plate contact by maintaining the bone-plate distance via locking screws, thereby minimizing damage to the periosteum which could promote callus formation and fracture healing.

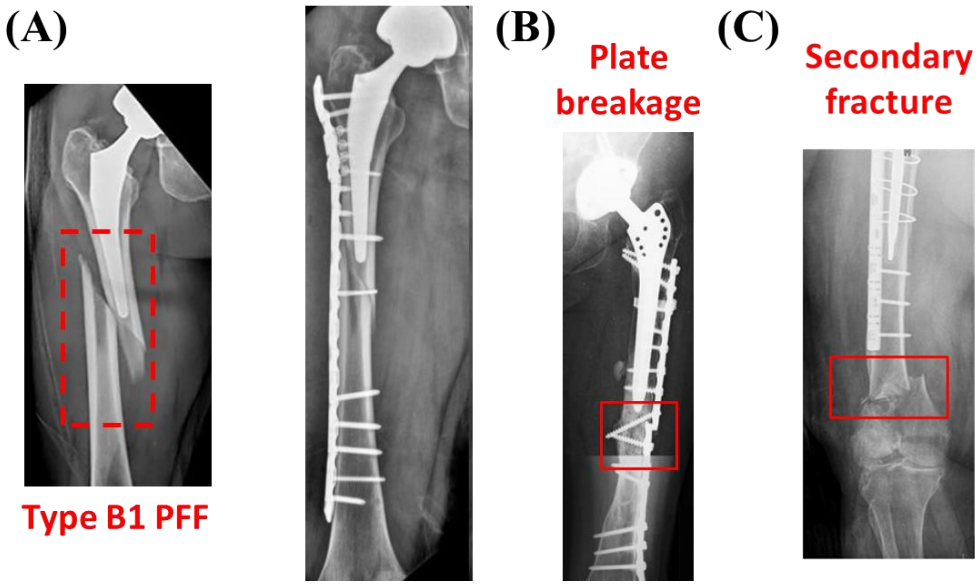

Fig. 1.2. Fixation of the Vancouver type B1 fracture and its complications (plate breakage and secondary femoral fracture). **(A)** Type B1 fracture and the fixation of the fracture using a diaphyseal construct. **(B)** Plate breakage after the plate fixation. **(C)** Secondary femoral refracture distal to the previously implanted diaphyseal plate.

However, the prognosis of plate fixation for type B1 PFF has been hindered by several severe complications. The overall rate of complication ranged from 15.6 to 33.9% after the

plate fixation for type B1 PFF with approximately 59% of the failures requiring revision surgeries (Abdel et al., 2016; Lindahl et al., 2006). Catastrophic failures of plate fixation, including femoral refracture and plate breakage, not only require complex reoperation to fix but also are associated with an increased rate of disability (residual limping) and mortality (Abdel et al., 2016; Lindahl et al., 2007).

Femoral refracture has been reported to be the second most prevalent complication of plate fixation for type B1 PFF. Causes of femoral refractures are multifactorial, including patients' demographic factors (sex, age, weight, level of activities, bone health, etc.) and more importantly the mechanics of the bone-implant system (Giovanni et al., 2020a; Moazen et al., 2011; Randelli et al., 2018; Wang et al., 2019). If the primary type B1 PFF is successfully healed (fracture union is established), femoral refracture frequently occurs distal to the healed primary PFF and is typically associated with the implantation of a short diaphyseal plate-screw construct (Lindahl et al., 2006; Moloney et al., 2014). Since the shorter diaphyseal plate does not span to the condyle of the femur, the most distal fixation screw is typically located in the distal diaphysis. Previous clinical studies have hypothesized that the most distal screw of the shorter construct may act as a stress riser due to concentrated load transfer through the screw (Bryant et al., 2009; Moloney et al., 2014). However, due to limited understanding of the *in vivo* mechanics of the bone-THA-plate system, further investigation is needed to provide more information on the mechanisms of femoral refractures in the distal femur.

To mitigate the risks of refractures in the distal femur, the longer condyle-spanning construct has been proposed clinically for the fixation of type B1 PFF (Bryant et al., 2009;

Moloney et al., 2014). The condyle-spanning construct spans the full length of the femur with the most distal screws inserted into the lateral condyle. Clinically, longer condyle-spanning constructs have shown promise in lowering the risks of femoral refractures (Bryant et al., 2009; Moloney et al., 2014). It has been hypothesized that the condyle-spanning construct could avoid stress/strain concentration in the bone around and distal to the most distal diaphyseal screw (Bryant et al., 2009; Chen et al., 2022a; Moloney et al., 2014). Nonetheless, understanding is lacking regarding the mechanism of lowered risks of femoral refractures.

Though not as prevalent as femoral refracture, the breakage of the plate is a severe complication that requires complex revision surgery and is associated with a high rate of post-operational morbidity and mortality (Boesmueller et al., 2015; Giovanni et al., 2020a; Randelli et al., 2018). The breakage of the plate may occur both before and after the healing of the type B1 PFF (Boesmueller et al., 2015; Giovanni et al., 2020a; Randelli et al., 2018). The causes of plate breakage are also multifactorial. The injury state of the primary PFF and the *in vivo* biomechanics of the bone-implant system have been proposed to be the leading contributing factors (Giovanni et al., 2020a). Nonunion of the primary PFF has been reported to cause increased risks of plate breakage (Boesmueller et al., 2015; Giovanni et al., 2020a; Randelli et al., 2018). Meanwhile, clinical incidences of plate breakage indicated that the plate does experience failure level load *in vivo* during activities of daily living. However, due to difficulties in direct measurements, the *in vivo* loading and the performance of the plate, including plate stress and the resultant moment and force in the plate have not been comprehensively investigated.

Alternatively, several standard mechanical tests have been typically utilized to evaluate the performance of the plate under simplified loads of isolated compression, bending, torsion, as well as combined compression and torsion (Lenz et al., 2016b, 2016a; Lever et al., 2010; Moazen et al., 2014, 2013). However, due to the lack of information on the *in vivo* biomechanics of the plate evidence is lacking to show the standard tests may mimic the effect of *in vivo* loads that the plate may experience.

1.2 OBJECTIVE AND CHAPTER OVERVIEWS

The overarching objective of this thesis is to seek biomechanically sound solutions for the plate fixation of periprosthetic femoral fractures. The biomechanically sound solutions should be able to minimize the risks of catastrophic fixation failures.

Chapter Two developed coupled musculoskeletal and FE models of THA-implanted femurs and simulated physiological loads in three common ADLs. By estimating bone strains, the models were used to evaluate the risks of type B1 PFF in THA-implanted femurs. In addition, based on the simulated strain state of THA implanted femurs, specifically the strain energy density, simplified mechanical tests were developed that were able to match the profile of strain energy density in the femur under ADL loading.

Chapter Three further used coupled musculoskeletal and FE models of THA and plate-implanted femurs to investigate the risks and the mechanisms of plate breakage in femurs either with or without an existing type B1 PFF under simulated loads of three common ADLs. The model predicted plate stress, as well as the resultant moment and force in the plate, were used as the basis to assess whether simplified mechanical tests may reproduce

the plate mechanics resulting from ADL-loading. Models evaluated plate stress and load transfer for both the existing standard test and the newly-developed mechanical test.

Chapter Four used the newly-developed simplified testing configuration in Chapter Two to validate FE models of THA and plate-implanted femurs. The validated femur FE models were then used to evaluate and compare the fixation mechanics of two different plating systems and two different construct lengths (a diaphyseal fixation construct and a condyle-spanning construct) under simulated physiological muscle loads of simulated gait. Specifically, the risks of femoral refractures, occurring most frequently around the most distal diaphyseal screw or just below the end of a short diaphyseal construct, were assessed based on estimated bone strains.

Chapter Five applied a similar strategy in chapter 4 to assess the fixation mechanics of the plating construct in osteoporotic femurs under simulated loads of three common ADLs. The resulting bone strain, plate stress, load transfer, and local stiffness were compared between models of healthy and osteoporotic femurs. In addition, osteoporosis-associated muscle weakening was simulated in FE models of osteoporotic femurs to investigate the impact of varied muscle forces on the fixation mechanics of plating construct in osteoporotic femurs.

Chapter Six summarized the current understandings of the mechanics of plate fixation for type B1 PFF, and proposed future directions for both mechanical and modeling studies that would further the process of seeking biomechanically sound solutions for plate fixations of type B1 PFFs.

CHAPTER TWO. MECHANICS OF THA-IMPLANTED FEMUR IN ADLS AND THE DEVELOPMENT OF PHYSIOLOGICAL STRAIN STATE BASED MECHANICAL TESTS

2.1 INTRODUCTION

As the total amount of THA patients rises continuously, cases of PFFs are expected to rise in the foreseeable future (Abdel et al., 2016; Marsland and Mears, 2012; Miettinen et al., 2021). The increased usage of uncemented THA femoral components in recent years has been associated with increased incidences of post-THA PFFs (Abdel et al., 2016; Lindahl et al., 2007; Miettinen et al., 2021).

The magnitude and distribution of principal strains in periprosthetic bone have been demonstrated to be indicators of the risk of bone fractures. Though it is difficult to measure *in vivo* bone strains, FE models have been proven to be an effective tool for the prediction of bone strains. Especially, the coupled musculoskeletal and FE model has enabled the simulation of physiological joint contact force and muscle forces during ADLs. Several previous studies have used the coupled musculoskeletal and FE model to simulate gait-loading in both intact and THA-implanted femurs to estimate the risks of femoral fractures and PFFs (Edwards et al., 2016; Speirs et al., 2007; Taylor et al., 1996). Nevertheless, information is lacking on the state of post-THA femoral strains during other activities.

Due to the difficulties in experimental replication of the complex muscle loads, validation of the coupled musculoskeletal and FE models against biomechanical testing is lacking. Post-THA changes in strain energy density (SED) have been identified to be the mechanical stimuli for bone remodeling (Lerch et al., 2012; Szwedowski et al., 2012). Using the coupled musculoskeletal and FE models of THA-implanted femurs, good agreement was achieved between the model-estimated bone remodeling stimuli and radiographic measurements of periprosthetic bone remodeling (Lerch et al., 2012; Szwedowski et al., 2012).

Simplified cadaveric tests have also been developed to assess the mechanical impact of THA or fixation hardware on bone mechanics (Moazen et al., 2011; Wang et al., 2018). FE models of those standard tests have also been developed and increasingly utilized to improve the efficiency in implant development. Though the simplified loadings were typically developed based upon *in vivo* hip contact force and hip moment (Bergmann et al., 2001), contributions of the complex muscle forces have rarely been considered. Moreover, previous modeling studies have shown the importance of properly distributed muscle forces on the fidelity of predicting physiological femoral strains as compared with using simplified loads in standard tests (Lerch et al., 2012; Speirs et al., 2007; Taylor et al., 1996). Thus far, no study has shown whether simplified loading configurations used in mechanical tests may simulate the femoral strain states seen in ADL loads.

The objectives of this chapter are two folds: first, to investigate the biomechanical mechanisms of PFFs by evaluating the strain state of THA implanted femurs; second, to investigate whether simplified mechanical tests derived from a FE integrated optimization

approach may replicate the state of femoral strains seen under different ADL loads. Coupled musculoskeletal and FE models were developed for three cadaveric femurs, while loads of three common ADLs (gait, stair-descent, and sit-to-stand) were simulated to evaluate the strain state of THA-implanted femurs. Models of THA-implanted femurs were used to verify the fidelity of FE models by comparing the calculated post-THA bone remodeling stimuli with the reported clinically measured radiographic bone remodeling. Specimen-specific axial compression and combined compression and torsion tests were then developed for each ADL via best matching the SED profile of the THA-implanted femur under ADL loads. The fidelity of the compression and combined compression and torsion models was further assessed by 1) comparing the model-estimated periprosthetic bone remodeling stimuli with the corresponding ADL-loading model; 2) comparing the model-predicted bone fatigue regions with the corresponding ADL model.

2.2 MATERIALS AND METHODS

2.2.1 SPECIMEN PREPARATION AND THA IMPLANTATION

Three fresh frozen cadaveric specimens of lower extremity (all right limbs, all males, 69.7 ± 7.4 years old, 173.6 ± 1.2 centimeters, 71.1 ± 13.5 kilograms) were CT scanned (slice thickness 0.6 mm and pixel size 0.5 mm, SIEMENS, Munich, Germany) with a density phantom (QCT Pro, Mindways Software, Inc., Austin TX, USA). Each femur was dissected of soft tissues and was physically implanted with a commercially-available cementless femoral stem and a 32-mm-diameter femoral head (SUMMIT®, Depuy) by an orthopaedic surgeon. To determine the positions of the THA component relative to each

femur, surfaces of the femur, the THA stem and head were digitized as point clouds using a 3D optical motion capture system (Optotrak Certus, Northern Digital, Waterloo, Canada).

2.2.2 FINITE ELEMENT MODELING

FE models of the intact and the THA-implanted femur were developed using the segmented femur geometries from the CT scans (ScanIP, Synopsys, Mountain View, CA, USA). Models of the physically implanted THA stem and femoral head were virtually implanted into each femur model in Solidworks (Dassault Systèmes, Vélizy-Villacoublay, France). To replicate the *in situ* implant position in the physical specimen, the implant models were aligned to the femur model based on the positions of digitized point clouds using a rigid iterative closest point algorithm in Matlab (MathWorks, Natick, MA, USA).

The intact and implanted femur models were imported into Abaqus 2018 (Dassault Systèmes, Vélizy-Villacoublay, France), where geometries were meshed using 10-noded tetrahedral elements. A preliminary mesh convergence study was performed to determine an average edge length of 2.5 mm for the femur to be optimal for both converged strain prediction and computational cost. The interfaces between stem and bone, as well as stem and femoral head, were modeled as fully bonded to simulate idealized load transfer.

The apparent density of the bony materials was interpolated from CT Hounsfield units (HUs) using the CT density phantom (Eq. 1-3) (Schileo et al., 2008). Note the coefficients of coversion between HU and bone mineral density (Eq. 1) was specimen specific, since each specimen was CT scanned with the density phantom. Young's moduli of bony materials were calculated from apparent density using an established relationship (Eq. 4)

(Morgan et al., 2003). Material assignment was performed in Bonemat software (Taddei et al., 2007). Each femur model contained approximately 400 bony materials with Young's moduli ranging from approximately 10 MPa to over 18,000 MPa in 50 MPa intervals. The Poisson's ratio for all bony materials was set to be 0.3 (Morgan et al., 2003). The implanted cobalt chrome THA stem and femoral head were modeled as linear elastic materials with a Young's modulus of 210,000 MPa and a Poisson's ratio of 0.29.

$$\text{Bone Mineral Density } (\text{g/cm}^3) = -0.02184 + 0.8242 * \text{HUs} \quad \text{Eq. 1}$$

$$\text{Ash Density } (\text{g/cm}^3) = 0.8772 * \text{Bone Mineral Density} + 0.07895 \quad \text{Eq. 2}$$

$$\text{Apparent Density } (\text{g/cm}^3) = \text{Ash Density} / 0.6 \quad \text{Eq. 3}$$

$$\text{Young's modulus (MPa)} = 6850 * \text{Apparent Density}^{1.49} \quad \text{Eq. 4}$$

2.2.3 ADL-LOADING FE MODELS

Peak hip contact forces and corresponding femoral muscle forces during gait, stair-descent and sit-to-stand were calculated using one of the lower extremity musculoskeletal models that were originally developed for THA patients that had participated in a laboratory testing session (Myers et al., 2018). Specifically, peak forces during gait were taken at the point of contralateral toe-off (approximately 25% of the stance phase) (Myers et al., 2018). Before applying to the FE models, the muscle forces and hip joint contact forces were scaled by a factor determined by the difference in body weight (BW) between each cadaveric specimen and the original THA patient from the lab. A subset of muscle forces (larger than 50 N, approximately 7.5% BW) were applied to the FE models to reduce the complexity in model development and simulation. Compared with the model using all

the muscle forces, a preliminary study showed that applying the subset of muscle forces had negligible effect on femoral strain.

In both the intact and the THA-implanted models, muscle forces were modeled as distributed loads applied over designated surface areas of muscle insertions (Fig. 2.1). The locations of muscle insertions were estimated from the musculoskeletal model (Myers et al., 2018). To avoid stress concentration, an elliptical insertion area was defined for each muscle centered at its insertion point (Speirs et al., 2007). In the intact femur models, the peak hip contact force was modeled as a distributed load over a surface region on the femoral head to avoid large stress caused by concentrated point load. The surface region was centered at the projected point of the hip contact force vector on the intact femoral head. Since hip contact forces were different in different ADLs, the surface region was redefined for each ADL. In the THA-implanted models, the hip contact force was applied through the center of the femoral head (Fig. 2.1). All translations were constrained for the surface nodes of the femoral condyles (Fig. 2.1). Anterior/posterior translation was fixed for the surface nodes in the articulating region of the patellofemoral joint (Fig. 2.1).

It was initially observed that the intact and THA FE models estimated unrealistic level of femoral deflection (> 10 mm) when applying the musculoskeletal model originally predicted hip contact and muscle forces during gait and stair-descent. An unphysiological femoral deflection has also been reported by other investigators while using model-predicted hip contact and muscle forces directly as input for FE models (Speirs et al., 2007). To limit the femoral deflection to a reported physiological range (< 5 mm, Taylor et al., 1996) muscle forces were adjusted using an iterative optimization approach integrated with

the FE models while maintaining the moment about the hip. This approach resulted in additional co-contractions of the important antagonistic muscles.

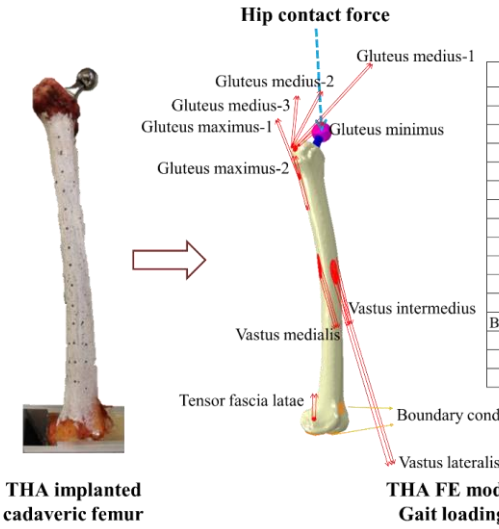

Force (percentage BW)			
	Gait	Stair-descent	Sit-to-stand
Hip contact force	269%	320%	111%
Gluteus medius - 1	77%	109%	nan
Gluteus medius - 2	39%	nan	nan
Gluteus medius - 3	39%	nan	nan
Gluteus maximus -1	33%	84%	10%
Gluteus maximus -2	8%	nan	38%
Gluteus minimus	16%	11%	nan
Vastus laterlis	97%	91%	130%
Vastus intermedius	23%	22%	20%
Vastus medialis	29%	27%	31%
Tensor fascia latae	13%	nan	nan
Biceps femoris short head	nan	56%	nan
Adductor longus	nan	27%	44%
Illiacus	nan	45%	10%
Psoas	nan	50%	nan

Fig. 2.1. Coupled musculoskeletal and FE model of a THA-implanted cadaveric femur. The THA-implanted FE model replicated the *in situ* position of the femoral component in the physically-implanted specimen. Muscle forces were applied to FE models as distributed loads over designated muscle insertion areas (ellipsoids in red) on the surface of the femur model. Directions of muscle forces were obtained from the musculoskeletal model. Lengths of plotted muscle vectors were proportional to the magnitude of muscle forces.

In the gait FE model, gluteus maximus 1 and 2 were activated more by 16% and 7% BW, respectively. Meanwhile, the vastus lateralis was activated more by 30% BW. Simulation of peak loads in stair-descent required adjustment of forces in gluteus medius, adductor longus and vastus lateralis muscles (increased by 21%, 12% and 15% BW, respectively). In the sit-to-stand FE model, forces in gluteus maximus and vastus lateralis were increased by 8% and 12% BW, respectively. The adjusted muscle forces were

comparable to the literature reported muscle forces in the three ADLs (Bitsako et al., 2005; Correa et al., 2010; Duda et al., 1996; Myers et al., 2018; Taylor et al., 1996; Verdonschot et al., 2001). SED, as well as maximum and minimum principal strains in the femur were calculated using the intact and the THA-implanted FE models.

In the THA-implanted ADL-loading models, the mean SED values in bony elements were calculated in 30 consecutive cross-sectional volumes (10-mm-interval) along the diaphysis of the femur (Fig. 2.2). For each ADL-loading model, FE models of axial compression and combined axial compression and torsion tests were developed to match the SED profile of the THA-implanted femur.

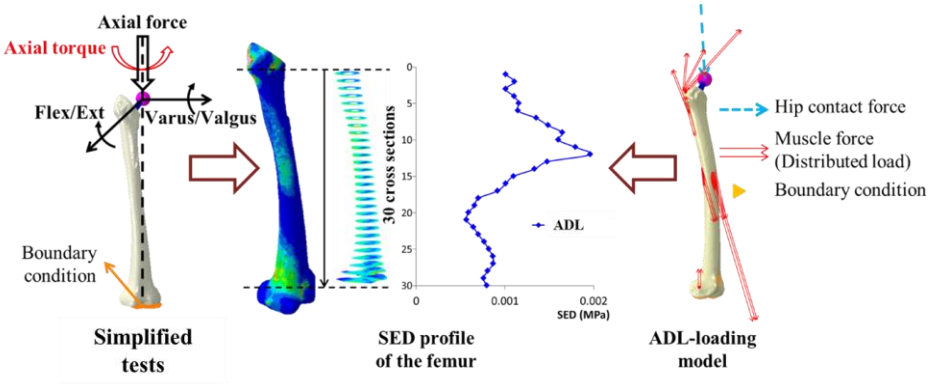

Fig. 2.2. Development of axial compression and combined axial compression and torque tests (simplified tests, left) to match the SED profile of the femur (middle) in the corresponding ADL-loading model (right).

2.2.4 DEVELOPMENT OF AXIAL COMPRESSION AND COMBINED AXIAL COMPRESSION AND TORSION TESTS USING FE MODELS

An iterative optimization approach was developed to adjust the configurations of axial compression and combined axial compression and torsion tests to match the femoral SED

profile of the corresponding ADL-loading FE model. Three loading configurations were optimized for the axial compression test: the magnitude of the axial force, and flexion/extension and varus/valgus angles of the femur as mounted in a test frame (Fig. 2.2). Development of the combined axial compression and torsion test included an axial torque, while maintaining the axial compression and the alignment of the femur the same as the optimized axial compression test (Fig. 2.2). As mounted in a test frame, the axial compression was applied through the center of the femoral head in a vertical direction after the femur was aligned in desired angles (Fig. 2.2). The axial torque was applied about the same vertical axis (Fig. 2.2). The minimum increment for the iterative optimization of flexion/extension and varus/valgus angles was 0.1°. The minimum increments for the axial compression and the axial torque in the optimization procedure were 100 N and 1 Nm, respectively. To simulate the boundary condition of the femur as mounted in a test frame, the distal femur was virtually resected just proximal to the distal end of the femoral condyles. All translations of nodes in the resection plane were constrained (Fig. 2.2). The percentage error in SED was calculated in each cross-sectional volume between each simplified-loading FE model (axial compression or combined axial compression and torsion) and the corresponding ADL-loading model (Fig. 2.2). Optimization was considered converged when the mean percentage error in SED (over 30 cross sections) reached less than ±5%.

Post-THA bone remodeling stimuli were calculated for the models of optimized axial compression and combined axial compression and torsion and compared with their corresponding ADL-loading model. Post-THA bone remodeling stimulus (ξ) was defined

as the percentage change in SED per unit mass (Eq. 5) in periprosthetic bone elements as compared with the intact femur (Eq. 6) (Lerch et al., 2012). Calculated bone remodeling stimuli were distinguished into stimulus for bone resorption ($\xi \leq -75\%$), no change ($-75\% < \xi < 75\%$), bone formation ($\xi \geq 75\%$), and overloading (bone necrosis, $\xi \geq 400\%$) (Lerch et al., 2012). Distributions of predicted bone remodeling stimuli were described using Gruen zones and compared with other modeling and clinical studies (Brodner et al., 2004; Lerch et al., 2012; Panisello et al., 2006).

$$S = \frac{SED}{\rho\_app} \quad \text{Eq. 5}$$

$$\xi = \frac{S_{THA} - S_{intact}}{S_{intact}} \times 100\% \quad \text{Eq. 6}$$

Based on the reported fatigue thresholds in maximum principal strain and minimum principal strain (2500 με and -4000 με, respectively, Pattin et al., 1996), fatigue regions were identified as bone elements that experienced principal strains beyond those thresholds. Prevalence of fatigue regions were assessed in simplified-loading models and compared with the corresponding ADL-loading model for each specimen.

2.3 RESULTS

2.3.1 SIMULATIONS OF PHYSIOLOGICAL STRAIN STATE OF THA-IMPLANTED FEMURS

Applying appropriately distributed muscle forces, the ADL-loading intact and THA-implanted FE models predicted physiological levels of femoral deflection across all three ADLs (Table 2.1). In ADL-loading models, specimens A and B consistently showed bone resorption stimuli in Gruen zones 1, 2, 6 and 7, whereas bone formation stimuli were

predominantly observed in the proximal aspect of Gruen zone 1 and in Gruen zone 3 (Fig. 2.3B). In contrast to specimens A and B, ADL-loading models of specimen C did not show bone resorption stimuli in Gruen zone 5 (Fig. 2.3B). Under gait and stair-descent loads, specimen C showed bone formation stimuli in Gruen zones 1, 2, 6 and 7 adjacent to the stem, where bone resorption stimuli were observed in specimens A and B (Fig. 2.3B).

ADL	Peak hip contact force (%BW)	Model	Peak deflection (mm)
Gait	269%	Intact	3.6 ± 0.5
		THA	1.6 ± 0.3
Stair-descent	320%	Intact	4.7 ± 0.2
		THA	3.5 ± 0.4
Sit-to-stand	111%	Intact	2.7 ± 0.1
		THA	2.6 ± 0.3

Table 2.1. The ADL-loading intact and THA-implanted FE models predicted physiological levels of femur deflection across three simulated ADL loads in three specimens.

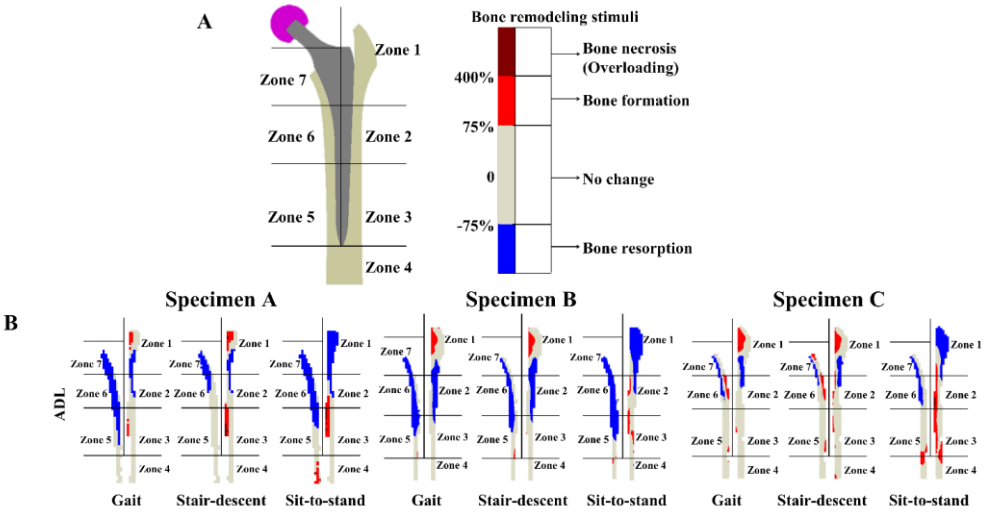

Fig. 2.3. Simulated bone remodeling stimuli under simulated loads of three common ADLs. **(A)** Locations of Gruen zones and the colormap of bone remodeling stimuli. **(B)** Estimations of bone remodeling stimuli in different ADLs.

Bone elements experiencing strains beyond fatigue thresholds (2500 με in maximum principal strain and -4000 με in minimum principal strain) were observed in all three specimens during stair-descent, and in specimens B and C during gait (Fig. 2.4). Observed fatigue regions located around and adjacent to the tip of the implanted stem (Fig. 2.4). Those locations were consistent with the site of Vancouver type B periprosthetic femoral fractures (Laurer et al., 2011).

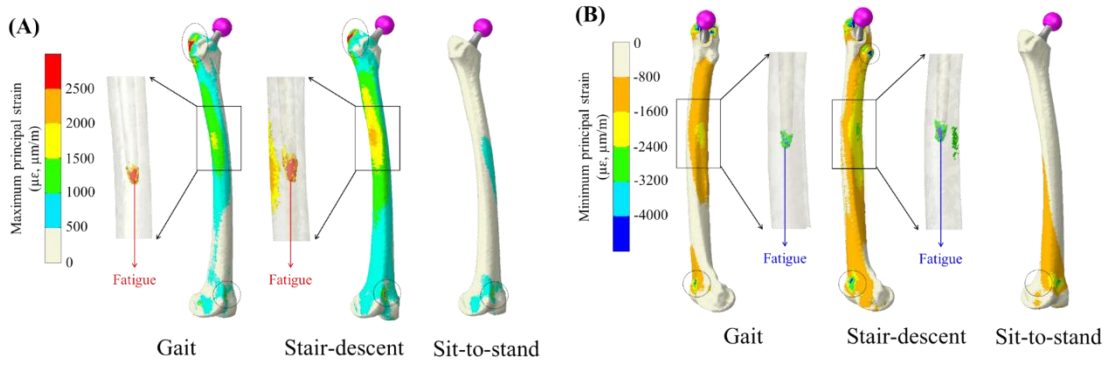

Fig. 2.4. Maximum and minimum principal strains in specimen B under simulated loads of three ADLs. Bone elements experiencing higher than 1500 με in maximum principal strain **(A)**, and lower than -2400 με in minimum principal strain **(B)** were isolated and plotted. Note that concentrated strains in proximal and distal aspects of the ADL-loading femurs (inside dashed black ellipsoids) were caused by either the application of muscle forces or the definition of boundary condition.

2.3.2 DEVELOPMENT OF AXIAL COMPRESSION AND COMBINED AXIAL COMPRESSION AND TORSION TESTS USING FE MODELS BASED ON ADL-LOADING MODELS

The optimized loading configurations for axial compression and combined axial compression and torsion tests were summarized in Table 2.2. For instance, the gait-loading based axial compression test included a compressive force of 293 ± 8% BW, and a femur alignment in 3.7 ± 0.4° extension and 2.3 ± 0.3° varus (Fig. 2.5, Table 2.2). The combined axial compression and torsion test introduced an additional 4.3 ± 1.2 Nm internal torque (Fig. 2.5). The SED profile calculated by the optimized simplified-loading models matched well with the gait-loading model (Fig. 2.5). The mean percentage error in SED profile as compared with the gait-loading model was -3.2 ± 0.9% for the axial compression model, while the combined axial compression and torsion model further reduced the mean percentage error to -0.6 ± 1.0% (Fig. 2.6). In stair-descent, optimized simplified-loading models (Table 2.2) resulted in mean percentage errors of -2.1 ± 1.6% and -0.6 ± 0.9%, respectively (Fig. 2.6). The sit-to-stand loading based tests (Table 2.2) showed mean percentage errors of -1.3 ± 1.5% and 0.0 ± 0.3%, respectively (Fig. 2.6).

ADL	Axial compression			Combined axial compression and torque
	Flexion (+)/ extension (-) (°)	Valgus (+)/ varus (-) (°)	Axial force (%BW)	Axial torque (internal +, external -; Nm)
Gait	3.7 ± 0.4	-2.3 ± 0.3	293 ± 8%	4.3 ± 1.2
Stair-descent	3.6 ± 0.2	-1.8 ± 0.2	460 ± 33%	6.0 ± 0.8
Sit-to-stand	5.0 ± 0.7	-5.2 ± 0.5	164 ± 14%	0.3 ± 1.9

Table 2.2. Optimized loading configurations for axial compression and combined axial compression and torque tests based on three ADLs.

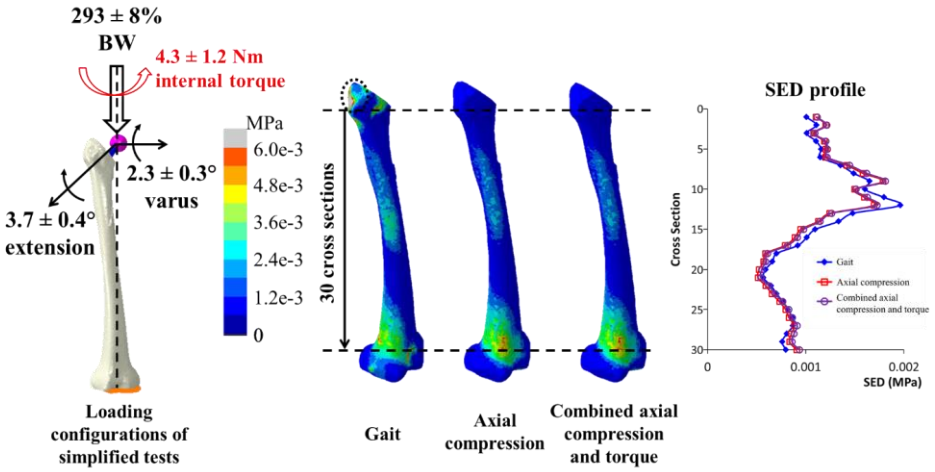

Fig. 2.5. Comparisons of SED profile between gait-loading model and models of simplified mechanical tests. The SED profile calculated by the axial compression and combined axial compression and torque FE models closely matched the SED profile as seen in the gait FE model. Mean values of optimized loading configurations for axial compression and combined axial compression and torque tests were shown, while SED profiles were plotted for models of specimen A. Note that concentrated SED in proximal femur (inside dashed black ellipsoid) was caused by application of muscle forces.

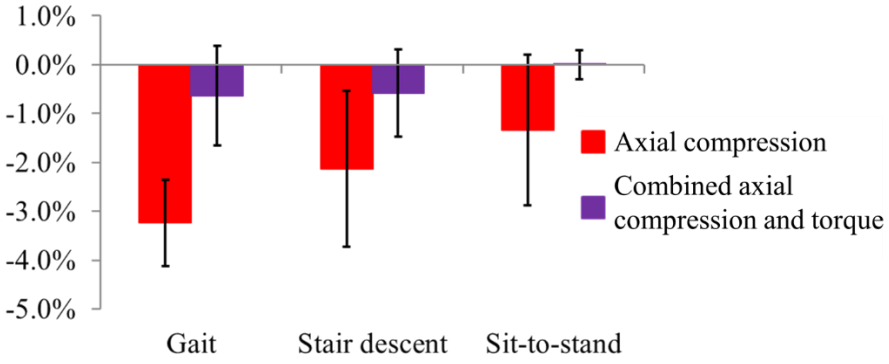

Fig. 2.6. Mean percentage errors in SED profile of optimized axial compression and combined axial compression and torque FE models as compared with gait, stair-descent, and sit-to-stand models.

2.3.3 VERIFICATION OF SIMPLIFIED-LOADING MODELS

Under loads of gait and stair-descent, axial compression and combined axial compression and torsion tests of specimens A and B generally agreed with ADL models in predictions of bone remodeling stimuli (Fig. 2.7A and B). Except for the proximal aspect of Gruen zone 1, where simplified-loading models over-estimated bone resorption stimuli by -32.2 ± 8.6% (Fig. 2.7C). Under sit-to-stand load, simplified-loading models of specimens A and B over-estimated bone formation stimuli and overloading in Gruen zones 3, 4 and 5 (by 57.3% in A and 49.6% in B; Fig. 2.7C), while under-estimated bone resorption stimuli in the lateral aspect of zone 4 (-15.5% in A and -20.8% in B; Fig. 2.7C). Similar to specimens A and B, simplified-loading models of specimen C showed good agreement with ADL models in simulations of gait and stair-descent, except for the over-estimated bone resorption stimuli in Gruen zone 1 (by -30.2%; Fig. 2.7C). Simplified-loading models of specimen C also over-estimated bone formation and overloading in sit-to-stand (by 70.4%; Fig. 2.7C).

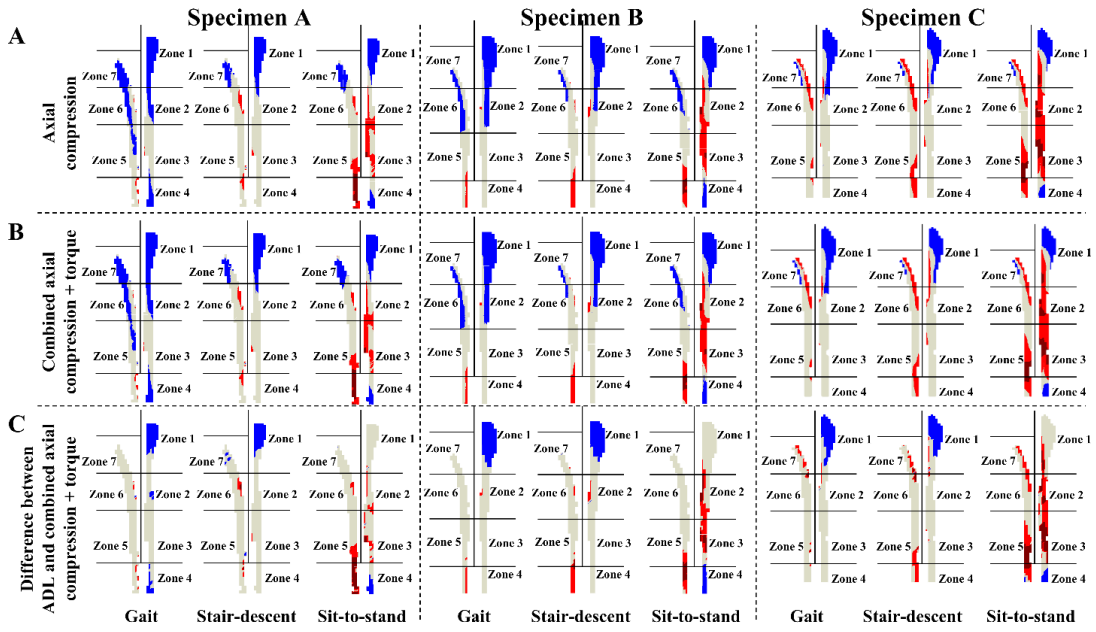

Fig. 2.7. Comparisons of bone remodeling stimuli in models of simplified mechanical tests. Estimated bone remodeling stimuli were compared between axial compression **(A)** and combined axial compression and torsion **(B)** models. Differences in estimated bone remodeling stimuli **(C)** were calculated between combined axial compression and torque and ADL-loading models.

Simplified-loading models of three specimens estimated similar fatigue regions as compared with their corresponding ADL-loading models (Fig. 2.8A and B). However, simplified-loading models over-estimated volumes of fatigue regions in both maximum and minimum principal strains (Fig. 2.8C and D).

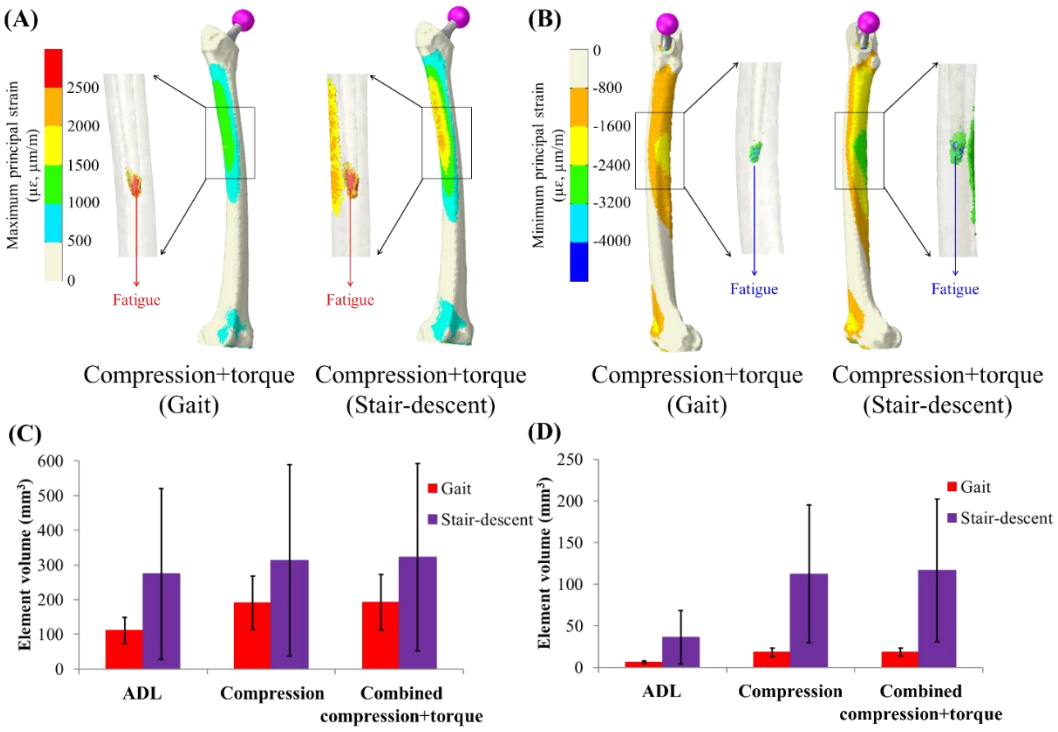

Fig. 2.8. Estimated bone fatigue regions and the volume of fatigue elements. Maximum and minimum principal strains in specimen B were shown for the models of combined axial compression and torsion (A and B). Mean volumes of element experiencing higher than fatigue threshold in maximum (C) and minimum (D) principal strains during gait and stair-descent in specimens B and C (specimen A did not show fatigue region under gait loads). Fatigue thresholds were 2500 με in maximum principal strain and -4000 με in minimum principal strain (Pattin et al., 1996).

2.4 DISCUSSION

Using appropriately distributed muscle forces, ADL-loading models developed in this study predicted physiological patterns of remodeling stimuli in the periprosthetic bone as compared with clinical observations (Bitsakos et al., 2005; Brodner et al., 2004; Lerch et

al., 2012; Panisello et al., 2006; Szwedowski et al., 2012). The proximally located bone resorption stimuli were consistent with clinically reported regions of stress shielding observed around cementless THA stems (Brodner et al., 2004; Panisello et al., 2006). During stair-descent and sit-to-stand, bone formation stimuli observed in Gruen zones 3 and 4 were consistent with the reported periprosthetic site showing postoperative increases in bone mineral density (Brodner et al., 2004; Panisello et al., 2006).

Fatigue regions were observed in periprosthetic bone in specimens B and C when applying simulated loads of gait and stair-descent. The fatigue regions contained concentrated bone elements that showed bone strains above the fatigue thresholds in either maximum or minimum principal strains. The estimated fatigue regions were consistent with the frequently reported locations for Vancouver type B1 PFFs. Previous FE modeling studies typically evaluated gait loads, however, the results of our study demonstrated that evaluating a composite of ADLs may provide more comprehensive information on the biomechanics in THA-implanted femurs.

This study successfully developed axial compression and combined axial compression and torsion tests for three common ADLs using an FE-integrated optimization approach via matching the femoral SED profile in THA-implanted models of three specimens. FE models of optimized axial compression and combined axial compression and torsion tests showed good agreement in predicting bone remodeling stimuli and fatigue regions as compared with ADL-loading models and literature results (Bitsakos et al., 2005; Brodner et al., 2004; Laurer et al., 2011; Lerch et al., 2012; Panisello et al., 2006; Szwedowski et al., 2012).

Optimized axial compression and combined axial compression and torsion tests generally achieved good agreement with ADL loading models in predicting bone remodeling stimuli. The most noticeable differences between simplified-loading models and their corresponding ADL-loading models were observed during sit-to-stand. Simplified-loading models consistently overestimated bone formation stimuli and overloading in Gruen zones 3 and 5, and the medial aspect of zone 4, while over-estimated bone resorption stimuli in the lateral aspect of zone 4 (Fig. 2.5D). Forces of vastus muscles were applied through the bone surface located just below the tip of the THA stem in ADL-loading models, while the vastus lateralis force was considerable in the sit-to-stand model (130% BW in vastus lateralis, Fig. 2.1). Simplified-loading models did not capture the effect of vastus muscle forces on bone remodeling stimuli during sit-to-stand. Similarly, simplified-loading models could not capture the effect of high forces in gluteus medius during gait and stair-descent thereby over-estimated bone resorption stimuli in the proximal aspect of Gruen zone 1 (gluteus medius forces were applied at the surface of the proximal aspect of Gruen zone 1, Fig. 2.1). Our findings were consistent with the reported lower bone resorption stimuli observed in the vicinity of muscle insertions (Bitsakos et al., 2005). The good agreement between ADL-loading and simplified-loading models in bone remodeling stimuli predictions in femoral diaphysis (Gruen zones 2, 3, 5, and 6) was the result of a combined effect of applying optimized loading configurations and the lack of impact through large muscle forces in the vicinity.

Though the FE model predicted bone remodeling stimuli agreed with clinical findings, varied distributions of bone remodeling stimuli were observed in different specimens.

During the same ADL, specimens A and B showed similar distributions of bone remodeling stimuli (Fig. 2.7). Specimen C showed less bone resorption stimuli in Gruen zone 5, and more bone formation stimuli in elements adjacent to the proximal portion of the stem compared with specimens A and B. Among three specimens, specimen C had the highest body weight of 89.8 kg (specimen A: 64.9 kg; specimen B: 58.5 kg). Specimen C also showed more elements with a bone mineral density close to or higher than 1.8 g/cm3 in Gruen zones 3, 4, and 5 (Fig. 2.9). Though input forces were higher in FE models of specimen C due to its higher body weight, higher bone mineral density resulted in overall higher von Mises stresses and more load transfer to the periprosthetic bone after THA implantation. At a cross-section just below Gruen zones 1 and 7 in the gait-loading model, load transfer through bone was 27% in specimen C compared with a mean of 17% in specimens A and B. More load transfer through periprosthetic bone thereby resulted in higher post-operative SED in bone and increases in bone formation stimuli.

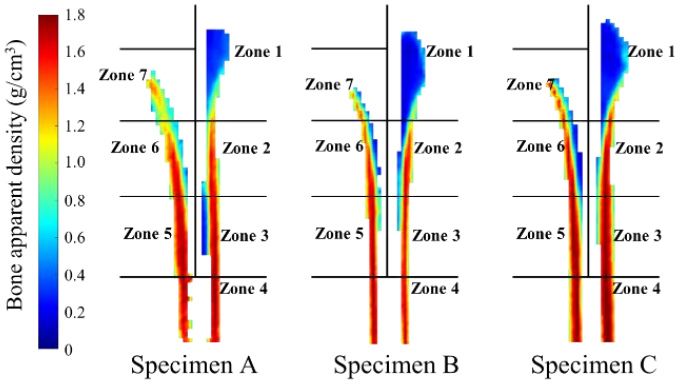

Fig. 2.9. Comparisons of bone mineral density in Gruen zones across three specimens.

The literature data and our results both showed that coupled musculoskeletal and FE models using appropriately distributed muscle forces were able to match patterns of

radiologically measured bone remodeling stimuli. Simplifications of muscle-loading FE models through reducing simulated muscles have been shown to overestimate bone resorption stimuli (Bitsakos et al., 2005). Furthermore, exclusions of certain important muscles without considering the effects of femur alignment and fixation were shown to cause imbalanced bending moment in the femur thereby resulting in higher femoral deflection and principal strains as compared with the complex muscle-loading FE models (Duda et al., 1998; Kersh et al., 2018; Speirs et al., 2007; Taylor et al., 1996). In contrast, the results of our study showed that a comprehensive optimization approach considering both the alignment and the loading of the femur could generate simplified mechanical testing configurations that accurately matched the SED profile of the femur in complex muscle-loading FE models. Due to a lack of *in vivo* data, the model predicted muscle loading, femoral deflection, and femoral principal strains have yet to be directly validated for any study of this type. Through the current study, we hope to establish the basis for a combined modeling and testing platform to better investigate critical factors that may influence femoral strains. Such information will help us and other investigators to design implementable methods for the eventual *in vivo* validation of the model predicted strain/SED.

Limitations in the modeling of muscle forces should be considered. Similar to the common approach reported in the literature, each muscle force was modeled as an evenly distributed surface load following a single vector. Since full muscle geometries were not represented, physiological muscle insertions and intrinsic force distribution within muscle fibers were not considered. Given the demonstrated impact of muscle forces on femoral

deflection and principal strains (Duda et al., 1998; Kersh et al., 2018; Lerch et al., 2012; Speirs et al., 2007; Taylor et al., 1996), as well as the impact on bone remodeling stimuli in the vicinity of muscle insertions (Bitsakos et al., 2005), future FE modeling of realistic 3D muscle geometries and active muscle contractions may better represent the physiological effect of muscle forces. FE modeling of 3D muscle may affect the optimization results of the simplified-loading configurations as described in this study, however, may also provide more insight into the fidelity of both the ADL- and the simplified-loading models. Several other limitations should be considered regarding the scope of our study and the methods used. The optimization utilized the femoral SED profile as the reference during the development of axial compression and combined axial compression and torsion tests. The optimized simplified-loading models all achieved less than ±5% mean percentage errors in the SED profile, but mean percentage errors in principal strains were found to be close to ±15%. Though the simplified-loading models predicted similar fatigue regions as compared with the ADL-loading models, future studies should consider principal strains as well in the optimization objective function to simultaneously achieve a closer fit for the principal strains. The bone-stem interface was modeled as fully bonded to simulate a well-fixed cementless THA stem. Future studies will investigate the impact of contact definitions on femoral strains.

2.5 CONCLUSION

This study successfully developed specimen-specific and ADL-specific axial compression and combined axial compression and torsion loading configurations that are

capable of simulating physiological bone remodeling stimuli and evaluating risks of bone fatigue in three THA-implanted femurs. The physiological-loading-based simplified tests can be readily implemented in vitro to provide a pre-clinical platform for future evaluations of implant/fixation devices for the hip and the femur.

CHAPTER THREE. SIMPLIFIED MECHANICAL TESTS CAN SIMULATE PHYSIOLOGICAL MECHANICS OF A FIXATION CONSTRUCT FOR PERIPROSTHETIC FEMORAL FRACTURES

3.1 INTRODUCTION

Periprosthetic femoral fractures (PFFs) are severe complications after a total hip arthroplasty (THA), and the third most frequent reason for revision surgeries (accounting for approximately 6% of revision cases after a THA) (Lindahl et al., 2006; Marsland and Mears, 2012). The Vancouver type B PFF is a fracture of the femoral shaft around the implanted THA stem or just below the tip of the stem, and accounts for over 70% of all PFF cases (Corten et al., 2009; Lever et al., 2010; Lindahl et al., 2007). When the THA stem is stable (classified as the type B1 fracture), the fracture is typically treated surgically using a laterally-implanted plate-screw construct (Corten et al., 2009; Duncan and Haddad, 2014). Although the fracture fixation constructs have been proven to promote the healing of primary type B1 PFFs, clinically reported fracture of the plate has raised concerns (Boesmueller et al., 2015; Giovanni et al., 2020a; Min et al., 2020; Randelli et al., 2018).

Plate fractures have been reported to occur both before and after the complete healing of the primary PFF (Boesmueller et al., 2015; Giovanni et al., 2020a; Min et al., 2020; Randelli et al., 2018). The reasons for plate fracture are multifactorial, including patient

demographics (Boesmueller et al., 2015; Giovanni et al., 2020a; Randelli et al., 2018), the injury state of the primary PFF (Boesmueller et al., 2015; Giovanni et al., 2020a; Randelli et al., 2018), and perhaps most importantly, the *in vivo* biomechanics of the construct (Giovanni et al., 2020a). Clinical incidences of plate fracture have demonstrated that the PFF fixation construct does experience failure-level loads *in vivo* (Boesmueller et al., 2015; Giovanni et al., 2020a; Min et al., 2020). To evaluate the risks of plate fracture, the ASTM standard test for metallic bone plates is a plate-only 4-point-bend test that is typically used to evaluate the stiffness and the fatigue life of a plate under a concentrated bending moment (ASTM International, 2008; Lenz et al., 2016b, 2016a; Lever et al., 2010). Other experimental and finite element (FE) studies have utilized simplified loads of compression (Lenz et al., 2016b, 2016a; Lever et al., 2010; Moazen et al., 2014, 2013), bending (Choi et al., 2010) and torsion (Choi et al., 2010; Lenz et al., 2016a; Lever et al., 2010) to test THA and plate-implanted cadaveric and synthetic femurs, while the initial stability of fracture fixation, the stiffness of the bone-implant system and the stresses/strains in the plate have been typically measured. Given the flexibility and the efficiency of FE analyses, models have been increasingly used not only for the evaluation of PFF fixation (Moazen et al., 2014, 2013, 2011; Wang et al., 2019) but also for the development of new implant device for PFF fixation (Dhason et al., 2020). However, due to the lack of direct measurement of the physiological conditions in the plate, a consensus is lacking on what testing procedures may best reproduce the *in vivo* plate mechanics (Moazen et al., 2011; Wang et al., 2019).

Though it is difficult to assess the *in vivo* performance of a PFF fixation construct directly, FE models applying joint contact force and muscle forces may provide an alternative for the estimation of the physiological plate mechanics. Coupled musculoskeletal and FE models have shown fidelity in predicting bone strains and bone remodeling stimuli in intact and THA-implanted femurs as compared with *in vivo* measurements (Chen et al., 2021; Duda et al., 1998; Speirs et al., 2007a; Taylor et al., 1996). Through simulating the peak hip contact force and forces of major muscles during gait, femur FE models were successfully utilized to compare different fixation strategies for non-prosthetic related femoral fractures (without an existing THA or other implants) in various regions, including the cervicotrochanteric, the diaphysis and the supracondylar regions (Chantarapanich et al., 2016; Jitprapaikulsarn et al., 2021). However, information on plate mechanics after the PFF fixation remains lacking, especially after the healing of a Vancouver type B1 PFF.

Aiming to further the understanding of plate mechanics, this study utilized coupled musculoskeletal and FE models to simulate hip contact force and muscle forces from three common ADLs in FE models of THA and plate-implanted femurs with an existing or a healed PFF. The simulated plate mechanics provided a basis for the development of appropriate simplified mechanical tests that can mimic the stress state and load transfer in the plate in both PFF and healed models.

3.2 MATERIALS AND METHODS

This study firstly developed FE models of implanted femurs either with a simulated Vancouver type B1 PFF or a completely healed PFF (sections 3.2.1 to 3.2.2). Peak hip contact force and corresponding femoral muscle forces from three common ADLs (gait, stair-descent, and sit-to-stand) were applied to the PFF and the healed models. Based on these ADL simulations, FE models of appropriate simplified mechanical tests were identified or developed to best match the plate mechanics in femur models with a simulated PFF or a healed PFF (sections 3.2.3 to 3.2.5).

3.2.1 FE MODELS TO EVALUATE PLATE STRESSES DURING ADLS

FE models of implanted femurs with both THA and PFF fixation plates were developed from three cadaveric femurs (the same specimens as in Chapter Two: all right limbs, all males, 69.7 ± 7.4 years old, 173.6 ± 1.2 centimeters, 71.1 ± 13.5 kilograms). Each cadaveric femur was CT scanned (0.6-mm slice thickness, 0.5-mm pixel size, SIEMENS, Munich, Germany) with a density phantom (QCT Pro, Mindways Software, Inc., Austin, TX, USA) and was physically implanted with a commercially available cementless THA femoral component (SUMMIT®, DePuy, Warsaw, IN, USA) and a PFF fixation plate-screw construct (Locking Compression Plate System, LCP®, DePuy Synthes, West Chester, PA, USA) by an experienced orthopedic surgeon. The fixation plate spanned from the proximal diaphysis to the lateral condyle of each cadaveric femur. The proximal portion of the plate was overlapping with the implanted THA stem, while the distal portion of the plate was bent and contoured to the shape of the lateral condyle of each femur (Fig. 3.1A).

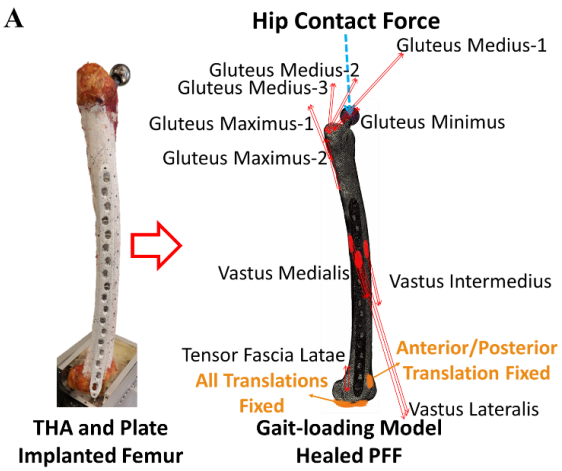

Force (Percentage Body Weight)			
	Gait	Stair-descent	Sit-to-stand
Peak Hip Contact Force	**269%**	**320%**	**111%**
Gluteus Medius – 1	77%	109%	nan
Gluteus Medius – 2	39%	nan	nan
Gluteus Medius – 3	39%	nan	nan
Gluteus Maximus -1	33%	84%	10%
Gluteus Maximus -2	8%	nan	38%
Gluteus Minimus	16%	11%	nan
Vastus Laterlis	97%	91%	130%
Vastus Intermedius	23%	22%	20%
Vastus Medialis	29%	27%	31%
Tensor Fascia Latae	13%	nan	nan
Biceps Femoris Short Head	nan	56%	nan
Adductor Longus	nan	27%	44%
Illiacus	nan	45%	10%
Psoas	nan	50%	nan

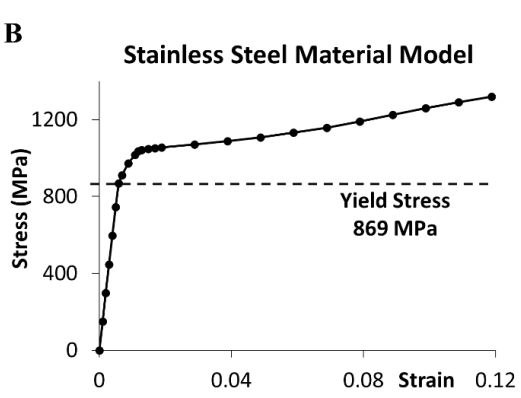

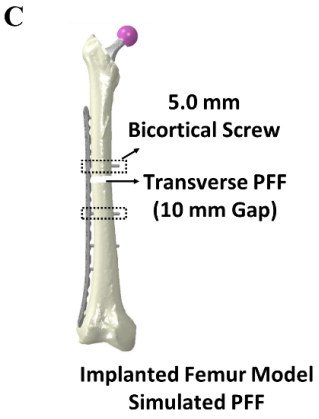

Fig. 3.1. An overview of the healed and the PFF models of a THA and plate implanted cadaveric femur. **(A)** THA and plate implanted femur FE models (simulated a healed PFF) were developed from CT scans of cadaveric specimens. Peak hip contact forces and muscle forces of three ADLs were applied to the implanted femur as distributed loads over elliptical muscle insertions. The denotation of 'nan' meant the specific muscle force was not used in a certain ADL due to the low magnitude (less than 5% body weight). **(B)** The elastic-plastic model of stainless steel. **(C)** A transverse PFF was simulated in the implanted femur model. The simulated PFF was bridged by two 5.0 mm bicortical screws.

The plate was fixed to the femur using seven 5.0 mm locking screws (Fig. 3.1A). The *in situ* positions of the THA stem and plate were determined by digitizing surfaces of the femur, the THA component and the plate as point clouds using a 3D motion capture system (Optotrak Certus, Northern Digital, Waterloo, Canada). Using CT-reconstructed femur geometries and methods described in Chapter Two, FE models of THA and plate-implanted femurs were developed in Abaqus 2018 (Dassault Systèmes, Vélizy-Villacoublay, France) and replicated the *in situ* positions of the implants in physical specimens (Chen et al., 2021).

Briefly, 10-noded tetrahedral elements were used for modeling of the femur, the THA component, the plate and the screws, with mean edge lengths of 2 mm, 2 mm, 1 mm, and 0.5 mm, respectively. A refined edge length of 0.5 mm was used to mesh the local interface between bone and screws. Mean edge lengths were determined from a previous mesh convergence study that showed further decreases in edge length did not result in greater than 5% changes in plate stresses. The mean number of elements of the THA and plate-implanted FE models across three specimens was 842767 ± 29273. The THA and plate-implanted FE model simulated a healed Vancouver type B1 PFF that was reduced to the anatomical alignment in the cadaveric femur.

Bone was modeled as heterogeneous linear elastic materials the same as in Chapter Two with Young's moduli interpolated from CT Hounsfield units using a CT density phantom and established relationships (Eq. 1-4) (Morgan et al., 2003; Schileo et al., 2008). The cobalt-chrome THA stem and femoral head was modeled as linear elastic with a Young's modulus of 210 GPa and a Poisson's ratio of 0.29 (Chen et al., 2021). The stainless steel PFF fixation plate and screws were modeled as elastic-plastic with a Young's modulus of

149 GPa, Poisson's ratio of 0.29, and a yield stress of 869 MPa (Fig. 3.1B) (ASTM F138-13a, 2013). The interface between bone and the cementless THA stem was modeled as fully bonded to represent a well-fixed stem as in a Vancouver type B1 PFF (Avval et al., 2016; Chen et al., 2021; Ebrahimi et al., 2012). In addition, the same THA and plate implanted cadaveric femurs were physically loaded with a compressive force of 1200 N in a previous testing study, while no relative motion was observed between the femur and the stem. This axial compression testing setup was developed and described in detail in Chapter Two. The fully bonded configuration appropriately represented the lack of displacement at the bone-stem interface. Since locking screws were used in the physical specimens, interfaces between the plate and screws and the bone and screws were modeled as fully bonded (Avval et al., 2016; Ebrahimi et al., 2012; Moazen et al., 2014, 2013).

$$\text{Bone Mineral Density } (\text{g/cm}^3) = -0.02184 + 0.8242 * \text{Hounsfield Unit} \quad \text{Eq.1}$$

$$\text{Ash Density } (\text{g/cm}^3) = 0.8772 * \text{Bone Mineral Density} + 0.07895 \quad \text{Eq.2}$$

$$\text{Apparent Density } (\text{g/cm}^3) = \text{Ash Density} / 0.6 \quad \text{Eq.3}$$

$$\text{Young's modulus (MPa)} = 6850 * \text{Apparent Density}^{1.49} \quad \text{Eq.4}$$

To assess plate stresses under ADL-loading after the healing of a primary Vancouver type B1 PFF, peak hip contact force and femoral muscle forces during gait (taken at the point of contralateral toe-off, approximately 25% of the stance phase), stair descent and sit-to-stand were calculated using a coupled musculoskeletal and FE model and applied to the THA and plate implanted femur FE models (Fig. 3.1A) (Chen et al., 2021; Myers et al., 2018). As described in detail in Chapter Two, muscle forces were modeled as distributed

loads and applied over designated elliptical insertion areas that were defined for each muscle centered at its insertion point in the initial musculoskeletal model (Fig. 3.1A) (Chen et al., 2021).

In addition to simulating ADL loads in healed PFF models, ADL loads were applied to femur models with a simulated Vancouver type B1 PFF. In each femur model, a transverse fracture was created 15 mm below the tip of the implanted femoral stem with a 10 mm gap (Fig. 3.1C). The fracture gap simulated a clinically unstable and/or non-union Vancouver type B1 PFF, which has shown higher rates of refracture and/or hardware failure after the initial fixation (Choi et al., 2010; Leonidou et al., 2015; Moazen et al., 2014, 2013). The simulated fracture was located between two implanted 5.0 mm bicortical screws in each physical specimen so that the fixation plate was able to bridge the simulated fracture (Fig. 3.1C). Contact between the plate and the bone, and between bone segments were modeled as frictional with a friction coefficient of 0.3 (Moazen et al., 2013). Peak hip contact force and corresponding muscle forces in three ADLs were applied to the fractured femur models using the same method as in the healed models.

3.2.2 EVALUATION OF PLATE MECHANICS IN PFF AND HEALED FEMUR FE MODELS UNDER PEAK ADL LOADS

In reference to the clinically-observed fracture failure of the plate, maximum principal stress in the plate was chosen as the primary stress variable to be evaluated (Fig. 3.2) (Moazen et al., 2016; Takahashi et al., 2021). The plate was divided into 16 segments using evenly spaced 15 cross-sections (perpendicular to the Y-axis of the plate coordinate system)

based on the locations of screw holes (Fig. 3.2). Segments showing high stress concentration were identified as critical segments which may be at higher risk of plate fracture (Fig. 3.2).

In healed models, critical elements in the plate were identified as those showing maximum principal stress above the 95-percentile stress level across all plate elements under each ADL-loading (only 5% plate elements showed higher stress than the threshold; the 95-percentile stress level was calculated using elemental volume weighted values of maximum principal stress). Critical segments in the plate were identified as those that had more than 10% of volume of critical elements in the segment (Fig. 3.2). Our preliminary analysis showed that using the 95-percentile stress and the 10% volume as thresholds not only provided appropriate quantitative basis for the characterization of critical segments, but also better facilitated the further development of simplified mechanical tests aimed at best matching the stress state in the plate under ADL-loading (described in detail in section 3.2.4). Elemental volume weighted mean maximum principal stress and mean von Mises stress in critical elements were then calculated for the critical segments identified.

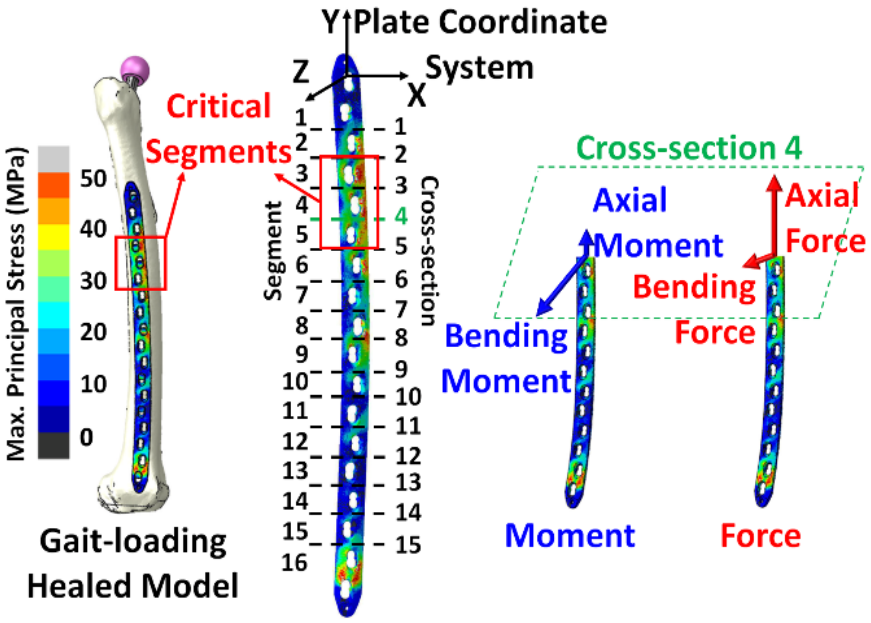

Fig. 3.2. An example of simulated plate stress and the load transfer in the plate in a gait-loading healed model. The plate was divided into 16 segments using 15 cross-sections. Plate segments with concentrated high maximum principal stress were identified as critical segments (segments 3 through 5 in the gait-loading healed model). Resultant moment and force in cross-sections (e.g. cross-section 4) were evaluated with focuses on those inside critical segments.

In addition to analyzing the stress state in the plate, load transfer through the plate was evaluated by calculating resultant force and moment that were transferred through each cross-section of the plate (Fig. 3.2). The resultant force and moment through each cross-section were transformed into the plate coordinate system and were analyzed in bending and axial directions (Fig. 3.2). Bending moment and force were the summation of the X and Z components of moment and force, respectively (parallel to the cross-section plane, Fig. 3.2). The axial moment and force were the moment and force in the Y direction.

In PFF models, due to the considerably higher magnitude of maximum principal stress as compared with the healed models, critical elements in the plate were identified using the yield stress (869 MPa) of stainless steel as the threshold. The percentage volume of critical elements was calculated in each plate segment. The plate segments that showed concentrated critical elements were identified as critical segments. Elemental volume weighted mean maximum principal stress and mean von Mises stress in critical elements were calculated in critical segments. Resultant force and moment in bending and axial directions were evaluated through plate cross-sections.

3.2.3 EVALUATION OF THE STANDARD 4-POINT-BEND TEST IN MATCHING PLATE MECHANICS IN ADL-LOADING PFF MODELS

To match the stress state in the plate in PFF models under ADL loads, a standard plate-only 4-point-bend test was modeled (Fig. 3.3A) (ASTM International, 2008). Through evaluating plate stresses in the ADL-loading PFF models, locations of loading and support pins were chosen to best represent the stress state in the plate (Fig. 3.3A). The loading and support pins were modeled as rigid bodies, while the plate was modeled as elastic-plastic as described previously. Two vertical bending forces (the same magnitude, in the Z direction of plate coordinate system) were applied through the center of loading pins as body forces (Fig. 3.3A). The support pins were fixed in all degrees of freedom, while the loading pins could translate only in the Z direction (Fig. 3.3A). To simulate an idealized 4-point-bend test, frictionless contact was modeled between the surfaces of pins and the plate.

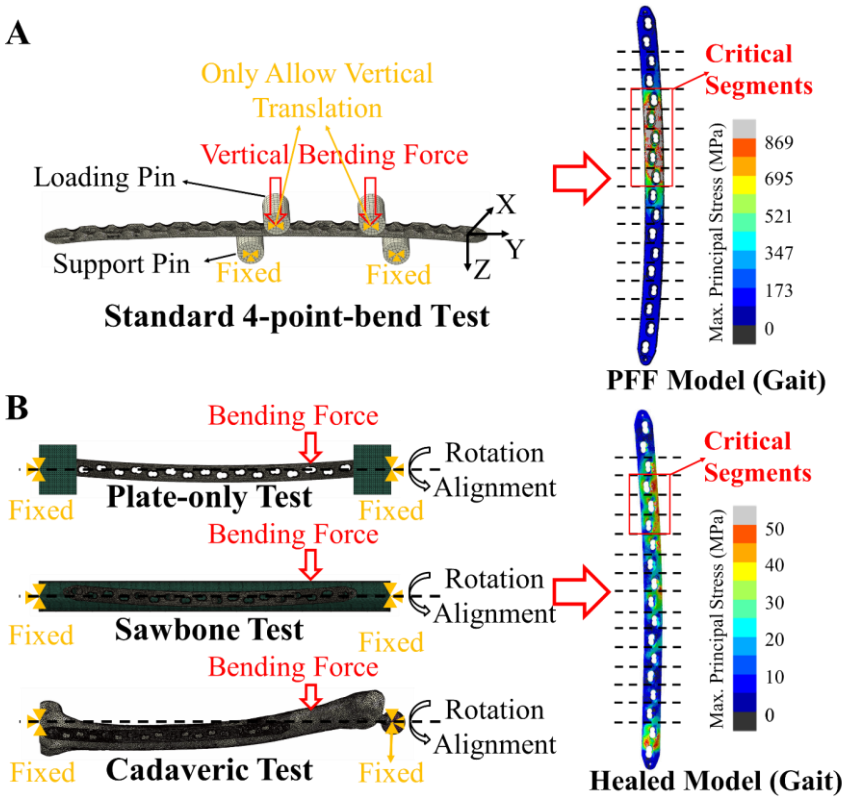

Fig. 3.3. The development of simplified mechanical tests based on healed and PFF models. **(A)** The standard 4-point-bend test was modeled to reproduce the stress state in the plate as in ADL-loading PFF models. **(B)** Three types of constrained 3-point-bend tests were developed to reproduce the stress state in the plate in healed models under ADL loads.

Using the yield stress of stainless steel (869 MPa) as the threshold, critical elements in the plate were identified (Fig. 3.3A). Percentage volume of critical elements in each plate segment, as well as elemental volume weighted mean maximum principal stress and mean von Mises stress in critical elements were calculated and compared with corresponding ADL-loading PFF models. Resultant moment and force in plate cross-sections were compared with ADL-loading PFF models.

3.2.4 DEVELOPING FE MODELS OF SIMPLIFIED MECHANICAL TESTS TO MATCH PLATE MECHANICS IN ADL-LOADING MODELS WITH A HEALED PFF

Based on our preliminary analyses, a constrained 3-point-bend test was found to match the healed model-predicted stress state in critical segments of the plate under ADL loads. For different testing purposes, three types of constrained 3-point-bend test were developed: 1) a plate-only test, 2) a sawbone test using a cylindrical sawbone, and 3) a cadaveric test that used the same femur model as each ADL-loading model (Fig. 3.3B). In the plate-only test, the plate was modeled to be potted at both ends in two cement blocks, while interfaces between the plate and the cement were modeled as fully bonded (Fig. 3.3B). The cement blocks were fixed in all degrees of freedom (Fig. 3.3B). In the sawbone and cadaveric tests, the plate was fixed to the cylindrical sawbone and the femur using the same configuration of 5.0 mm locking screws as those used in each ADL-loading model (Fig. 3.3B). Interfaces between the bone/sawbone and screws, and between the plate and screws were modeled as fully bonded. Surfaces of the proximal and distal aspects of the cylindrical sawbone were fixed in all degrees of freedom (Fig. 3.3B). In the cadaveric test, a flat cut was made just above the femoral condyles to simulate a surface for potting (Fig. 3.3B). Nodes on the potting surface, as well as the center of the femoral head were fixed in all degrees of freedom (Fig. 3.3B).

To best match the stress state in critical segments in the plate, a FE-integrated iterative optimization approach was developed to adjust the location and the magnitude of the bending force and the rotation of the specimen in constrained 3-point-bend tests (Fig. 3.3B). The optimization approach applied similar algorithm as the method used in Chapter Two.

The bending force was applied on the surface of either the plate or the specimen (the sawbone or the cadaveric bone) over a few nodes to avoid stress concentration (at the location of the arrows in Fig. 3.3B). After trials of different optimization objectives (including the mean maximum principal stress, mean von Mises stress and the percentage volume of critical elements), the percentage volume of critical elements in critical segments was chosen as the primary optimization objective, which was shown to best match the distribution of critical elements and magnitudes of mean maximum principal stress and mean von Mises stress in critical elements. The optimization was considered converged once the mean percentage error in the optimization objective reached less than ± 5% as compared with the corresponding healed ADL-loading model. In addition to the stress state, load transfer through cross-sections were calculated in the optimized models of three constrained 3-point-bend tests and compared with ADL-loading healed models.

3.2.5 DEVELOPMENT OF A BIAXIAL CADAVERIC TEST TO MATCH BOTH PLATE MECHANICS AND BONE STRAINS IN ADL-LOADING MODELS WITH A HEALED PFF

The optimized cadaveric 3-point-bend test could not match the complex pattern of axial force transfer as compared with ADL-loading healed models (described in detail in the result section), and hence an axial compressive force was added to the cadaveric test. Together with the bending force, applied forces in this biaxial loading configuration were optimized again with the same objective of matching the percentage volume of critical elements in critical segments as described previously. Similarly, the optimization was

considered converged once the percentage difference in the objective reached less than ±5%. In addition to analyzing the stress state and load transfer in the plate, bone strains around fixation screws were calculated in the newly optimized biaxial-loading cadaveric test and compared with the corresponding ADL-loading models. Mean absolute maximum principal strain was calculated in bone elements that were within a 10-mm-diameter cylindrical region of interest (ROI) that was center at the axis of each fixation screw.

3.3 RESULTS

3.3.1 PLATE MECHANICS UNDER ADL LOADS

In ADL-loading models with a simulated PFF, almost all critical elements (plate elements that experienced maximum principal stress higher than the yield stress of 869 MPa) were found in segments four through eight across three ADLs (Fig. 3.4A and B). Those were the segments between the two bicortical screws that bridged the simulated transverse fracture. The stair-descent load resulted in the highest percentage volume of critical elements (Fig. 3.4B), as well as the highest mean maximum principal stress and mean von Mises stress in critical elements (Fig. 3.4C).

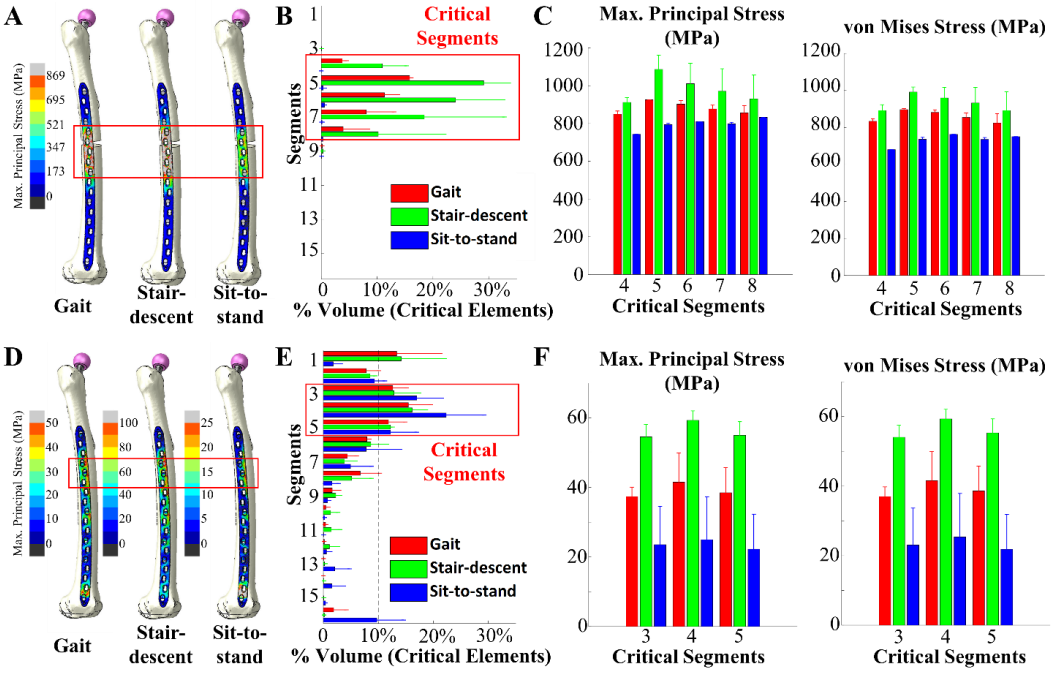

Fig. 3.4. Simulated stress state of plate in ADL-loading healed and PFF models. **(A)** Maximum principal stress in the plate (specimen 1) in ADL-loading PFF models. **(B)** Critical segments (segments 4 through 8) in ADL-loading PFF models. **(C)** Mean maximum principal stress and mean von Mises stress in critical elements were calculated in critical segments of PFF models. **(D)** Maximum principal stress in the plate in ADL-loading healed models. **(E)** Critical segments (segments 3 through 5) in ADL-loading healed models. **(F)** Mean maximum principal stress and mean von Mises stress in critical elements were calculated in critical segments of healed models.

Compared with PFF models, healed models showed significantly lower magnitude of maximum principal stress under peak loads of three ADLs (Fig. 3.4D). Across three ADLs, segments 3, 4 and 5 consistently showed higher than 10% volume of critical elements, and

therefore were identified as critical segments (Fig. 3.4E). Similar to PFF models, the stair-descent load showed the highest percentage volume of critical elements (Fig. 3.4E), mean maximum principal stress and mean von Mises stress in critical segments (Fig. 3.4F).

In both PFF and healed models, the bending moment and axial force were found to be the dominant component of load transfer in moment and force, respectively (Fig. 3.5A and B). In PFF models across three ADLs, bending moment and compressive axial force both plateaued in cross-sections 4 through 7 (inside the critical segments that bridged the simulated Vancouver type B1 PFF), with the stair-descent loading showing the highest bending moment (Fig. 3.5A). As expected, the magnitude of moment and force were considerably lower in the healed models as compared with the PFF models (Fig. 3.5B). Nonetheless, peak bending moments in all three ADLs were found inside critical segments at cross-section 4 (Fig. 3.5B). In contrast to PFF models, the sit-to-stand load resulted in the highest peak bending moment in healed models (4.2 ± 0.7 Nm in sit-to-stand compared with 4.0 ± 0.8 Nm in stair-descent and 3.2 ± 0.5 Nm in gait, Fig. 3.5B).

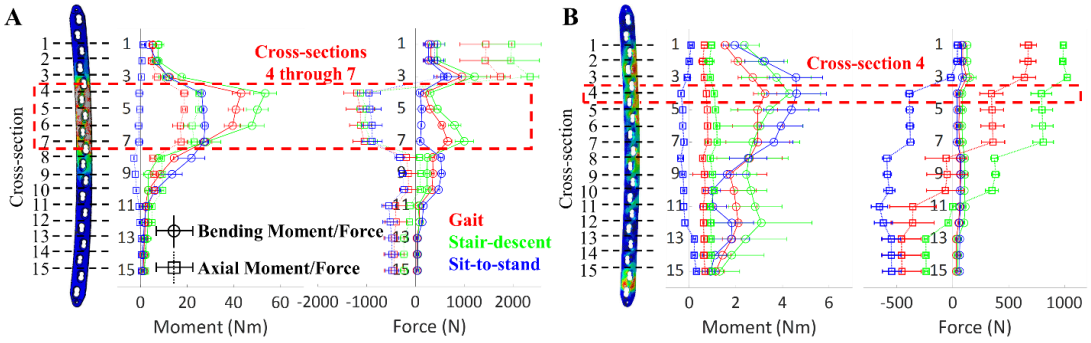

Fig. 3.5. Load transfer (mean ± standard deviation across three specimens) through all cross-sections in the plate was shown for ADL-loading PFF models **(A)** and ADL-loading healed models **(B)**.

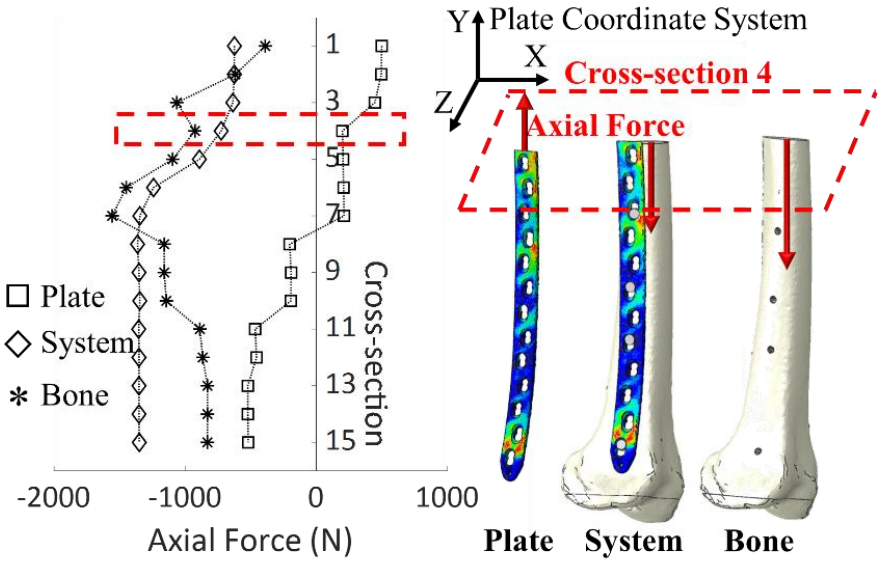

Fig. 3.6. Comparisons of load transfer in the bone, in the plate and in the bone-implant system. Using the gait-loading healed model of one specimen as an example, transfer of the axial force was shown separately for the plate, the entire system (including all implants and bone), and the bone. Resultant axial forces through cross-section 4 were shown in detail: the axial force in the plate was in the opposite direction as compared with the system and the bone.

Healed models showed a much more complex pattern of axial force transfer under ADL-loading (Fig. 3.5B). Tensile axial forces (in positive Y-direction of the plate coordinate system) were observed through the proximal cross-sections of the plate, whereas compressive axial forces (in negative Y-direction) were observed through distal cross-sections of the plate (Fig. 3.5B). When tensile axial force was observed at a plate cross-section (for example in cross-section 4 shown in Fig. 3.6), higher compressive axial forces were transferred through the bone as compared with the magnitude of compressive force

in the system at the same cross-section (Fig. 3.6). Under ADL loads, the proximal segments of the plate provided more compression to the bone through stiffening the entire system (more noticeable in gait and stair-descent), whereas the distal portion of the plate functioned to share the compressive force that was transferred through the system (Fig. 3.5B and Fig. 3.6).

3.3.2 SIMPLIFIED TESTS MATCHED PLATE STRESSES IN ADL-LOADING MODELS

Since the same critical segments were predicted in PFF models under loads of three different ADLs, positions of loading and support pins were the same (Fig. 3.7A), while the required vertical bending forces were determined to best match the plate mechanics for each ADL (Table 3.1). FE models of the standard 4-point-bend test estimated similar volumes of critical elements and similar magnitudes of stresses in the same critical segments as in ADL-loading PFF models (achieved less than ± 5% differences across three ADLs and three specimens, Table 3.2). The 4-point-bend tests were able to simulate the same plateaued pattern of resultant bending moment in cross-sections 4 through 7 (cross-sections within critical segments), however, the mean bending moment was slightly lower as compared with the ADL-loading PFF models (Fig. 3.7B and Table 3.2). In models of gait and stair-descent, high compressive axial forces were observed at cross-sections 3 and 8 located at the proximal and the distal ends of critical segments (Fig. 3.7B). However, 4-point-bend tests could not reproduce the plateaued axial compression through cross-sections 4 through 7 as observed under ADL loads (Fig. 3.7B).

	Magnitude of Bending Force (N)				Rotation Alignment (°)		
	Standard 4-point-bend Test (Vertical Bending Force)	Constrained 3-point-bend Test			Constrained 3-point-bend Test		
		Plate-only	Sawbone	Cadaveric	Plate-only	Sawbone	Cadaveric
Gait	3460 ± 860	605 ± 78	827 ± 106	1548 ± 199	30 ± 5	50 ± 5	50 ± 8
Stair-descent	5268 ± 957	756 ± 97	1395 ± 179	2288 ± 294	40 ± 8	50 ± 5	50 ± 5
Sit-to-stand	1873 ± 202	145 ± 19	387 ± 50	487 ± 62	10 ± 5	20 ± 5	10 ± 8

Table 3.1. Loading configurations (mean ± standard deviation across three specimens) of simplified mechanical tests. Magnitudes of vertical bending forces were shown for standard 4-point-bend tests. Optimized bending force and the rotation alignment of the specimen were shown for three types of constrained 3-point-bend tests.

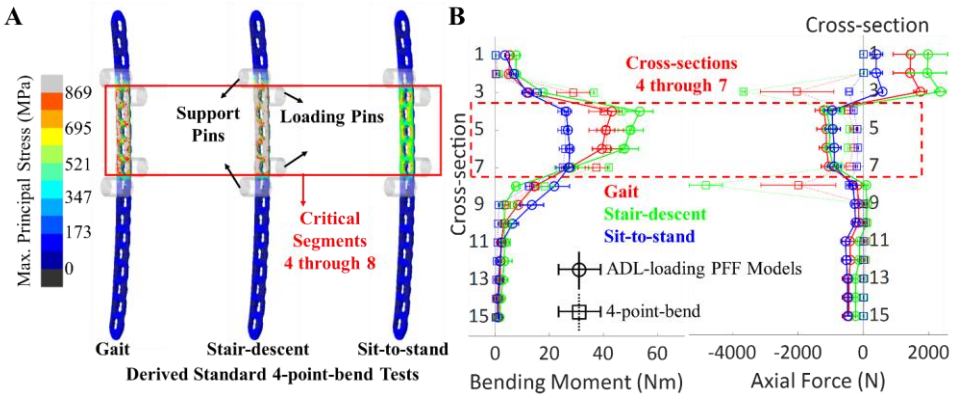

Fig. 3.7. Stress state of the plate and load transfer in optimized 4-point-bend tests. **(A)** Standard 4-point-bend tests estimated the same critical segments and the similar levels of maximum principal stress as compared with the ADL-loading PFF models. Support pins were positioned at segments 3 and 9, respectively. Loading pins were positioned at segments 4 and 8, respectively. **(B)** Comparisons of load transfer between ADL-loading PFF models and models of 4-point-bend test. Bending moment and axial force were shown, which were the dominant components in moment and force transfer in ADL-loading PFF models, respectively.

To match the stress state in the plate of ADL-loading models with a healed PFF, configurations of constrained 3-point-bend tests were optimized (Table 3.1). The optimized 3-point-bend tests were able to reproduce similar distributions of critical elements as compared with the healed models under ADL loads (Fig. 3.8A). All three tests reached less than ±1% mean differences in the percentage volume of critical elements in critical segments (the primary optimization objective, Table 3.2). The sawbone and cadaveric tests were able to achieve less than ±5% percentage differences in mean maximum principal stress and mean von Mises stress in critical elements (Table 3.2). The plate-only test did show higher percentage differences in mean stresses as compared with the sawbone and cadaveric tests (Table 3.2).

Mean % Difference (Across 3 ADLs)	Standard 4-point-bend Test	Constrained 3-point-bend Test			Biaxial Cadaveric Test
		Plate-only	Sawbone	Cadaveric	
% Volume (Critical Elements)*	-3.8 ± 0.3%	-0.1 ± 2.8%	0.6 ± 2.6%	-0.5 ± 3.4%	0.5 ± 2.6%
Max. Prin. Stress*	-3.4± 3.1%	12.4 ± 0.7%	1.1 ± 0.5%	0.8 ± 0.2%	0.7 ± 0.5%
von Mises Stress*	-1.8± 2.5%	11.5 ± 0.7%	0.2 ± 0.7%	-0.5 ± 0.7%	0.6 ± 0.7%
Bending Moment**	-10.0± 5.0%	20.5 ± 8.5%	-20.2 ± 0.5%	-8.3 ± 1.1%	9.4 ± 1.8%

Table 3.2. Percentage differences (mean ± standard deviation across three specimens and three ADL loads) in variables of plate mechanics between ADL-loading models and models of simplified mechanical tests. Results of standard 4-point-bend tests were compared with ADL-loading PFF models. Constrained 3-point-bend tests and the biaxial cadaveric test were compared with ADL-loading healed models. *, volume of critical elements and plate stresses were calculated from critical elements in critical segments. **, bending moment was calculated from cross-sections within critical segments; for constrained 3-point-bend tests and the biaxial cadaveric test, bending moment was calculated from segments 2 through 5 (Fig. 3.8B and 3.9B).

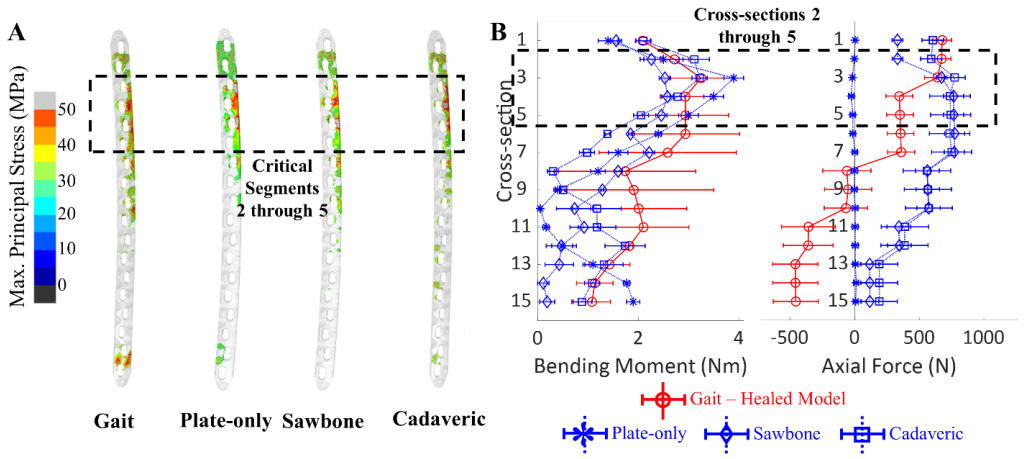

Fig. 3.8. Comparisons of plate stress determined critical segments and load transfer in simplified models derived from a gait-loading healed model. **(A)** Isolated critical elements in the plate were shown in a gait-loading healed model and the derived 3-point-bend tests. **(B)** Comparisons of load transfer between gait-loading healed models and the optimized models of 3-point-bend tests, with focuses on cross-sections 2 through 5. Comparisons were shown for bending moment and axial force.

Percentage differences in mean bending moments were found to be less than ±20% through cross-sections 2 to 5 (the cross-sections that expanded critical segments, Fig. 3.8B and Table 3.2), with the plate-only test showing a higher mean bending moment (20.5 ± 8.5%, Table 3.2), while the sawbone and the cadaveric tests showed lower mean bending moments as compared with the ADL-loading healed models (Table 3.2). None of the three 3-point-bend tests were able to simulate the complex pattern of load transfer in axial force as observed in healed models under ADL loads (Fig. 3.8B). For example under gait-loading, the plate experienced tensile axial force (positive) through proximal cross-sections (1 through 7, Fig. 3.8B), while the axial force converted to compressive (negative) through

distal cross-sections (8 through 15, Fig. 3.8B). In contrast, the sawbone test and the cadaveric test showed tensile axial force through all cross-sections of the plate, while the resultant axial forces in the plate-only test were very low in magnitude (Fig. 3.8B).

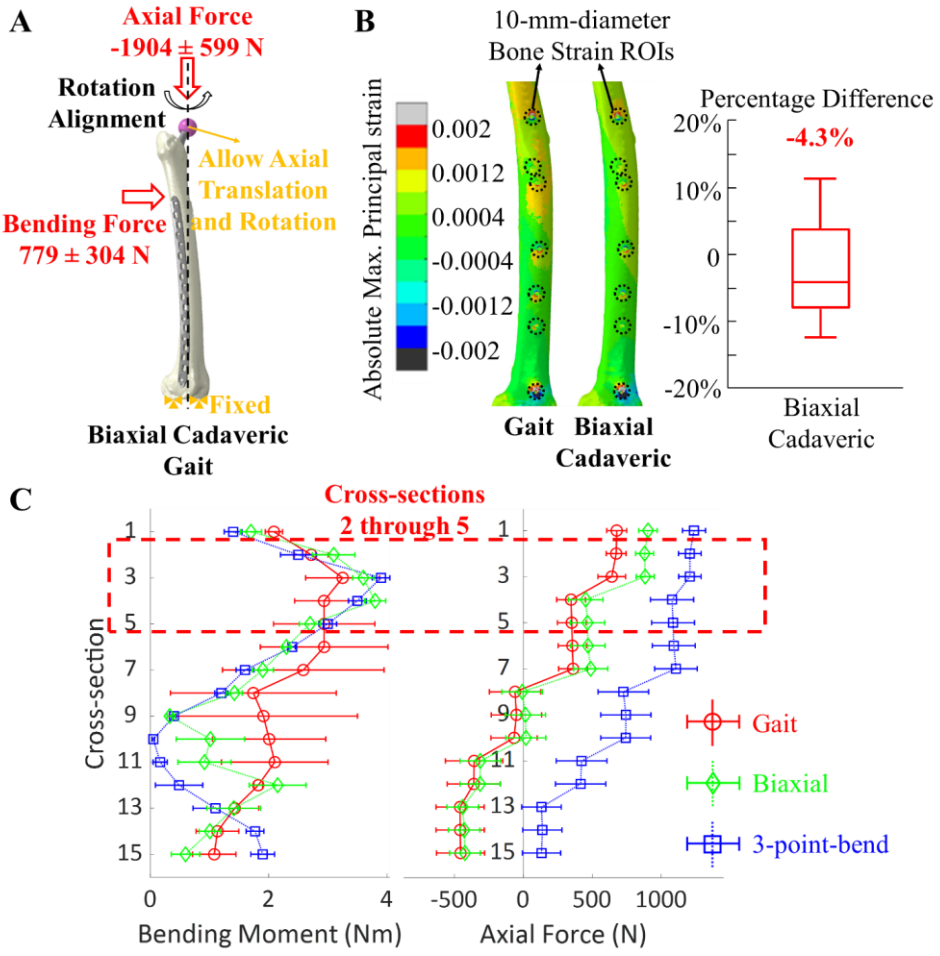

Fig. 3.9. The biaxial cadaveric test. **(A)** Optimized biaxial cadaveric test for gait-loading healed models. **(B)** Comparisons of absolute maximum principal strain in bone ROIs (bone elements within10-mm-diameter cylindrical regions centered at each screw hole). **(C)** Comparisons of load transfer (mean ± standard deviation across three specimens) across gait-loading healed models, biaxial cadaveric models, and 3-point-bend cadaveric models.

3.3.3 BIAXIAL CADAVERIC TEST MATCHED BOTH PLATE STRESSES AND BONE STRAINS AROUND FIXATION SCREWS AS IN ADL-LOADING MODELS

An axial force was added to the 3-point-bend cadaveric test, while the loading configurations of this biaxial cadaveric test was reoptimized (Fig. 3.9A). In addition to achieving good agreement with corresponding ADL-loading models in plate mechanics (including stresses and load transfer, especially improved agreement in axial force transfer, Fig. 3.9C and Table 3.2), the reoptimized biaxial cadaveric test also matched the principal strain distributions in bone elements around the screw holes (achieved a median percentage difference of -4.3% in absolute maximum principal strain as compared with the gait-loading model, Fig. 3.9B).

3.4 DISCUSSION

Through comprehensive analyses of plate mechanics in THA and plate-implanted femurs, this study developed appropriate simplified mechanical tests that showed fidelity in reproducing plate mechanics in ADL-loading models either with an existing or a healed Vancouver type B1 PFF. The standard 4-point-bend test showed fidelity in matching the stress state and the bending moment in ADL-loading models with a simulated PFF, however, the newly-developed constrained 3-point-bend tests were shown to best match the plate stress and bending moment as observed in ADL-loading models with a healed PFF. Furthermore, an optimized biaxial cadaveric test (constrained 3-point-bend test with an axial force) matched both the plate mechanics (including a good agreement with the axial force that the 3-point-bend test could not reproduce) and the bone strains around the

fixation screws. This study provided purpose-driven testing options that can be readily implemented in both experimental and computational forms.

Risks of plate fracture have been assessed using FE model-predicted plate stresses. Concentrated plate elements with higher than yield level maximum principal stress indicate the formation of cracks and microfractures, which may further progress to fracture of the plate (Moazen et al., 2014, 2013). With a simulated fracture gap (represented by a non-union or a delayed-union Vancouver type B1 PFF (Choi et al., 2010; Moazen et al., 2014, 2013; Takahashi et al., 2021), as well as the initial state of the plate fixation), up to 15% and 30% volume of plate elements in critical segments showed beyond yield level maximum principal stress under peak loads of gait and stair-descent, respectively. The indicated risk of plate fracture in critical segments was consistent with the clinically-reported complication rates in patients with non-union or delayed-union type B1 PFFs (Giovanni et al., 2020a; Randelli et al., 2018). On the other hand, early postoperative mobilization and weight bearing as tolerated have shown promise in reducing complications in patients after surgery for hip fractures (Ottesen et al., 2018; Warren et al., 2019). Though results were not shown, the ADL-loading PFF models showed that peak maximum principal stresses in the plate stayed below the yield threshold when partial forces were applied in three ADLs (up to 50% of hip contact force and muscle forces in gait, 30% forces in stair-descent and 90% forces in sit-to-stand, respectively). Though the *in vivo* muscle loading in PFF patients requires further investigation, the results of the current study suggested that the plate was able to withstand partial ADL-loading without plastic deformation. In contrast, plate stresses were drastically reduced after the complete

healing of a primary Vancouver type B1 PFF. However, peak loads of three different ADLs estimated the same critical segments in the plate that showed concentrated high maximum principal stress (above the 95-percentile stress level in each model) in healed models. The risks of acute plate fracture may be low, however, risks of plate fatigue under repetitive loading remain to be further investigated.

The standard 4-point-bend test was demonstrated to be an appropriate test for the evaluation of plate stresses before the healing of a PFF, especially for a non-union and/or unstable type B1 PFF. The standard 4-point-bend test reproduced both the concentrated stress and the plateaued bending moment in the same critical segments as observed in ADL-loading models. In contrast, the newly developed constrained 3-point-bend tests were shown to best match plate stresses and the resultant bending moment in the healed models. Considering realistic testing environment and purposes, the development of constrained 3-point-bend tests explored different testing setups including a plate-only test (as in the ASTM standard 4-point-bend test), a sawbone test, and a cadaveric test. Due to the simplicity of the test setup, the plate-only test and the sawbone test could be adopted in cyclic testing of the fatigue performance of the plate, which could provide critical information on the risks of plate failure once patients resume ADLs after the healing of PFF.

Simplified tests successfully reproduced the stress state in critical segments of the plate in ADL-loading models once the resultant bending moment in critical segments was matched. Though lack of agreement in resultant axial force did not affect the good agreement in the stress state in critical segments, the 3-point-bend cadaveric test could not

match the bone strains around the screws as compared with the ADL-loading healed models. However, with an additional axial force, the reoptimized biaxial cadaveric test successfully improved the agreement in axial force transfer as compared with ADL-loading models, while also showing good agreement in bone strains around the screws. The biaxial cadaveric test could serve as a more appropriate option for the evaluation of screw loosening upon loading.

A variety of experimental and computational studies have applied different simplified loading conditions to evaluate the mechanics and the performance of PFF fixation plates (Choi et al., 2010; Lenz et al., 2016b, 2016a; Lever et al., 2010; Moazen et al., 2014, 2013, 2011; Pletka et al., 2011; Wang et al., 2019). Besides the standard 4-point-bend test (ASTM International, 2008; Lenz et al., 2016a; Lever et al., 2010), previous studies have evaluated plate stiffness and fixation under simple compression (Lenz et al., 2016b, 2016a; Lever et al., 2010; Moazen et al., 2014, 2013; Pletka et al., 2011), torsion (Choi et al., 2010; Lenz et al., 2016a; Lever et al., 2010; Pletka et al., 2011), and 3-point-bend tests (Choi et al., 2010). However, the lack of standard testing methodology and outcome measures has made it difficult to directly compare results from different studies. The lack of standard testing methodology is partially the result of limited knowledge of the *in vivo* plate mechanics and performance. In previous studies, coupled musculoskeletal and FE models have shown promise in simulating biomechanics of bone and bone-implant systems under physiological loads (Chantarapanich et al., 2016; Chen et al., 2021; Duda et al., 1998; Jitprapaikulsarn et al., 2021; Speirs et al., 2007a; Taylor et al., 1996). Coupled musculoskeletal and FE models were shown to accurately estimate the bone remodeling stimuli in THA-implanted femur

(Chen et al., 2021; Duda et al., 1998; Speirs et al., 2007a; Taylor et al., 1996). Additionally, muscle-loading FE models have been used to evaluate the initial stability of fracture fixation in the native femur (without THA or other implants) (Chantarapanich et al., 2016; Jitprapaikulsarn et al., 2021). Utilizing ADL-loaded cadaveric femur models, this study simulated the *in vivo* state of plate mechanics, which provided a basis for the subsequent evaluation and development of simplified mechanical tests to assess risks of plate fatigue and fracture.

Limitations regarding the scope of this study should be considered. Aimed at evaluating and developing simplified mechanical tests to evaluate the risks of plate fracture, this study focused on the analyses of plate mechanics, including plate stresses and load transfer. However, the successful development of combined compression and bending cadaveric test showed that simplified tests may concurrently match plate mechanics and bone strains around the fixation screws as in ADL-loading models. Future studies may apply a similar FE-integrated optimization approach to evaluate in detail how simplified loading configurations may affect bone strains, and therefore provide more information on the risks of screw loosening. Through developing specimen-specific coupled musculoskeletal and FE models for three cadaveric femurs, the current study successfully simulated the *in vivo* state of stresses and load transfer in the plate after PFF fixation. Future studies may apply a similar methodology to develop models for femurs from a larger population, thereby enabling the simulation of the biomechanics of the bone-implant system for specimens with different demographic characteristics.

Several other limitations regarding the method used in this study should be considered. The bone-stem interface and the bone-screw interface were both modeled as fully bonded. The bonded bone-stem interface simulated a well-fixed cementless THA stem, therefore this study only simulated a Vancouver type B1 PFF. Future studies will model a sliding interface between the femur and the stem to simulate a Vancouver B2 or B3 PFF, which can provide additional information on the plate mechanics with a loosened stem. Similarly, future studies will investigate the impact of the bone-screw interface contact definition on bone strains around fixation screws.

3.5 CONCLUSION

Appropriate simplified mechanics tests were successfully identified for the assessment of the risk of plate fracture both before and after the healing of a Vancouver type B1 PFF. Compared with the complex loading configuration in the ADL-loading femur model, the optimized simplified tests can be readily implemented in both experimental and computational forms. This study provides a basis for the development of a complementary experimental/computational framework that can serve as an advanced pre-clinical platform for minimizing the risk of construct failure for the fixation of PFF.

CHAPTER FOUR. IMPACT OF PERIPROSTHETIC FEMORAL FRACTURE FIXATION PLATING CONTRUTS ON LOCAL STIFFNESS, LOAD TRANSFER AND BONE STRAINS

4.1 INTRODUCTION

Secondary failures after successful plate-screw fixation and healing of a primary Vancouver type B1 periprosthetic femoral fracture (PFF) have remained a clinical concern (Abdel et al., 2016; Giovanni et al., 2020a; Lindahl et al., 2006; Moloney et al., 2014; Randelli et al., 2018; Raschke and Schliemann, 2020). With the complete healing of a primary B1 PFF, the most prevalent failures of fixation include the secondary femoral fracture at a new location, and the loosening and/or the breakage of the plate-screw construct (Giovanni et al., 2020a; Lindahl et al., 2006; Randelli et al., 2018; Raschke and Schliemann, 2020). Those complications require a complex reoperation to fix, which is not only difficult but have also been reported to significantly worsen the prognosis (Giovanni et al., 2020a; Randelli et al., 2018).

In addition to patient demographics, the biomechanics of plate-screw fixation for the primary Vancouver type B1 PFF have been hypothesized to play a key role in the pathogenesis of failures of fixation (Bryant et al., 2009; Giovanni et al., 2020a; Moloney et al., 2014; Randelli et al., 2018). Secondary femoral fractures have been reported to occur

often at a location more distal to the healed primary PFF, which has been associated with elevated local strains/stresses in bone caused by the implantation of the plate-screw construct (Giovanni et al., 2020a; Moloney et al., 2014; Randelli et al., 2018). Elevated bone strains/stresses may also cause localized bone damage, which has been associated with the loosening of screws (Feng et al., 2019; Panagiotopoulos et al., 1994; Sugiura et al., 2000).

Extending the length of the plate to the lateral condyle of the femur has been proposed clinically to reduce the risks of secondary failures of fixation by distributing the physiological femoral load along the entire length of the femur (Bryant et al., 2009; Moloney et al., 2014). However, supporting evidence is lacking due to the difficulties in direct measurement of *in vivo* state of strains/stresses in bone. FE models of the bone-plate system have been utilized to assess the stability and strength of PFF fixation by evaluating the stiffness of the system (Choi et al., 2010; Lever et al., 2010). Meanwhile, FE models have been used to evaluate the stress state in different plate-screw constructs to ensure the plate may not fail upon loading (Moazen et al., 2016, 2014). However, these previous studies of PFF fixation either lacked corroboration with experimental data or did not simulate the physiological loads in the femur. Nonetheless, no study has evaluated mechanisms underlying the secondary failures of fixation after the healing of a primary Vancouver type B1 PFF.

Hence, the objective of this study was to compare PFF fixation mechanics, including resulting bone strain, local load transfer, and stiffness for different construct lengths in different plating systems during simulated gait-loading.

4.2 MATERIALS AND METHODS

Briefly, CT-reconstructed geometries of three cadaveric femurs (different specimens from the specimens used in Chapters Two and Three) were used to develop THA and plating system implanted FE models for two different plating systems (each had a diaphyseal and a condyle-spanning configuration, five implanted models for each femur). The modeled THA femoral component and the diaphyseal and condyle-spanning constructs of one of the two modeled plating systems (described in detail in later sections) were physically implanted to each cadaveric femur, which were experimentally tested to validate the corresponding FE models. Through simulating the load in mechanical testing and the physiological gait-loading, the validated femur FE models were used to evaluate and compare the mechanics of PFF fixation for two different plating systems with two construct lengths (the diaphyseal and the condyle-spanning construct).

4.2.1 CADAVERIC SPECIMEN PREPARATION

Three fresh frozen cadaveric femurs (all left femurs; two males, one female; age, 78.5±7.8; height, 168.9±7.1 centimeters; weight, 66.7±13.9 kilograms) were CT scanned with a density phantom (QCT Pro, Mindways Software, Inc., Austin TX, USA) prior to dissection of all soft tissues. The distal femur was potted into a custom fixture using bone cement. The lateral condyle of each femur remained exposed after potting to allow implantation of the fracture fixation plate (Fig. 4.1A). Markers for a digital image correlation (DIC) system (GOM, Braunschweig, Germany) were glued on the anterolateral surface of each femur to allow tracking of bone displacement upon loading (Fig. 4.1A).

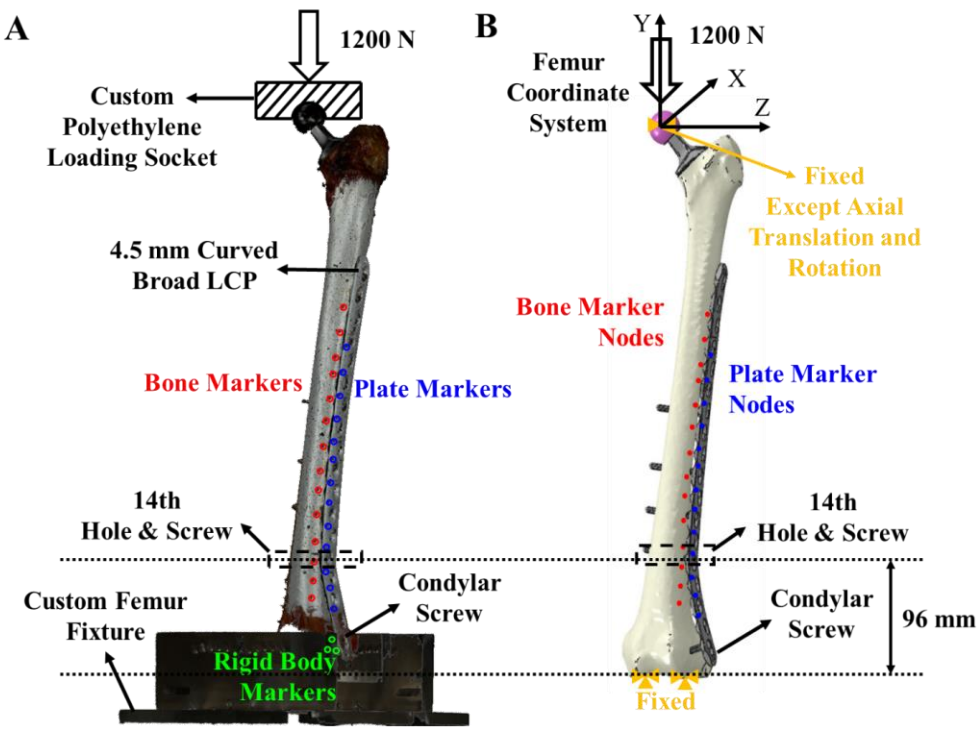

Fig. 4.1. Experimental setup and the FE modeling of THA and plate implanted cadaveric femur model. **(A)** The 3D-scanned geometry of a cadaveric femur (specimen 2) implanted with the THA femoral component and the LCP18 construct. **(B)** The THA and LCP18 implanted FE model of the scanned cadaveric femur.

4.2.2 MECHANICAL TESTING OF THA AND PLATE IMPLANTED FEMURS

For each cadaveric femur, three implanted conditions were mechanically tested: 1) femur implanted with a THA stem and femoral head (the THA condition); 2) THA femur implanted with a diaphyseal plate-screw construct, the Synthes 4.5 mm Curved Broad Locking Compression Plate (LCP, DePuy Synthes, West Chester, PA) without the condylar screw (denoted as the LCP14 condition); 3) THA femur with a condyle-spanning plate-screw construct that reached the lateral condyle of the femur (an additional condylar screw

was implanted to the femur in the LCP14 implanted femur to add fixation through the lateral condyle, denoted as the LCP18 condition).

Initially, each cadaveric femur was implanted with a commercially-available cementless femoral stem and a 28-mm-diameter cobalt-chrome femoral head (different from the component modeled in Chapters Two and Three; Corail®, DePuy Synthes, Warsaw, IN) by a fellowship trained orthopedic surgeon. A best-fitting stem size was chosen by the surgeon. Among the three specimens, two were implanted with a collared stems, and one was implanted with a collarless stem. The THA-implanted femur was rigidly fixed in the custom fixture in 3° valgus and 3° flexion (Chen et al., 2021). The geometries of the specimen were scanned within the fixture using a Artec Spider 3D scanner (Artec 3D, Luxembourg) so that the *in situ* position of the stem was quantified.

With the fixture, the THA-implanted specimen was placed in a uniaxial Instron test frame (Instron, Norwood, MA). A custom polyethylene loading socket was rigidly connected to the load cell of the test frame and was used to load the THA implanted femurs through the femoral head (Fig. 4.1A). Since the loading socket is fully conforming with the 28-mm-femoral head, the femoral head could only translate axially relative to the loading frame. The axial rotation of the femoral head was not constrained due to the low friction between the Cobalt-Chrome femoral head and the polyethylene socket (friction coefficient less than 0.1 (Chan et al., 2011)).

To eliminate any settling effect between the stem and the bone before testing, each specimen was conditioned using a compressive load of 600 N for three cycles using a constant loading and unloading rate of 40 N/s. In each cycle, the peak load of 600 N was

held for five seconds, then the load was decreased to 10 N and held for another five seconds before initiating another loading cycle. Marker displacement of all three specimens stabilized during the conditioning. Three cycles of testing load of 1200 N were then applied using the same loading and unloading rate of 40 N/s while maintaining the five-second holding at the peak load and the unloaded stages (Fig. 4.2). The chosen magnitude of testing load was shown in a previous study to be able to reproduce the strain state of the THA implanted femur during peak gait-loading (Chen et al., 2021). The displacement of bone markers was recorded at a data collection rate of two Hz through the duration of three testing cycles (Fig. 4.2).

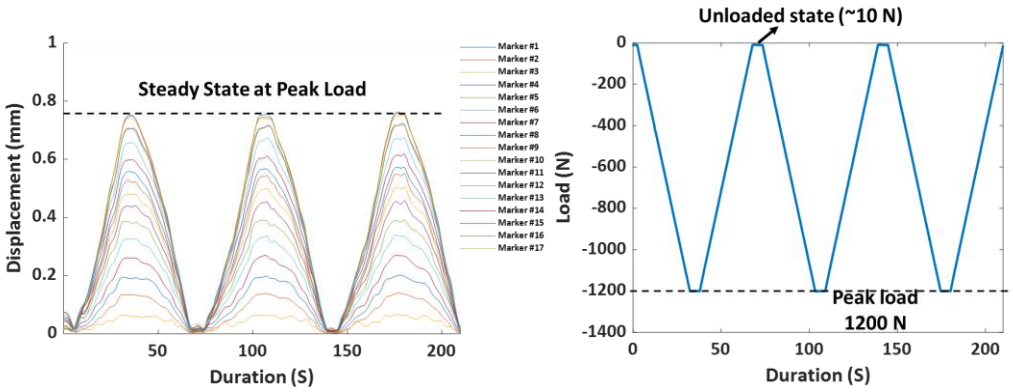

Fig. 4.2. The displacement profile and the loading profile of the mechanical testing. Left, DIC recorded displacement of 17 bone markers during a test using the 1200 N loading profile. Note that marker displacement was stable during three loading cycles. Right, loading profile using a peak load of 1200 N (-1200 ± 0.3 N across three loading cycles in the graph).

Following the THA testing, each specimen was implanted with a diaphyseal plate-screw construct. A 4.5 mm Curved Broad LCP was implanted and fixed to each femur using six

5.0-mm locking screws, with the most distal diaphyseal screw implanted through the 14th hole on the plate (the LCP14 construct, Fig. 4.1A). Depending on the position of the implanted THA stem in each specimen, two or three unicortical screws were implanted into the proximal femoral diaphysis, while bicortical screws were implanted below the THA stem. To keep plate positions consistent among specimens, the most distal screw of the LCP14 construct was implanted approximately 96 mm (± 10 mm) above the distal fixation surface of each femur (Fig. 4.1A). The plate was contoured to the shape of each femur so that the distal portion of the plate (the portion below the 14th hole and screw) was not in contact with the femur. This was to ensure the LCP14 condition simulated a short diaphyseal plate (Fig. 4.1A). DIC markers were placed onto the surface of each plate to record the displacement of plate during loading. The LCP14 implanted femur was tested using the same loading protocol of 1200 N, while displacement was recorded using the DIC system at a rate of two Hz.

Lastly, one additional 5.0-mm locking screw was implanted into the lateral condyle of each femur through the most distal screw hole (the 18th hole) on the LCP to complete the condyle-spanning construct (the LCP18 condition). The LCP18 construct was tested using the same 1200 N loading profile, while the displacement of bone and plate markers was recorded (Fig. 4.2). Specimens were 3D scanned again with the fixture to determine the positions of the plate and screws in each femur after testing.

DIC recorded displacement was transformed into the International Society of Biomechanics recommended femoral coordinate system and compared across different implanted conditions (Wu et al., 2002). Peak displacement was calculated as the

differences between the displacement at the peak load (1200 N) and the displacement at the corresponding unloaded stage (approximately 10 N). The mean and standard deviations of peak displacement were calculated using data from three cycles of loading during each test. Using the displacement of the fixture markers, a rigid body compensation was applied to both the bone and plate markers to reduce the effect of rigid motions of the fixture.

4.2.3 DEVELOPMENT AND VALIDATION OF FINITE ELEMENT MODELS OF IMPLANTED FEMURS

Using CT scans of the mechanically tested three cadaveric femurs, FE models of THA and plate implanted femurs were developed for two different plating systems that each had a diaphyseal configuration and a condyle-spanning configuration (one of the plating system was the physically implanted LCP system).

Initially, each cadaveric femur was virtually implanted with models of the THA femoral component and the LCP construct (LCP14 and LCP18) in Abaqus 2018 (Dassault Systèmes, Vélizy-Villacoublay, France), and accurately replicated the *in situ* implant positions in each femur using 3D scans of each specimen as the reference (Fig. 4.1). The screws were modeled as cylinders with the same diameter (the major pitch diameter) as the physical screws implanted in the specimens.

The femur, the THA component, the plate and the screw were meshed using 10-noded tetrahedral elements in Abaqus using mean edge lengths of 2 mm, 2 mm, 1 mm, and 0.5 mm, respectively. The local bony interfaces with screws were also meshed using a 0.5-mm edge length. The mesh sizes were determined through a preliminary mesh convergence

study that showed further decreases in edge length did not result in a greater than 5% changes in displacement and principal strains.

The cobalt-chrome THA stem and head were modeled as linear elastic with a Young's modulus of 210 GPa and a Poisson's ratio of 0.29. The stainless-steel fracture fixation plate was also modeled as linear elastic with a Young's modulus of 149 GPa and a Poisson's ratio of 0.3 (ASTM F138-13a, 2013). Apparent densities of bony materials were interpolated from CT Hounsfield units (HUs) using the density phantom (Eq. 1 to 3) (Schileo et al., 2008). In Bonemat software (Taddei et al., 2007), Young's moduli of bony materials were calculated using literature reported density-modulus relationships and assigned to the FE models in 50 MPa intervals (Eq. 4) (Morgan et al., 2003). The Poisson's ratio for all bony materials was set to be 0.3. Since negligible relative displacement was observed between the THA stem and the femur during the experiment, the interface between the THA stem and the femur was modeled as fully-bonded. The screws were modeled as fully bonded to the bone at the interface. As all locking screws were utilized, interfaces between screws and plate were also modeled as fully bonded.

$$\text{Bone Mineral Density } (\text{g/cm}^3) = -0.02184 + 0.8242 * \text{HU} \quad \text{Eq. 1}$$

$$\text{Ash Density } (\text{g/cm}^3) = 0.8772 * \text{Bone Mineral Density} + 0.07895 \quad \text{Eq. 2}$$

$$\text{Apparent Density } (\text{g/cm}^3) = \text{Ash Density} / 0.6 \quad \text{Eq. 3}$$

$$\text{Young's Modulus (MPa)} = 6850 * \text{Apparent Density}^{1.49} \quad \text{Eq. 4}$$

To validate the FE models against experimentally measured displacement, the FE models simulated the same loading condition as in the mechanical testing. For each DIC marker (bone or plate markers) in the physical experiment, a closest node was identified in

each FE model as the marker node (Fig. 4.1B). FE model calculated nodal displacement of each marker node was compared to the corresponding experimental marker displacement.

Given the reported variances in the density-modulus relationship for the bone, Young's moduli of bone were calculated using three different first coefficients in Eq. 4 to analyze the influence of property variances on FE predictions (Morgan et al., 2003). The reported mean coefficient was shown in Eq. 4. Additionally, the reported bounds of the 95% confidence interval of the first coefficient were used in FE simulations (5440 and 8630, respectively) (Morgan et al., 2003).

4.2.4 COMPARISONS OF THE BIOMECHANICS BETWEEN TWO PLATING SYSTEMS

Using the validated femur models, FE models of a new plating system, the VA-LCP Periprosthetic Proximal Femur System* (DePuy Synthes, West Chester, PA, USA; PFP+DSAP) were developed to compare with the LCP14 and LCP18 models. Firstly, the VA-LCP Proximal Femur Plate (PFP) of the new system was implanted to each THA model and fixed to the femur using six 3.5-mm bicortical locking screws in the proximal portion of the femur and three 5.0-mm bicortical locking screws (Fig. 4.2A) in the distal portion. To better compare with the LCP14 models, the PFP models maintained the same location of the most distal diaphyseal screw as in the LCP14 models (96 ± 10 mm above the bottom fixation surface of each femur, Fig. 4.3A). After the virtual implantation of the PFP, a modular component of the VA-LCP Periprosthetic Proximal Femur System, the Distal Femur Spanning Attachment Plate (DSAP), was added to each PFP implanted model

(herein referred to as the DSAP model). The DSAP plate was attached to the underlying PFP plate using two connecting screws and was fixed to the lateral condyle of each femur using four 3.5-mm locking screws (Fig. 4.3A). According to the recommendation in the surgical technique guide for the novel system, the connecting screws had a minimum of one-hole spacing between the screws. The screws of PFP and DSAP constructs were also modeled as cylinders. Interfaces between screws and the bone, and between screws and the plate were modeled as fully bonded. The implanted plate and screws were modeled with a Young's modulus of 149 GPa and a Poisson's ratio of 0.3 (ASTM F138-13a, 2013).

In LCP14 and LCP18 implanted models, bone elements around the three distal diaphyseal screws and the condylar screw were isolated as regions of interest (ROIs of DSC1, DSC2, DSC3 and CSC, 10 mm diameter cylindrical volume centered at the axis of each screw, Fig. 4.3A). An additional ROI of the distal femoral metaphyseal shaft was identified between the most distal diaphyseal screw and the condylar screw (the DIST-FEMUR ROI, Fig. 4.3A). Elemental volume weighted mean maximum and minimum principal strains within the ROIs were calculated. Percentage differences of the volume weighted mean strains in ROIs were calculated in each LCP18 model using the corresponding LCP14 model as the reference. In PFP and DSAP-implanted models, bony ROIs were also identified around the three distal diaphyseal screws and the four condylar screws, as well as in the distal metaphyseal shaft of the femur. Similarly, elemental volume weighted mean maximum and minimum principal strains in those ROIs were compared between PFP and DSAP models, while percentage differences in mean strains were calculated in the DSAP model of each specimen using the PFP model as the reference.

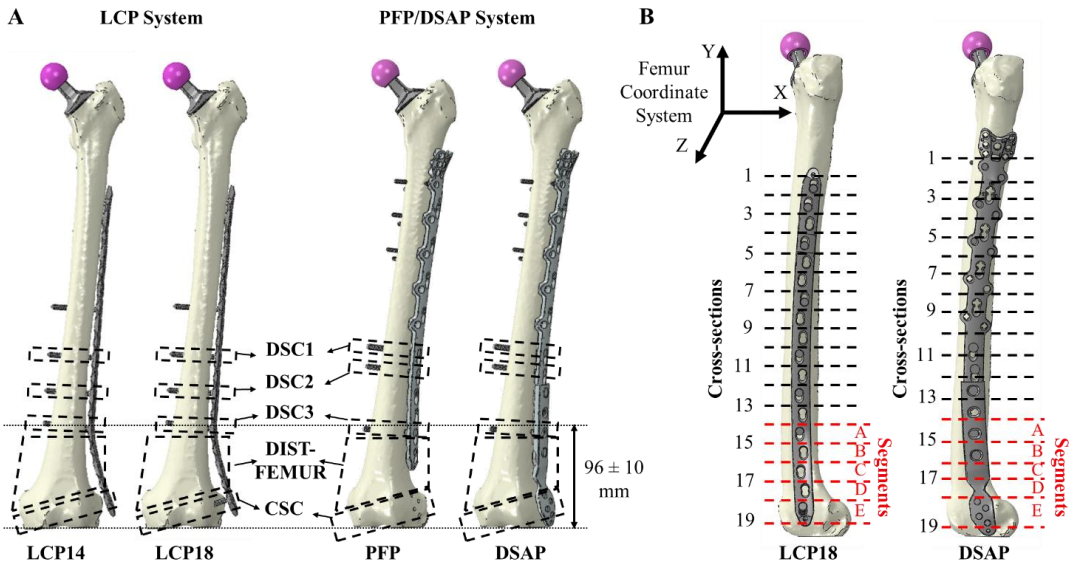

Fig. 4.3. FE models of two plating systems and two construct lengths. **(A)** FE models of a cadaveric femur (specimen 2) that was implanted with the LCP and the novel PFP/DSAP constructs. Bony ROIs around three distal diaphyseal screws and the condylar screws, as well as the DIST-FEMUR ROI, are shown. Note that the plate in LCP14 was not in contact with the bone below the most distal screw (or below the DSC3 ROI). **(B)** In LCP models, evenly spaced plate cross-sections were defined perpendicular to the Y axis based on the locations of screw holes. Though not evenly spaced, plate cross-sections in PFP and DSAP models were defined based on the locations of screw holes. Local compressive stiffness was calculated in 18 consecutive segments (divided by the 19 cross-sections), with focuses on the distal A to E segments.

Transfer of compressive load through the plate was calculated as the resultant compressive force in 19 cross-sections along the length of the plate (Fig. 4.3B). Load transfer in the plate was compared across four plate-implanted conditions in each specimen.

The model of the entire bone-implant system was divided into 18 consecutive segments using the 19 cross-sections described previously. The local compressive stiffness in each segment was calculated as the relative displacement of each segment divided by the applied 1200 N external force. Specifically, the relative displacement of each segment was calculated as the difference in displacement between the top and the bottom cross-sections that divided each segment. Local compressive stiffness was compared between two plating systems and two construct lengths, with focuses on the distal segments.

4.2.5 MODELING OF PHYSIOLOGICAL GAIT LOADS

To investigate the fixation and the load transfer under physiological loads, gait-loading was simulated using FE models of both plating systems. Peak hip contact force and femoral muscle forces during gait (taken at the toe-off stage in the stance phase of gait) were calculated using a musculoskeletal model and applied to the validated FE models of plate-implanted femurs (Fig. 4.4) (Myers et al., 2018). Muscle forces were modeled as distributed loads and applied over designated surface areas (centered at the insertion point of each muscle, Fig. 4.4) (Chen et al., 2021). Maximum and minimum principal strains in previously described ROIs were calculated in plate-implanted models. Load transfer through the plate was calculated and compared between both plating systems and the two construct lengths.

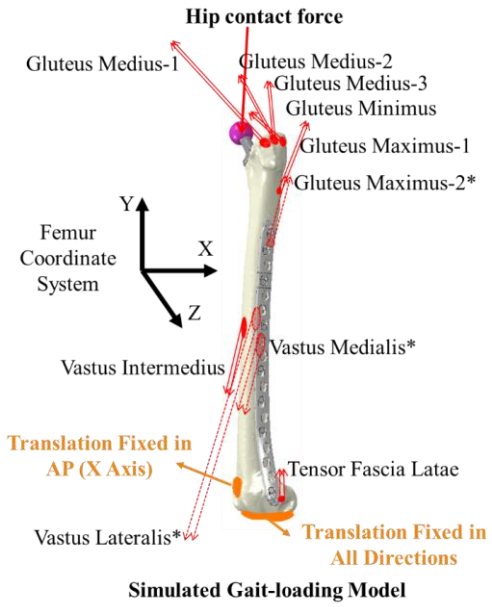

Force (Percentage BW)	
Hip Contact Force	269%
Gluteus Medius – 1	77%
Gluteus Medius – 2	39%
Gluteus Medius – 3	39%
Gluteus Maximus -1	33%
Gluteus Maximus -2	8%
Gluteus Minimus	16%
Vastus Lateralis	97%
Vastus Intermedius	23%
Vastus Medialis	29%
Tensor Fascia Latae	13%

Fig. 4.4. The gait-loading FE model of a LCP18 implanted cadaveric femur (specimen 2). Vectors of the hip contact force and the muscle forces are shown. The gait-loading model was constrained at nodes in medial and lateral condyles in all translations, and at nodes in the patellofemoral articulation in anterior/posterior (AP) translation.

4.3 RESULTS

4.3.1 VALIDATION OF IMPLANTED FEMUR FE MODELS

Magnitude of bone and plate displacement varied across the three specimens, with specimen three showing the highest overall displacement (Fig. 4.5A and C). Under the peak load of mechanical testing, implantation of the PFF fixation construct was shown to consistently reduce the displacement of bone markers compared to the THA implanted femurs (Fig. 4.5A). The condyle-spanning construct (LCP18) did not show appreciable differences in displacement as compared with the diaphyseal construct (LCP14) (Fig. 4.5).

Using the mean first coefficient in density-modulus relationship for bone, FE models of the implanted conditions showed good agreement with the experimentally measured marker displacement across three specimens (Fig. 4.5).

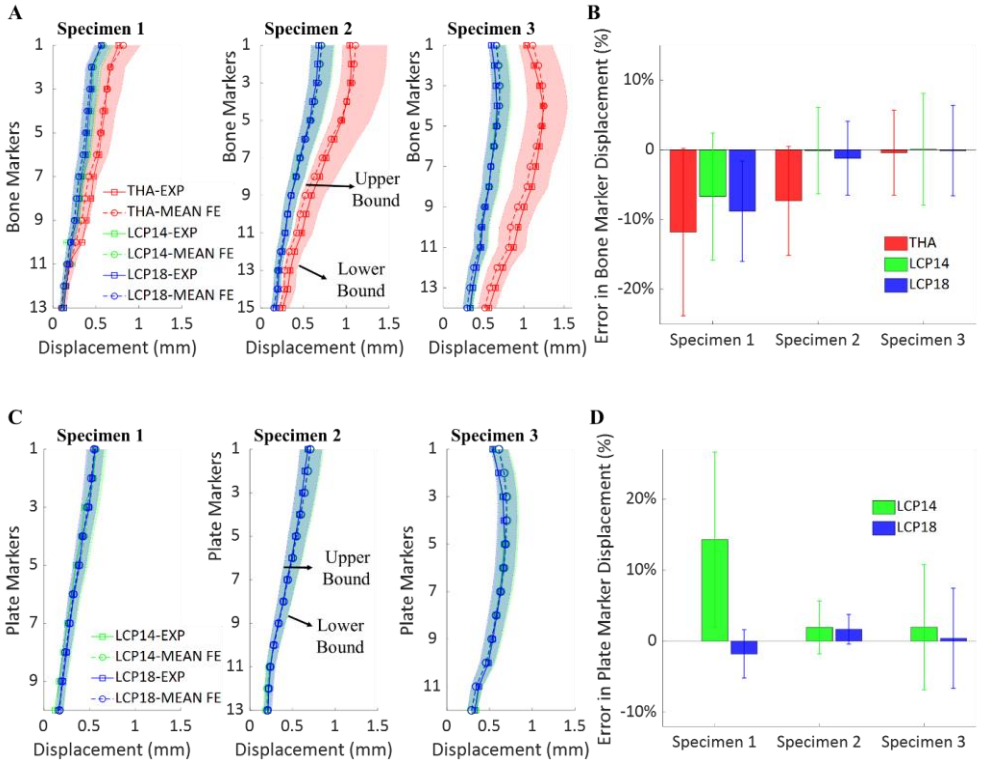

Fig. 4.5. Validation of FE models of three specimens using experimentally measured displacement of bone and plate markers. **(A)** Bone marker displacement. **(B)** Percentage errors in FE predicted bone displacement (mean ± standard deviation across all markers in each specimen). **(C)** Plate marker displacement. **(D)** Percentage errors in FE predicted plate displacement (mean ± standard deviation across all markers in each specimen). FE models simulated variances in bone property using the mean, and the lower and upper bounds of the 95% confidence interval of the first coefficient in the density-modulus relationship (Morgan et al., 2003). FE predicted ranges of displacement are shown (A and C).

Compared with the experiment, mean percentage errors in FE-predicted bone marker displacement were -7.2 ± 8.8%, -1.7 ± 8.2% and -3.4 ± 7.1% for THA, LCP14 and LCP18 across three specimens, respectively (Fig. 4.5B). Mean percentage errors in plate marker displacement were 5.4 ± 10.0% and 0.3 ± 4.7% for LCP14 and LCP18, respectively (Fig. 4.5D). Simulations using different first coefficients in the density-modulus relation showed how varied bone property affected FE predicted displacement (Fig. 4.5A and C). As expected, models using the lower bound of the coefficient resulted in the highest displacement across all implanted conditions, while the upper bound showed the lowest magnitude of displacement (Fig. 4.5A and 5C). In general, the mean coefficient (mean FE in Fig. 4.5) showed the best overall match in marker displacement as compared to the experimental displacement.

4.3.2 COMPARISONS OF MODEL PREDICTED BONE STRAINS AMONG DIFFERENT FIXATION CONSTRUCTS

Magnitude of principal strains varied across three specimens (Fig. 4.6). Specimen 3 showed overall higher magnitude of maximum and minimum principal strains than specimens 1 and 2 (Fig. 4.6). Across five ROIs, the highest magnitude of strains was consistently observed in the CSC ROI, with the condyle-spanning constructs (DSAP and LCP18) showing higher strains than the corresponding shorter diaphyseal constructs (PFP and LCP14) (Fig. 4.6).

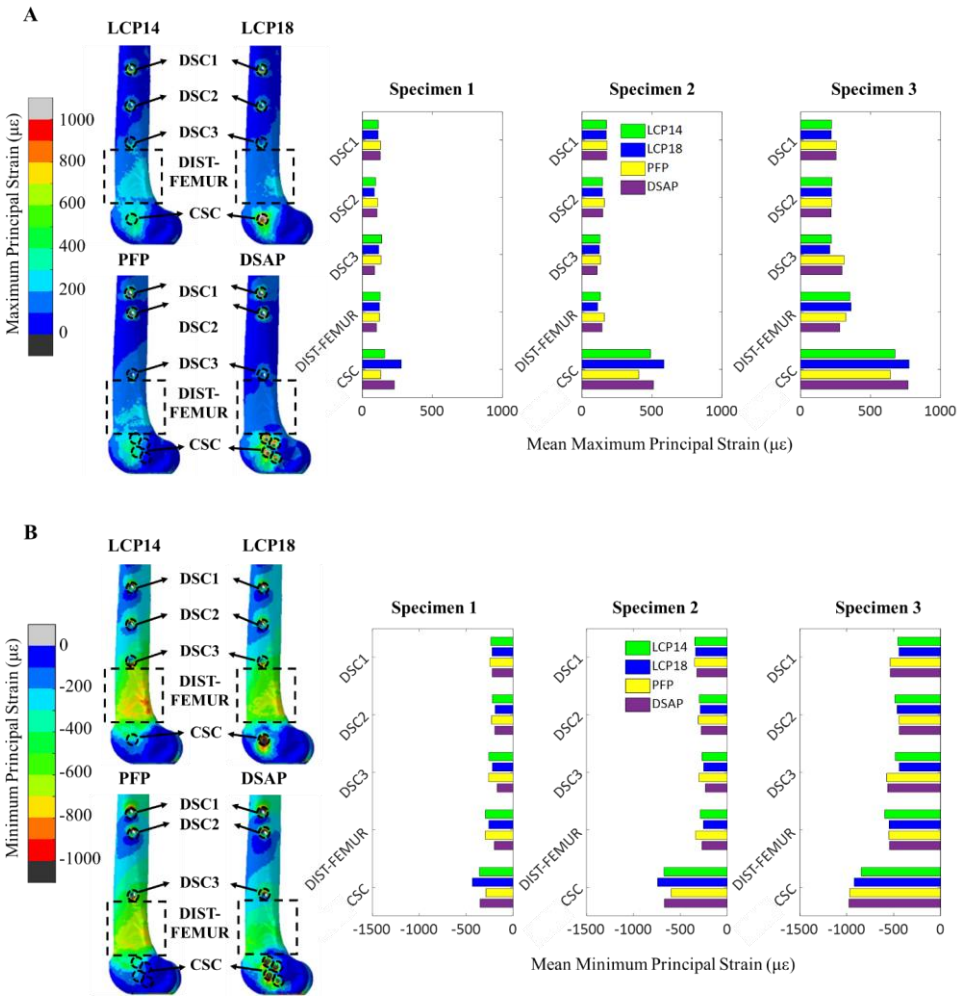

Fig. 4.6. Comparisons of maximum **(A)** and minimum **(B)** principal strains in ROIs between two plating systems and two construct lengths under the peak load of mechanical testing.

In contrast, LCP18 and DSAP models (condyle-spanning constructs) consistently showed reduced mean maximum and minimum principal strains in ROIs of DSC1, DSC2, DSC3 and DIST-FEMUR as compared with LCP14 and PFP (diaphyseal constructs) models, respectively (Table 4.1). The highest percentage reduction in both maximum and

minimum principal strains were observed in DSC3 in both LCP18 (-11.8 ± 4.9% in maximum principal strain, and -11.8 ± 2.5% in minimum principal strain) and DSAP (-19.0 ± 11.9% in maximum principal strain, and -20.1 ± 13.8% in minimum principal strain) models, with the DSAP models showing greater strain reductions compared with the LCP18 models (Table 4.1). The DSAP models also showed greater strain reductions compared with the LCP18 models in the DIST-FEMUR ROI (-13.8 ± 3.2 % in DSAP compared with -0.8 ± 2.5 % in LCP18 in maximum principal strain; -17.9 ± 12.7% in DSAP compared with -9.6 ± 2.1% in LCP18 in minimum principal strain). LCP18 and DSAP models consistently showed increases in mean principal strains in the CSC ROI as compared with the corresponding LCP14 and PFP models (Table 4.1).

ROIs	Percentage Difference in Maximum Principal Strain*				Percentage Difference in Minimum Principal Strain*			
	Simulated Mechanical Testing		Simulated Gait-loading		Simulated Mechanical Testing		Simulated Gait-loading	
	LCP18 vs LCP14	DSAP vs PFP	LCP18 vs LCP14	DSAP vs PFP	LCP18 vs LCP14	DSAP vs PFP	LCP18 vs LCP14	DSAP vs PFP
DSC1	-1.0 ± 0.3 %	-1.1 ± 0.5 %	1.7 ± 1.5 %	1.0 ± 5.1 %	-3.9 ± 1.2 %	-5.8 ± 4.2 %	-0.7 ± 1.7 %	-1.3 ± 3.7 %
DSC2	-5.2 ± 3.5 %	-4.6 ± 2.1 %	-7.7 ± 4.1 %	-4.4 ± 1.8 %	-8.1 ± 3.6 %	-8.6 ± 6.1 %	-8.7 ± 3.9 %	-5.9 ± 1.3 %
DSC3	-11.8 ± 4.9 %	-19.0 ± 11.9 %	-22.1 ± 8.6 %	-24.8 ± 11.5 %	-11.8 ± 2.5 %	-20.1 ± 13.8 %	-21.4 ± 5.4 %	-26.6 ± 10.5 %
DIST-FEMUR	-0.8 ± 2.5 %	-13.8 ± 3.2 %	-10.8 ± 5.4 %	-15.9 ± 5.2 %	-9.6 ± 2.1 %	-17.9 ± 12.7 %	-19.1 ± 2.0 %	-25.7 ± 4.5 %
CSC	36.1 ± 26.6 %	40.1 ± 24.6 %	28.9 ± 2.0 %	1.8 ± 2.7 %	13.3 ± 5.5 %	11.2 ± 8.2 %	6.5 ± 2.4 %	-3.9 ± 2.0 %

Table 4.1. Percentage differences in mean principal strains are shown between the diaphyseal and the condyle-spanning constructs of two plating systems. *A negative value indicates a reduction in strain.

Similar to models applying the peak load in mechanical testing, gait-loading models of condyle-spanning constructs (LCP18 and DSAP) consistently showed strain reductions in ROIs of DSC2, DSC3 and DIST-FEMUR compared with the diaphyseal constructs (LCP14 and PFP, respectively; Fig. 4.7 and Table 4.1). In contrast to mechanical testing, gait-loading models generally showed higher magnitude of mean maximum and minimum

principal strains in all ROIs, with smaller differences across different ROIs (Fig. 4.7). The amount of strain reductions was generally higher in the gait-loading LCP18 and DSAP models as compared with models of mechanical testing, especially in ROIs of DSC3 and DIST-FEMUR (Table 4.1).

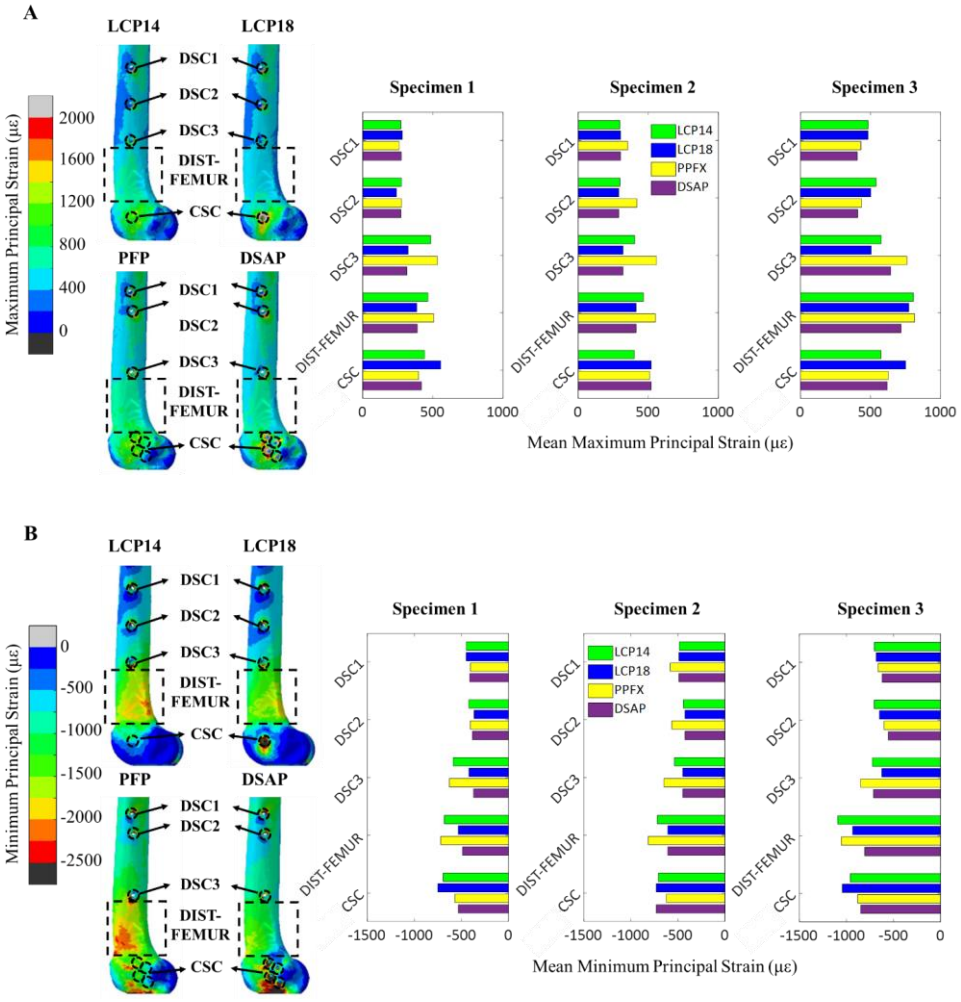

Fig. 4.7. Comparisons of maximum **(A)** and minimum **(B)** principal strains in ROIs in models between two plating systems and two plate lengths under gait-loading.

Under gait-loading, the DSAP models showed higher levels of strain reductions in DSC3 and DIST-FEMUR compared with the LCP18 models (Table 4.1). Increases in mean principal strains were consistently observed in the CSC in LCP18 models as compared with LCP14 models. DSAP models showed considerably less increases in maximum principal strain in CSC as compared with LCP18 models (1.8 ± 2.7% in DSAP compared with 28.9 ± 2.0% in LCP18, Table 4.1), while showing decreased mean minimum principal strain (-3.9 ± 2.0% in DSAP compared with 6.5 ± 2.4% in LCP18, Table 4.1).

4.3.3 COMPARISONS OF LOCAL STIFFNESS AMONG DIFFERENT FIXATION CONSTRUCTS

Under the peak load of mechanical testing, a sudden drop of the local compressive stiffness was observed in both diaphyseal constructs in segment B (the first segment located below the diaphyseal plate, Fig. 4.8A) as compared with the proximal neighboring segment A (a reduction of 53.2 ± 12.1% in LCP14, and a reduction of 44.2 ± 9.5% in PFP, Fig. 4.8A). In contrast, the local compressive stiffness in condyle spanning constructs maintained relatively consistent through segments A to E (Fig. 4.8A).

The condyle spanning constructs consistently showed increased local compressive stiffness as compared with the shorter diaphyseal constructs across segments A to E (Fig. 4.8B). Under the peak load of mechanical testing, the peak percentage increase in local compressive stiffness was observed in segment B (117.3 ± 52.1% and 151.1 ± 107.1% in LCP18 and DSAP, respectively). Similarly, the condyle-spanning constructs were shown to increase the local compressive stiffness under simulated gait-loading (Fig. 4.8C).

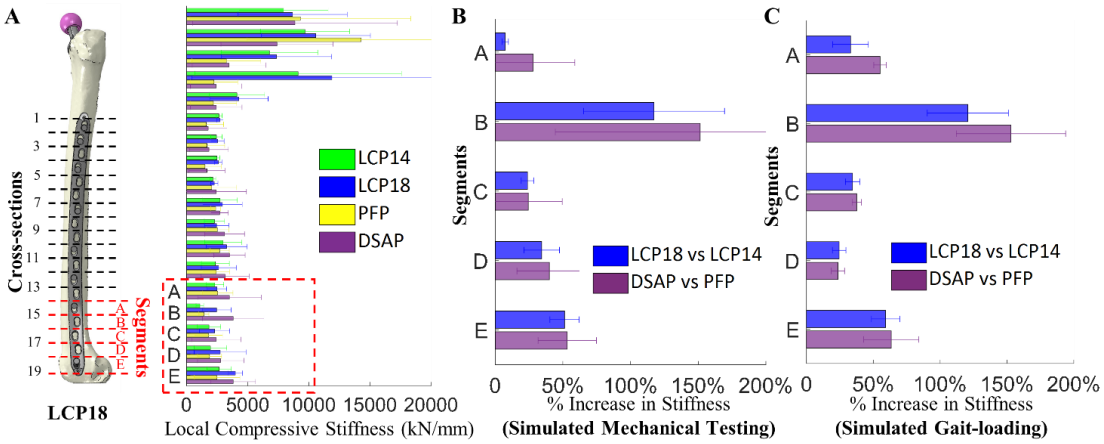

Fig. 4.8. Comparisons of local compressive stiffness and the increases in local compressive stiffness in condyle-spanning constructs. **(A)** Local compressive stiffness of bone-implant systems (LCP14, LCP18, PFP and DSAP) was calculated in 18 consecutive segments (defined using the 19 cross-sections), with focuses on the five distal segments (A to E). **(B)** Increases in local compressive stiffness (mean ± standard deviation across three specimens) in LCP18 and DSAP under peak load of mechanical testing as compared with LCP14 and PFP, respectively. **(C)** Increases in local compressive stiffness (mean ± standard deviation across three specimens) in LCP18 and DSAP under gait-loading.

4.3.4 COMPARISONS OF LOAD TRANSFER AMONG DIFFERENT FIXATION CONSTRUCTS

Tension (in the positive Y-direction of the femur coordinate system) was observed through the proximal cross-sections of the plate (proximal to cross-section 11, Fig. 4.9A and B), whereas compression (in the negative Y-direction) was observed through distal cross-sections of the plate (cross-sections 11 through 18, Fig. 4.9A and B). When tension was observed at a plate cross-section, higher compression was transferred through the bone

compared to the magnitude of compressive force in the system at the same cross-section (Fig. 4.9A). Through stiffening the entire bone-implant system, the proximal portion of the plate provided more compressive force to the bone, whereas the distal portion of the plate functioned to share the compressive force that was transferred through the system (Fig. 4.9A).

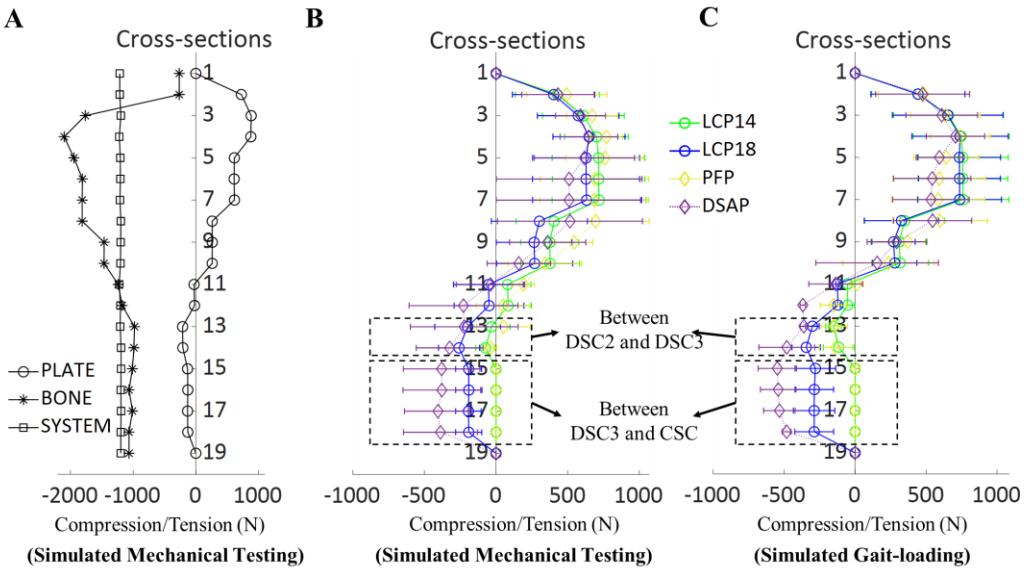

Fig. 4.9. Comparisons of load transfer among two plating systems and two construct lengths. **(A)** As an example, load transfer in compression(-)/tension(+) through cross-sections in the plate, the bone and the entire bone-implant system are shown in a LCP18 implanted model under the peak load of mechanical testing (specimen 2). **(B)** Comparisons of load transfer (mean ± standard deviation across three specimens) in compression(-)/tension(+) through the plate in different constructs (LCP14, LCP18, PFP and DSAP) under the peak load of mechanical testing. **(C)** Comparisons of load transfer (mean ± standard deviation across three specimens) in compression(-)/tension(+) through the plate in different constructs under gait-loading.

Both in mechanical testing and under loads of simulated gait, the condyle-spanning constructs enabled load transfer to the lateral condyle through the condylar screws (Fig. 4.9B and C). Compared with the diaphyseal constructs (LCP14 and PFP), the condyle-spanning constructs (LCP18 and DSAP) were shown to share more compressive load in cross-sections between DSC2 and DSC3 (Fig. 4.9B and C). In addition, the DSAP construct was shown to share more compressive load compared with LCP18 in cross-sections between DSC2 and DSC3 and between DSC3 and CSC (Fig. 4.9B and C), especially under gait-loading (Fig. 4.9C).

4.4 DISCUSSION

FE models of THA and PFF fixation construct implanted femurs were developed and validated for three cadaveric specimens by accurately representing the experimentally-measured displacement of bone and plate markers. Through increasing the local compressive stiffness and lowering the resultant compressive load in the distal diaphyseal and metaphyseal shaft of the femur, the condyle-spanning constructs of two different plating systems both showed potentially lowered risks of bone damage in ROIs as compared with their corresponding diaphyseal constructs.

By accurately replicating the *in situ* position of implants, FE models were able to differentiate bone and plate displacement in different specimens and implanted conditions. Simulations using different first coefficients in the density-modulus relationship allowed evaluations of the sensitivity of FE-predicted displacement relative to the uncertainty in material models for bone. Though models using the mean first coefficient generally

achieved the best match to the experimental displacement in this study, models of specimen 1 showed higher mean percentage errors as compared with specimens 2 and 3 (Fig. 4.5B and 4.5D).

Clinically, increasing the construct length in PFF fixation has shown benefits in mitigating the risks of secondary femoral fractures in the distal diaphyseal shaft of the femur (Bryant et al., 2009; Moloney et al., 2014). Using experimentally validated FE models, this study showed that both condyle-spanning constructs of two plating systems (LCP18 and DSAP) were able to lower mean maximum and minimum principal strains in ROIs around distal diaphyseal screws (DSC2 and DSC3), and in the distal metaphyseal shaft of the femur (the DIST-FEMUR ROI). The reduction of local maximum principal strain in bone is indicative of lowered risks of fracture in femurs implanted with condyle-spanning constructs (Choi et al., 2010; Lever et al., 2010; Moazen et al., 2013). Meanwhile, the reduction of minimum principal strain is indicative of lower risks of screw loosening, which has been associated with compromised integrity of plate fixation that could modify patterns in load transfer with elevated local strains in neighboring fixation locations (Feng et al., 2019; Panagiotopoulos et al., 1994; Sugiura et al., 2000). Modeling of gait loading allowed the assessment of PFF fixation mechanics under physiological conditions. Compared with the uniaxial load in mechanical testing, higher levels of strain reduction were indicative of increased efficacy of the condyle-spanning constructs (LCP18 and DSAP) in mitigating the risks of bone damage in ROIs of DSC2, DSC3, and DIST-FEMUR under gait loads. Between the two different PFF plating systems, The VA-LCP Periprosthetic Proximal Femur Plating System construct (DSAP) was shown to be more

effective in lowering the risks of bone damage in DSC3 and DIST-FEMUR compared with the LCP18 construct.

It was hypothesized that a longer plating construct that extends to the lateral condyle of the femur would distribute the load more evenly, therefore reducing local strains/stresses in the bone around the distal diaphyseal screws (Bryant et al., 2009; Moloney et al., 2014). In this study, the condylar fixation was shown to increase the local compressive stiffness in the distal diaphyseal and metaphyseal shaft of the femur, as well as enabled more load transfer through the distal portion of the plate. The increased stiffness combined with lowered compressive load in the distal diaphysis and metaphysis of the femur consequently resulted in lowered mean principal strains in ROIs.

Transfer of the compressive load through condylar screws was shown to result in elevated mean principal strains in the CSC ROI in femurs implanted with condyle-spanning constructs. However, different strategies in condylar fixation may mitigate the effect of elevated strains in the CSC ROI. Though more compressive load was transferred to the bone via condylar screws in DSAP models as compared with LCP18 models (Fig. 4.7), DSAP models showed fewer increases in mean principal strains in CSC ROIs (Table 4.1). Compared with the condylar fixation using a single 5.0-mm screw in the LCP18 construct, the DSAP construct utilized four 3.5-mm screws. The compressive load was transferred more evenly to the lateral condyle through a larger volume of bone in DSAP models, which could be associated with the lessened elevation in principal strains.

Several limitations of this study should be considered. The ROIs of bone strains were completely covered by the implanted plate in physical specimens; therefore this study

could not measure bone strains in ROIs in the experiment using the DIC system. This study used the DIC system to measure the displacement of bone and plate markers over almost the entire length of the implanted plate as well as the middle and distal shaft of the femur. Future studies may use alternative methods, such as surface strain gauges, to measure bone strains in ROIs.

4.5 CONCLUSION

Using experimentally validated FE models, this study demonstrated the biomechanical benefits of utilizing condyle-spanning constructs over the diaphyseal constructs in PFF fixation in mitigating risks of secondary femoral fractures. Different strategies in condylar fixation were shown to mitigate the potential strain elevations in the femoral lateral condyle. This study highlighted the importance of simulating physiological loads for the assessment of the biomechanics of PFF fixation. Future studies will apply similar strategies to investigate the biomechanics of PFF fixation in other common activities of daily living.

CHAPTER FIVE. IMPACT OF BONE HEALTH ON THE MECHANICS OF PLATE FIXATION FOR VANCOUVER B1 PERIPROSTHETIC FEMORAL FRACTURES

5.1 INTRODUCTION

Periprosthetic femoral fracture (PFF) is one of the leading causes of reoperation (approximately 6% of cases) after a total hip arthroplasty (THA) (Abdel et al., 2016; Duncan and Haddad, 2014; Lindahl et al., 2007; Marsland and Mears, 2012). The fracture around or just below the implanted THA stem (the Vancouver type B PFF) accounts for over 70% of all PFF cases (Marsland and Mears, 2012). With a stable THA stem (further classified as the type B1 PFF), implantation of a fracture fixation plate has proven to be a successful treatment to promote the healing of the primary PFF (Bryant et al., 2009; Moloney et al., 2014; Pletka et al., 2011; Shah et al., 2011). However, high incidences of femoral refractures (ranged 7% to 20%) have been reported clinically (Lindahl et al., 2006; Miettinen et al., 2021), with the refractures frequently occurring distal to the implanted plate (approximately 50% of all refracture cases) (Randelli et al., 2018). Femoral refractures require complex reoperation and have been reported to increase the rate of disability and mortality (Giovanni et al., 2020b; Lindahl et al., 2007, 2006; Randelli et al., 2018).

Clinically, a longer condyle-spanning plate-screw construct has been shown to reduce the risks of femoral refractures (Bryant et al., 2009; Moloney et al., 2014). Through simulating peak gait loading, a previous biomechanical modeling study by our group showed that condyle-spanning constructs reduced bone strains in the distal diaphysis and metaphysis as compared with shorter plates under physiological muscle loads (Chen et al., 2022a). However, those studies either only used healthy femurs, or did not quantify the health state of bone (Bryant et al., 2009; Chen et al., 2022a; Moloney et al., 2014). Patients with osteoporosis (accounts for over 25% of all THA patients) have been associated with increased risks of type B1 primary PFF, as well as complications after fixation of PFF (Franklin and Malchau, 2007; Glowacki et al., 2003; Karachalios et al., 2020; Labuda et al., 2008; Mäkinen et al., 2007; Reid, 2020; Sidler-Maier and Waddell, 2015). No study has thus far evaluated the mechanics of plate fixation in patients with osteoporosis.

In addition to the degraded bone strength hindering plate fixation, osteoporosis-associated muscle weakening may also affect the mechanics of the bone-implant system (Be'ery-Lipperman and Gefen, 2005; Rikkonen et al., 2012; Sinaki et al., 2005). Weakening of the major hip abductors (gluteus medius) and the knee extensors (the vastus muscles) have been typically reported in patients with osteoporosis (Be'ery-Lipperman and Gefen, 2005; Rikkonen et al., 2012; Sinaki et al., 2005). Weakening of those muscles has been associated with the Trendelenburg gait, i.e. slower gait and increased side sways, which has been shown to reduce hip abduction moment and loading at the knee (Brech et al., 2013; Henriksen et al., 2009; Mündermann et al., 2008; Sinaki et al., 2005; Weinhandl et al., 2017). Such modified muscle and joint loading may reduce stress and strain in THA

and plate implanted femur. However, since no clinical and biomechanical study has investigated modified muscle and joint loading in PFF fixation, it remains unclear how the mechanics of plate fixation may be affected.

Using experimentally-validated finite element (FE) models of THA and plate-implanted femurs, the mechanics of plate fixation were investigated for two plating systems and two construct lengths in both healthy and osteoporotic femurs. Through simulating peak loads of three common activities of daily living (ADLs: gait, stair-descent, and sit-to-stand), resulting bone strains and plate stress were evaluated and compared between two plating systems and two construct lengths in plate-implanted healthy and osteoporotic femurs. In addition, load transfer and stiffness of the bone-implant system were calculated to investigate the mechanisms underlying differences in bone strains between different plating systems and construct lengths.

5.2 METERIALS AND METHODS

5.2.1 CADAVERIC FEMURS AND DETERMINATION OF T-SCORE

Computed Tomography (CT) scans (0.72 mm X 0.72 mm X 0.60 mm, SIMENS, Munich, Germany) of six fresh frozen cadaveric femurs were used for the development of coupled musculoskeletal and finite element models. Three of the six selected cadaveric femurs (all left; two males, one female; age, 71.7±1.7; height, 169.4±6.4 cm; weight, 67.7±16.9 kg) were physically tested and numerically modeled in a previous study (Chen et al., 2022a). These three specimens did not show signs of bone damage or disease, thereby were denoted as ‘healthy’ subjects in the current study (Fig. 5.1A).

To compare with the three healthy specimens, three osteoporotic femurs were selected and modeled. Among the three osteoporotic femurs (all left; two females, one male; age, 84.0±3.6; height, 165.1±7.4 cm; weight, 59.9±15.9kg), one was physically tested and numerically modeled similar as the three healthy specimens, the remaining two were selected from an inhouse CT database of fresh frozen cadaveric specimens. CTs of osteoporotic femurs clearly showed radiographic porotic bone loss (Fig. 5.1A).

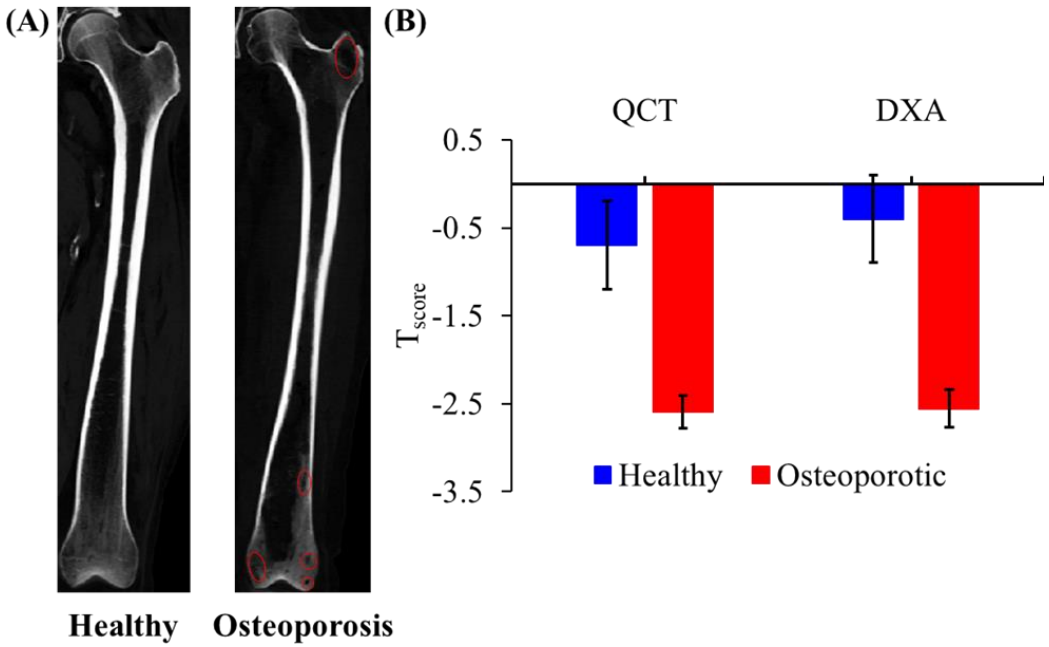

Fig. 5.1. Comparisons of the CT image and T-scores between healthy and osteoporotic femurs. **(A)** CT slices of a healthy femur (left) and an osteoporotic femur (right). Red ellipsoids indicated radiographically observed porotic bone loss. **(B)** Comparisons of CT derived T scores between the healthy and osteoporotic femurs.

Analyses were conducted to determine T-scores for the femurs using a previously established method (Varga et al., 2016). The CT Hounsfield units (HUs) were converted into volumetric bone mineral density units (vBMD) using specimen-specific calibration equations determined from a five-material density phantom (Model 3, Mindways Software Inc, Austin, TX, USA) according to the specifications of the phantom manufacturer (Eq. 1). Note that coefficients in Eq. 1 were the mean values from CTs of six specimens. The femurs were segmented semi-automatically on the resulting quantitative CT (QCT) images using Amira software (v6.3, FEI Company, Hillsboro, Oregon, USA). Anatomical landmarks including head center, neck axis and shaft axis were identified using a custom-developed algorithm implemented in GNU Octave 3.8.2 (www.gnu.org/software/octave/), utilizing tools from Fiji (Schindelin et al., 2009) with the BoneJ plugin (Doube et al., 2010) and the Insight Segmentation and Registration Toolkit (ITK, www.itk.org). Based on these landmarks, the QCT images were aligned with the anatomical axes of femurs. Areal bone mineral density (aBMD, in mg/cm^2) of the proximal femur was calculated by dividing the summed bone mineral content by the projected area. The latter was determined by projecting the QCT image along the anterior-posterior axis into a 2D image and measuring the area of the projected mask. The resulting densities were corrected to account for differences between QCT-based and dual X-ray absorptiometry (DXA)-based aBMD and then converted into T-scores using the relationships proposed by Khoo et al. (Khoo et al., 2009). The osteoporotic femurs showed much lower QCT-based T-scores (-2.6 ± 0.2) and DXA-based T-scores (-2.6 ± 0.2) than the healthy femurs (QCT-based T-score: -0.7 ± 0.5; DXA-based T-score: -0.4 ± 0.5). Those T-scores agreed well with the reported range for

osteoporotic femurs (below -2.5) and healthy femurs (above -1.0) (Khoo et al., 2009; Mäkinen et al., 2007).

$$\text{vBMD}\ (\text{g/cm}^3) = -0.02184 + 0.8242 * \text{HUs} \quad \text{Eq. 1}$$

5.2.2 DEVELOPMENT AND VALIDATION OF THA AND PLATE IMPLANTED FE MODELS OF CADAVERIC FEMURS

The development of THA and plate implanted FE model used the same method as described in detail previously (Chen et al., 2022a). Briefly, three healthy femurs and one osteoporotic femur were physically implanted with a THA femoral component (Corail®, DePuy Synthes, Warsaw, IN, USA) and the Locking Compression Plating system (LCP system, DePuy Synthes, West Chester, PA, USA) that had a diaphyseal configuration and a condyle-spanning configuration. In the diaphyseal LCP construct, the 4.5 mm Curved Broad LCP was fixed to each femur using six 5.0-mm locking screws, with the most distal screw implanted through the 14th hole on the plate (hence the LCP14 construct, Fig. 5.2A). The condyle-spanning construct included an additional 5.0-mm locking screw that was implanted into the lateral condyle of each femur through the most distal screw hole (the 18th hole) on the LCP (hence the LCP18 construct, Fig. 5.2A). The THA and LCP implanted femur FE models accurately replicated the *in situ* implant positions using 3D scans of the physical specimens as references (Fig. 5.2A).

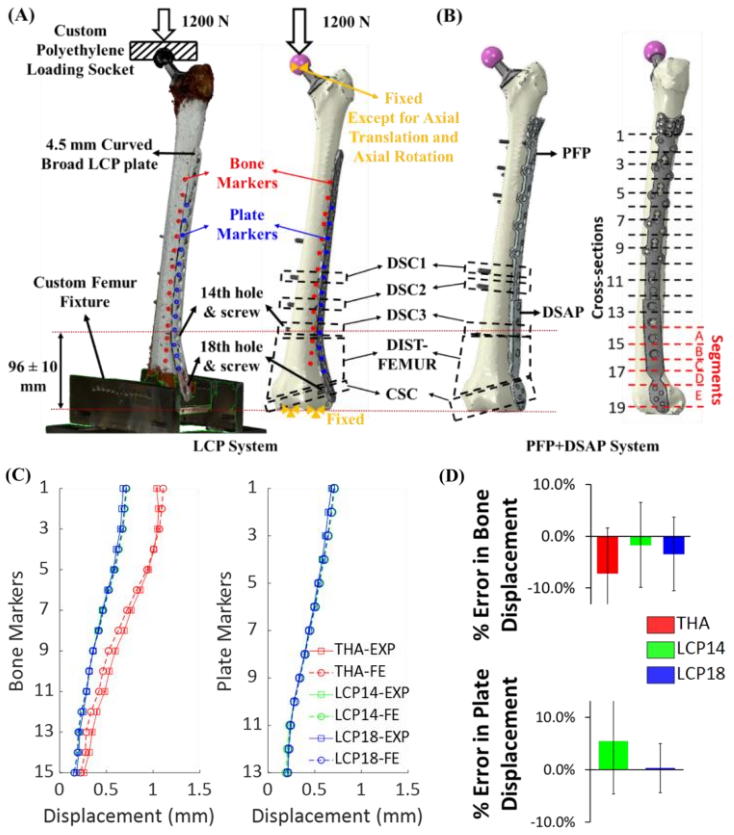

Fig. 5.2. Experimental validation of models of THA and plate implanted femurs. **(A)** Left, 3D scanned geometries of a physically-implanted femur (THA and the LCP construct) in the setup of mechanical testing. Right, the FE model of the THA and LCP18-implanted femur. **(B)** FE models of a femur that was implanted with the PFP+DSAP system. Left, locations of bone strain ROIs (DSC1, DSC2, DSC3, and CSC are 10 mm diameter cylindrical volumes centered at the axis of each screw). Right, 19 cross-sections for the calculation of load transfer through the bone-implant system. Stiffness of the bone-implant system was calculated in segments along the femur, with focuses on the distal five segments (A through E). **(C)** Comparisons of displacement of bone and plate markers between experimentally-measured and FE-predicted values. **(D)** Percentage errors of FE-predicted displacement relative to the measured values.

Since the remaining two osteoporotic femurs did not have physical references, virtual implantations of THA and the LCP constructs mimicked the positions in those physical specimens. The orientation and the size of the THA stem was determined by the shape of the femoral canal, with the position of the THA head center coincidental with the native femoral head center. The LCP constructs were implanted to the lateral surface of femur with the same screw locations as in those physical specimens (Fig. 5.2A). In particular, the most distal screw in the LCP14 model maintained the same location as in those physical specimens (96 ± 10 mm above the bottom fixation surface of each specimen, Fig. 5.2A).

The femur, the THA component, the plate and the screw were meshed using 10-noded tetrahedral elements in Abaqus 2018 (Dassault Systèmes, Vélizy-Villacoublay, France) using mean edge lengths of 2 mm, 2 mm, 1 mm, and 0.5 mm, respectively. A finer local mesh size (0.5 mm edge length) was used to mesh the bone elements at the bone-screw interface to estimate strains in the high gradient region. The edge lengths were determined through a previous mesh convergence study (Chen et al., 2022a). Given lack of relative displacement observed during physical testing, fully-bonded interfaces were modeled for bone-stem, bone-screw and plate-screw interfaces.

The cobalt-chrome THA component (Young's modulus: 210 GPa; Poisson's ratio: 0.29) (Weinans et al., 1992), the stainless steel fracture fixation plate and screws (Young's modulus: 149 GPa; Poisson's ratio: 0.3) (ASTM F138-13a, 2013) were modeled as linear elastic.

Bone was modeled as nonhomogeneous linear elastic materials (with a constant Poisson's ratio of 0.3). Young's moduli of bone were interpolated from CT HUs and the

density phantom using previously established relationships in 50 MPa intervals (Eq. 1 to 4) (Morgan et al., 2003; Schileo et al., 2008; Taddei et al., 2007).

$$\text{Ash Density } (g/cm^3) = 0.8772 * \text{vBMD} + 0.07895 \quad \text{Eq. 2}$$

$$\text{Apparent Density } (g/cm^3) = \text{Ash Density} / 0.6 \quad \text{Eq. 3}$$

$$\text{Young's Modulus (MPa)} = 6850 * \text{Apparent Density}^{1.49} \quad \text{Eq. 4}$$

The THA and LCP implanted FE models (LCP14 and LCP18) of the three healthy femurs and one osteoporotic femur were validated using experimentally-measured bone and plate displacement from a previously developed protocol (Chen et al., 2022a). The implanted-femurs were fixed at the distal femur in 3° extension and 3° valgus and subjected to a 1200 N uniaxial compressive force applied through the THA femoral head (Fig. 5.2A). Bone and plate displacement were measured using the markers of a digital imaging correlation system (GOM, Braunschweig, Germany) that were glued to the anterolateral surfaces of the femur and the implanted plate. FE-predicted displacement agreed with the experimentally-measured marker displacement (Fig. 5.2C), achieving less than ±10% mean percentage error (Fig. 5.2D).

After validation against physically-measured bone and plate displacement (LCP14 and LCP18 configurations), the PFP+DSAP system (3.5/4.5 mm VA-LCP Proximal Femur Plate combined with the modular 3.5 mm Distal Femur Spanning Attachment Plate, DePuy Synthes, West Chester, PA, USA) was virtually implanted into the femur FE models. To compare with the diaphyseal LCP14 models, the most distal screw in the 3.5/4.5 mm VA-LCP Proximal Femur Plate (PFP) implanted models maintained the same location as in

LCP14 models (96 ± 10 mm above the bottom fixation surface of each femur, Fig. 5.2A and B). The modular Distal Femur Spanning Attachment Plate (DSAP) was then attached to the PFP plate using two connecting screws and was fixed to the lateral condyle of each femur using four 3.5-mm locking screws to complete the condyle-spanning DSAP construct (Fig. 5.2B). Implanted FE models (THA, LCP and PFP+DSAP) were developed similarly for the remaining two osteoporotic femurs.

5.2.3 MODELING OF PHYSIOLOGICAL ADL LOADS

Physiological loadings of three common ADLs (gait, stair-descent and sit-to-stand) were simulated to compare bone strain, load transfer and local stiffness of the bone-implant system between the healthy and the osteoporotic femurs. The hip contact force and femoral muscle forces were calculated in each ADL (with the focus on the instance of peak hip contact force) using a coupled musculoskeletal and FE model (Chen et al., 2022b, 2021; Myers et al., 2018). The peak hip contact force was applied through the THA femoral head, while muscle forces were modeled as distributed loads and applied over designated surface areas (centered at the insertion point of each muscle, Fig. 5.3). Before applying to FE models of each specimen, magnitudes of the hip contact force and muscle forces were scaled to the body weight of each specimen. These initially applied physiological forces were referred as ‘the normal muscle forces’ to distinguish from the later simulation of osteoporosis associated muscle weakening.

To simulate osteoporosis associated muscle weakening, the normal forces of hip abductors and knee extensors were reduced to 70% of the previously calculated magnitude

(Sinaki et al., 2005). Weakened forces of hip abductors and knee extensors altered the resultant force and moment in the bone-implant system, the magnitude of the hip contact force and forces of other major muscles were adjusted using a previously developed FE integrated optimization approach to reestablish force and moment balance in the bone-implant system (Chen et al., 2021). The adjusted muscle forces were thereby referred to as 'the weakened muscle forces', which were applied only in models of osteoporotic femurs.

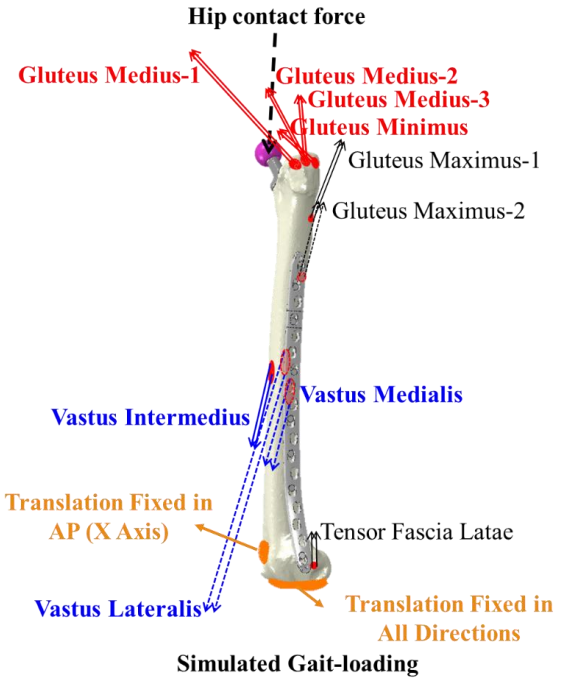

Hip Abductors
Knee Extensors
Other Muscles

ADL	Peak hip contact force (% body weight)
Gait	269%
Stair-descent	320%
Sit-to-stand	110%

Fig. 5.3. Simulated muscle forces are shown in a coupled musculoskeletal and FE model of a THA and plate implanted femur. The peak hip contact force was applied through the THA femoral head, while muscle forces were modeled as distributed loads and applied over designated surface areas. Forces of hip abductors (red) and knee extensors (blue) were decreased to 70% of the healthy capacity to simulate osteoporosis associated muscle weakening. Magnitudes of the peak hip contact force are shown for three simulated ADLs (right bottom).

To compare bone strain between the healthy and the osteoporotic models, as well as between different plating systems and different construct lengths, regions of interest (ROIs) were identified that contained bone elements around three distal diaphyseal screws and condylar screws in plate-implanted models (ROIs of DSC1, DSC2, DSC3, and CSC, which are 10 mm diameter cylindrical volumes centered at the axis of each screw, Fig. 5.2A and B) (Chen et al., 2022a). Additionally, a DIST-FEMUR ROI was defined at the distal femoral metaphyseal shaft (Chen et al., 2022b). Elemental volume weighted mean maximum and minimum principal strains within the ROIs were calculated. Percentage differences of the volume weighted mean strains in the ROIs were calculated in each LCP18 and DSAP implanted model using the corresponding LCP14 and PFP model as the reference, respectively. To compare the impact of plating (different plating systems and different construct lengths) between the healthy and the osteoporotic femurs, the percentage differences in strains between the diaphyseal and the condyle-spanning constructs were compared in both the healthy and the osteoporotic femurs.

Load transfer through the bone-implant system were calculated in implanted healthy and osteoporotic femurs, which was compared between two plating systems and two construct lengths. The calculation of load transfer focused on the compressive force (the major component of the resultant force) through 19 cross-sections that were determined based on the structure of the plate (Fig. 5.2B).

In addition, local compressive stiffness of the bone-implant system in the distal femur was calculated in healthy and osteoporotic femurs, and compared between two plating systems and two construct lengths (Eq. 5, Fig. 5.2B). Note in Eq. 5, the displacement of

each segment (e.g., the segment divided by cross-sections i+1 and i) was the relative displacement between two cross-sections.

$$\text{Local Stiffness (N/mm)} = Force/(Displacement_{i+1} - Displacement_i) \quad \text{Eq. 5}$$

5.3 RESULTS

5.3.1 COMPARISONS OF BONE STRAINS BETWEEN HEALTHY AND OSTEOPOROTIC MODELS

Applying 'the normal muscle forces', loads of stair-descent generally resulted in the highest mean maximum and minimum principal strains in both healthy and osteoporotic femurs across three simulated ADLs (Fig. 5.4A and C). The DIST-FEMUR or the DSC3 ROI in models implanted with shorter constructs (LCP14 and PFP) typically showed the highest mean strains across five ROIs in both healthy and osteoporotic femurs. In osteoporotic models, LCP14-implanted femurs showed the highest magnitude of strains in DIST-FEMUR (601.8 ± 224.5 με in maximum principal strain and -825.2 ± 261.2 με in minimum principal strain, compared with 448.3 ± 242.4 με and -658.9 ± 333.8 με in PFP-implanted healthy femurs, Fig. 5.5A). Between the condyle-spanning constructs of two plating systems, DSAP-implanted femurs typically showed slightly lower mean strains in DSC3 and DIST-FEMUR than LCP18-implanted femurs (especially in osteoporotic femurs, Fig. 5.5A).

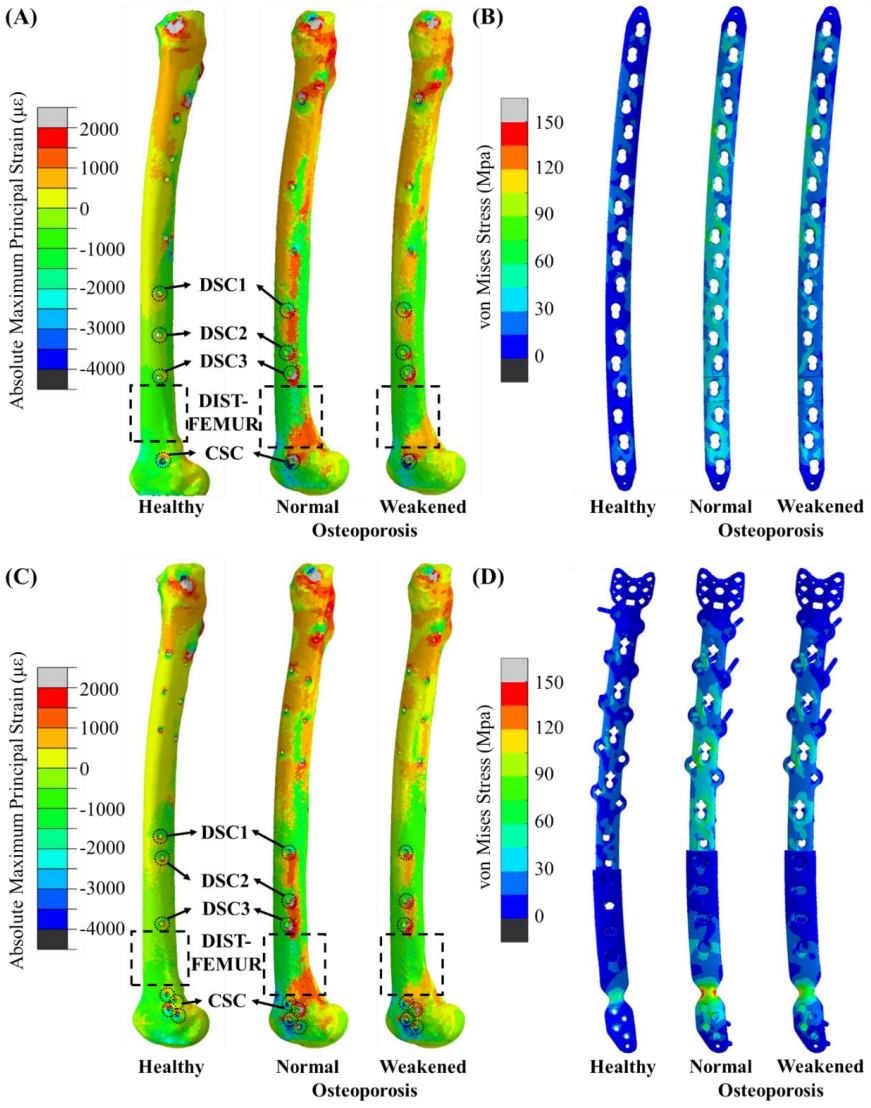

Fig. 5.4. Comparisons of bone strain and plate stress between a healthy and an osteoporotic femur (with a similar bodyweight of approximately 58 kg) under loads of simulated stair-descent. Results are shown for the osteoporotic model applying both 'the normal' and 'the weakened muscle forces'. **(A)** Absolute maximum principal strain in LCP18-implanted femurs. **(B)** Plate stress in LCP18-implanted femurs. **(C)** Absolute maximum principal strain in DSAP-implanted femurs. **(D)** Plate stress in DSAP-implanted femurs. Construct lengths showed little effect on the peak stress or stress distribution (data not shown).

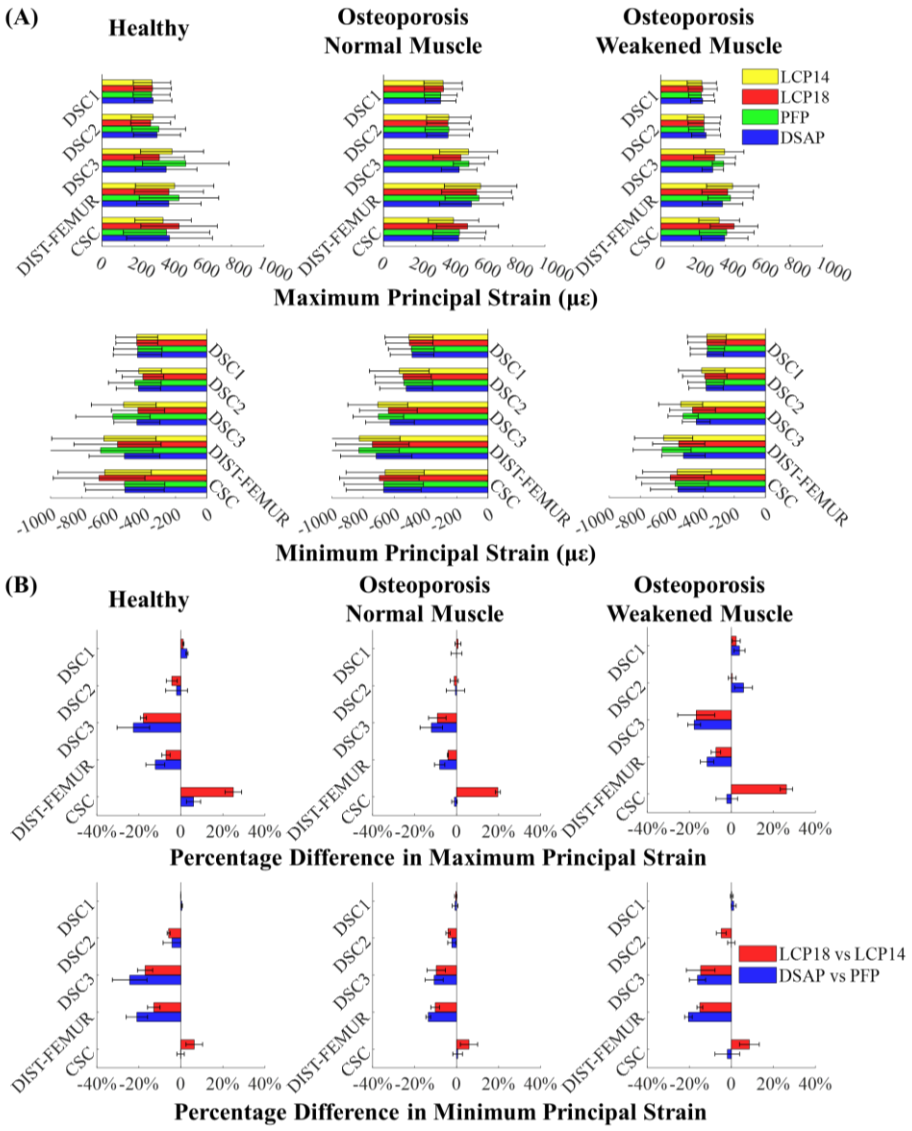

Fig. 5.5. Comparisons of principal strains among two plating systems and two plate lengths in healthy and osteoporotic femurs. **(A)** Mean maximum (top) and minimum (bottom) principal strains in ROIs (mean ± standard deviation across three specimens in each group) were compared in healthy and osteoporotic femurs under simulated loads of stair-descent. **(B)** Percentage differences in maximum (top) and minimum (bottom) principal strains between the diaphyseal and the condyle-spanning constructs (LCP18 versus LCP14 and DSAP versus PFP).

Across three ADLs, condyle-spanning constructs of two plating systems consistently reduced strains in DSC3 and DIST-FEMUR compared with their corresponding shorter constructs, with DSAP frequently showing greater reductions than LCP18 (Table 5.1, indicated in green background). In DIST-FEMUR (showed the highest mean maximum principal strain in osteoporotic femurs across five ROIs) under simulated loads of stair-descent, DSAP models reduced mean maximum principal strain (compared with PFP) by 12.2 ± 4.5% and 8.1 ± 2.5% in healthy and osteoporotic femurs, respectively (Table 5.1 and Fig. 5.5B). In contrast, LCP18 (compared with LCP14) showed 7.1 ± 2.0% reductions in heathy femurs and 4.1 ± 0.2% reductions in osteoporotic femurs (Table 5.1 and Fig. 5.5B). When applying 'the weakened muscle forces' in osteoporotic femurs, condyle-spanning constructs achieved greater strain reductions in DSC3 and DIST-FEMUR than the osteoporotic models applying 'the normal muscle forces' (approximately 5% more for both DSAP versus PFP and LCP18 versus LCP14, Table 5.1 and Fig. 5.5B).

In the most distal CSC ROI, LCP18 models of both healthy and osteoporotic femurs consistently showed increased strains as compared with LCP14 models (mean increases of 33.2% and 7.0% in maximum and minimum principal strains across three ADLs, respectively; Table 5.1). In contrast under simulated loads of gait and stair-descent, DSAP-implanted models showed relatively unchanged strains in healthy femurs, and even reduced strains in osteoporotic femurs in CSC (Table 5.1, indicated in blue background).

Gait												
	LCP18 vs LCP14						DSAP vs PFP					
	Maximum Principal Strain			Minimum Principal Strain			Maximum Principal Strain			Minimum Principal Strain		
ROIs	Healthy	Osteoporosis	Osteoporosis (weakened)	Healthy	Osteoporosis	Osteoporosis (weakened)	Healthy	Osteoporosis	Osteoporosis (weakened)	Healthy	Osteoporosis	Osteoporosis (weakened)
DSC1	2.0 ± 0.2%	1.6 ± 2.2%	3.3 ± 2.7%	0.5 ± 0.2%	0.2 ± 0.5%	0.8 ± 0.6%	3.4 ± 0.4%	1.5 ± 2.5%	5.2 ± 3.1%	1.0 ± 0.3%	0.4 ± 1.0%	1.9 ± 1.3%
DSC2	-1.9 ± 1.5%	-0.3 ± 1.4%	0.8 ± 1.6%	-4.6 ± 0.9%	-3.8 ± 2.6%	-5.1 ± 4.6%	0.1 ± 4.9%	2.4 ± 3.5%	8.7 ± 3.7%	-1.8 ± 3.1%	-0.2 ± 0.4%	1.7 ± 1.0%
DSC3	-21.1 ± 1.1%	-12.5 ± 9.7%	-18.5 ± 13.0%	-18.8 ± 4.2%	-11.8 ± 8.8%	-16.3 ± 10.5%	-17.9 ± 9.7%	-15.4 ± 3.7%	-20.8 ± 8.7%	-20.1 ± 8.1%	-12.1 ± 6.0%	-18.1 ± 7.4%
DIST-FEMUR	-9.5 ± 1.9%	-6.0 ± 1.5%	-9.0 ± 2.0%	-15.0 ± 2.2%	-12.1 ± 4.3%	-17.1 ± 3.0%	-11.9 ± 4.4%	-10.0 ± 1.4%	-13.8 ± 3.7%	-19.5 ± 4.2%	-15.1 ± 2.5%	-22.7 ± 2.7%
Mean-CSC	25.5 ± 4.4%	21.3 ± 4.2%	28.2 ± 4.0%	6.4 ± 3.9%	7.6 ± 6.2%	10.4 ± 6.2%	3.8 ± 2.7%	-2.3 ± 4.0%	-2.3 ± 6.5%	-1.7 ± 2.6%	-0.6 ± 4.5%	-2.2 ± 6.5%
Stair-descent												
	LCP18 vs LCP14						DSAP vs PFP					
	Maximum Principal Strain			Minimum Principal Strain			Maximum Principal Strain			Minimum Principal Strain		
ROIs	Healthy	Osteoporosis	Osteoporosis (weakened)	Healthy	Osteoporosis	Osteoporosis (weakened)	Healthy	Osteoporosis	Osteoporosis (weakened)	Healthy	Osteoporosis	Osteoporosis (weakened)
DSC1	1.2 ± 0.3%	0.7 ± 1.4%	2.3 ± 1.9%	-0.1 ± 0.0%	-0.4 ± 0.6%	0.2 ± 0.6%	2.9 ± 0.5%	-0.1 ± 2.6%	3.9 ± 2.6%	0.5 ± 0.3%	-0.7 ± 1.4%	1.1 ± 1.2%
DSC2	-4.3 ± 2.6%	-1.1 ± 1.9%	0.4 ± 1.8%	-5.8 ± 0.7%	-4.1 ± 1.0%	-4.8 ± 2.3%	-2.0 ± 5.2%	-0.5 ± 4.4%	5.8 ± 4.2%	-4.2 ± 4.2%	-2.3 ± 1.9%	-0.0 ± 1.7%
DSC3	-17.8 ± 1.4%	-9.2 ± 4.2%	-16.7 ± 8.8%	-17.0 ± 3.6%	-9.7 ± 4.4%	-14.6 ± 6.8%	-22.6 ± 7.7%	-12.0 ± 5.4%	-17.7 ± 3.1%	-24.4 ± 8.2%	-10.7 ± 4.3%	-16.1 ± 3.9%
DIST-FEMUR	-7.1 ± 2.0%	-4.1 ± 0.2%	-7.4 ± 2.3%	-12.9 ± 3.0%	-10.2 ± 2.0%	-15.0 ± 1.4%	-12.2 ± 4.5%	-8.1 ± 2.5%	-11.6 ± 3.2%	-20.9 ± 5.1%	-13.5 ± 1.1%	-20.4 ± 1.8%
Mean-CSC	25.0 ± 4.0%	19.7 ± 1.2%	26.2 ± 2.9%	6.4 ± 4.0%	5.9 ± 4.1%	8.6 ± 4.7%	6.0 ± 3.4%	-1.0 ± 1.3%	-2.2 ± 5.1%	-0.1 ± 1.7%	0.5 ± 2.3%	-1.9 ± 5.9%
Sit-to-stand												
	LCP18 vs LCP14						DSAP vs PFP					
	Maximum Principal Strain			Minimum Principal Strain			Maximum Principal Strain			Minimum Principal Strain		
ROIs	Healthy	Osteoporosis	Osteoporosis (weakened)	Healthy	Osteoporosis	Osteoporosis (weakened)	Healthy	Osteoporosis	Osteoporosis (weakened)	Healthy	Osteoporosis	Osteoporosis (weakened)
DSC1	3.0 ± 3.9%	9.5 ± 4.5%	7.9 ± 3.6%	-0.4 ± 0.9%	0.9 ± 1.7%	-0.3 ± 1.8%	6.6 ± 3.5%	9.2 ± 5.2%	7.3 ± 8.1%	0.6 ± 0.9%	1.0 ± 1.1%	0.2 ± 1.9%
DSC2	-14.6 ± 10.3%	-21.5 ± 2.1%	-24.9 ± 1.7%	-10.7 ± 4.1%	-15.9 ± 5.3%	-18.3 ± 6.2%	-4.4 ± 14.3%	-9.3 ± 5.9%	-17.9 ± 12.3%	-8.4 ± 4.9%	-11.3 ± 8.6%	-16.1 ± 3.6%
DSC3	-26.1 ± 7.1%	-37.9 ± 5.9%	-41.4 ± 8.1%	-18.1 ± 6.3%	-27.0 ± 2.9%	-29.8 ± 6.0%	-47.3 ± 7.9%	-52.3 ± 9.1%	-60.0 ± 8.1%	-36.8 ± 8.6%	-38.0 ± 7.1%	-43.1 ± 5.4%
DIST-FEMUR	-10.5 ± 0.9%	-15.8 ± 3.7%	-16.4 ± 3.6%	-13.4 ± 5.6%	-20.8 ± 5.4%	-21.7 ± 6.8%	-25.2 ± 9.0%	-25.3 ± 5.3%	-30.3 ± 7.0%	-25.6 ± 3.4%	-29.1 ± 4.6%	-32.1 ± 7.4%
Mean-CSC	42.0 ± 13.5%	54.3 ± 7.4%	57.2 ± 6.2%	8.7 ± 5.9%	15.6 ± 3.9%	16.4 ± 4.0%	19.6 ± 8.1%	18.1 ± 11.2%	23.7 ± 9.0%	-0.5 ± 3.5%	6.3 ± 7.3%	8.4 ± 7.4%

Table 5.1. Comparisons of percentage difference in maximum and minimum principal strains. Comparisons were made for LCP18 versus LCP14 and DSAP versus PFP, and between healthy and osteoporotic femurs (applying the normal and the weakened muscle forces, respectively) across three ADLs. Reduction in strains were indicated as negative numbers. Cells in green background, instances where DSAP showed greater strain reductions than LCP18 (most frequently in DSC3 and DIST-FEMUR). Cells in blue background, instances where DSAP showed decreased strains in the CSC ROI.

5.3.2 COMPARISONS OF PLATE STRESS BETWEEN HEALTHY AND OSTEOPOROTIC MODELS

Simulated loads of stair-descent consistently resulted in the highest magnitude of von Mises stress in the plate across three ADLs in models of each femur. Across different

specimens, the magnitude of von Mises stress in the plate was affected by both the state of bone health (healthy or osteoporosis) and by body weight of the specimen (the hip contact force and muscle forces were calculated as percentage body weight). Between one healthy femur and one osteoporotic femur with similar body weight (approximately 58 kg), the osteoporotic model clearly had higher von Mises stress in the plate (in both plating systems, Fig. 5.4B and D). The peak von Mises stresses (142.2 MPa and 347.4 MPa in the healthy and osteoporotic femurs, respectively) were below the fatigue strength of stainless steel (ranged 310 to 448 MPa at 10^7 cycles). Construct lengths showed little effect on the peak stress or stress distribution (data not shown). Weakened muscle forces reduced plate stress in osteoporotic models, with the peak stress reduced by 14.7% and 25.6% in DSAP and LCP18 models, respectively (Fig. 5.4B and D).

5.3.3 COMPARISONS OF LOAD TRANSFER AND LOCAL COMPRESSIVE STIFFNESS BETWEEN HEALTHY AND OSTEOPOROTIC MODELS

Across three simulated ADLs, a higher magnitude of compressive force was observed in the bone than the entire bone-implant system in cross-sections 3 through 11, which was balanced by the tension generated in the plate (Fig. 5.6A). In distal cross-sections 12 to 18, plates functioned to share the compressive force in the bone-implant system (Fig. 5.6A). Longer condyle-spanning constructs transferred the compressive force to the lateral condyle, therefore resulted in decreased compressive force in the distal metaphysis and diaphysis of implanted femurs as compared with femurs implanted with shorter constructs (cross-sections 15 through 18 in red boxes, Fig. 5.6B).

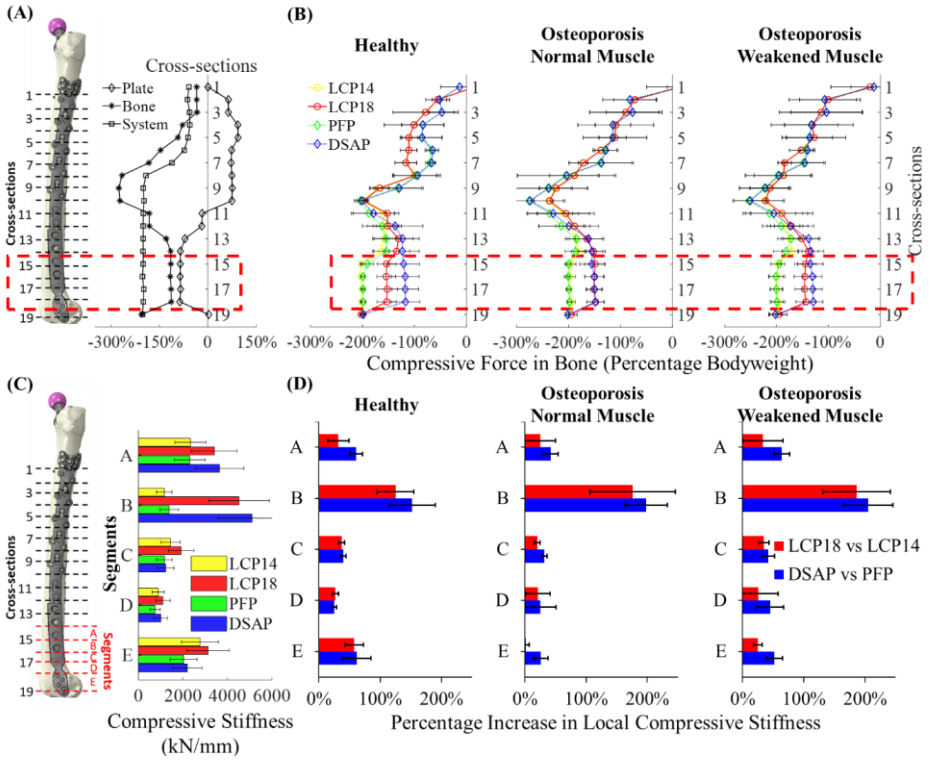

Fig. 5.6. Comparisons of load transfer and local compressive stiffness among two plating systems and two construct lengths in healthy and osteoporotic femurs. **(A)** Using a THA and DSAP-implanted femur model as an example, load transfer was shown for the plate, the bone and the bone-implant system under simulated loads of stair-descent. **(B)** Comparisons of load transfer in bone between models of healthy and osteoporotic femurs (applying 'the normal' and 'the weakened muscle forces', respectively) that were implanted with different plating systems and construct lengths under simulated loads of stair-descent. Red rectangle, distal cross-sections beyond the length of shorter diaphyseal plates. **(C)** Local compressive stiffness (in kN/mm) was compared across models of osteoporotic femurs (all plating configurations) under loads of stair-descent. **(D)** Percentage increases of local compressive stiffness (LCP18 versus LCP14 and DSAP versus PFP) were compared between healthy and osteoporotic femurs.

In healthy femurs, DSAP-implanted femurs consistently carried less compressive force in distal cross-sections than in LCP18-implanted femurs. Under loads of simulated stair-descent, 117.8 ± 26.8% bodyweight of compressive force was carried by DSAP-implanted femurs in cross-sections 15 through 18, while LCP18-implanted femurs carried 154.4 ± 18.0% bodyweight of compressive force (Fig. 5.6B). In osteoporotic models applying 'the normal muscle forces', a similar magnitude of compressive force was transferred through the distal femur in DSAP and LCP18-implanted models. Applying 'the weakened muscle forces', DSAP-implanted femurs carried 130.7% bodyweight of compressive force through the distal cross-sections, which was 14.1% less than the LCP18 (Fig. 5.6B).

Compared with the shorter constructs, implantation of the longer condyle-spanning constructs resulted in increased local compressive stiffness of the bone-implant system in distal metaphysis and diaphysis in both healthy and osteoporotic femurs (Fig. 5.6C and D). The greatest increase of local stiffness was consistently observed in segment B, the first segment below the most distal screw in shorter constructs (Fig. 5.6C and D). A reduction of local compressive stiffness (over 100%) was observed from segment A to B in models implanted with the shorter constructs (LCP14 and PFP, Fig. 5.6C). In contrast, models implanted with the condyle-spanning constructs (LCP18 and DSAP) showed an increase of local compressive stiffness (approximately 35%) from segment A to B (Fig. 5.6C).

Condyle-spanning constructs resulted in greater increases of local stiffness in osteoporotic femurs than in healthy femurs (Fig. 5.6C). Especially when applying 'the weakened muscle forces', LCP18 showed a mean increase of 61.3% of local stiffness in segments A through E in osteoporotic femurs as compared with 56.5% in healthy femurs.

Similarly, the DSAP models showed a mean increase of 82.1% of local stiffness in osteoporotic femurs compared with 61.9% in healthy femurs (Fig. 5.6C).

5.4 DISCUSSION

Applying ‘the normal muscle forces’, a higher magnitude of bone strains was observed in plate-implanted osteoporotic femurs than in healthy femurs (approximately 21.9% higher), while plates experienced higher stresses (up to 144.3% higher in peak von Mises stress). Compared with the shorter constructs (LCP14 and PFP), the longer condyle-spanning constructs (LCP18 and DSAP) reduced bone strains in both healthy and osteoporotic femurs in the distal metaphysis and diaphysis under loads of three simulated common ADLs. When forces in hip abductors and knee extensors were weakened in osteoporotic femurs, condyle-spanning constructs achieved greater strain reductions (approximately 5% more in DSC3 and DIST-FEMUR for both DSAP versus PFP and LCP18 versus LCP14) as compared with the osteoporotic models applying ‘the normal muscle forces’. The reduced strain via condyle-spanning constructs may be the combined effect of the reduced compressive force and increased local stiffness in the distal femur.

In the current study, FE models of healthy femurs predicted a peak maximum principal strain of approximately 1500 με and a peak minimum principal strain of around -2500 με under gait-loading, which were comparable to the literature reported values (Speirs et al., 2007a; Taylor et al., 1996). The osteoporotic models showed higher bone strains, which agreed with the clinically reported increased incidences of PFF or other femoral fractures in patients with osteoporosis (Karachalios et al., 2020; Sidler-Maier and Waddell, 2015).

Similar to the previously reported strain reductions in healthy femurs (Chen et al., 2022a), both condyle-spanning constructs reduced bone strains around the most distal screw of the shorter constructs and in the distal metaphysis in osteoporotic femurs, where secondary femoral refractures are typically reported (Lindahl et al., 2006; Randelli et al., 2018). Clinically, longer condyle-spanning constructs have been hypothesized to mitigate stress concentration in the distal femoral diaphysis (Bryant et al., 2009; Moloney et al., 2014). Through transferring load to the lateral condyle, longer condyle-spanning constructs carried up to 35% compressive force of the bone-implant system (the DSAP construct) in distal cross-sections, therefore lowering the resultant compressive force in the distal diaphysis and metaphysis of implanted femurs. Together with the increased local compressive stiffness (an 82.1% increase in DSAP implanted osteoporotic femurs) in the distal femur, strains in the DSC3 and DIST-FEMUR were thereby reduced.

Though the DSAP construct was shown to transfer more compressive load than LCP18 in distal cross-sections (beyond the lengths of shorter plates), DSAP minimally increased strains in the lateral condyle as compared with LCP18 implanted femurs (both the healthy and osteoporotic femurs). Especially under loads of gait and stair-descent, DSAP was shown to consistently reduce bone strains in the lateral condyle in osteoporotic femurs (especially when applying ‘the weakened muscles forces’) as compared with the PFP construct. Compared with the single condylar screw in the LCP18 construct, 4 condylar screws in DSAP enabled distribution of the force over a larger volume of bone, thereby mitigating the impact of concentrated load transfer.

The FE model predicted plate stress in healthy femurs was comparable to the magnitude reported by other investigators (the range of peak von Mises stress of between 200 to 300 MPa) (Leonidou et al., 2015; Pletka et al., 2011). Though the plate stress was higher in osteoporotic femurs, the magnitude was below the fatigue strength (450 MPa at 2 × 106 cycles, corresponding to approximately five years of normal walking) (ASTM F138-13a, 2013).

Simulations of osteoporosis-related weakening of hip abductors and knee extensors allowed evaluations of the impact of varied muscle loading on the mechanics of plate-implanted osteoporotic femurs. By reducing the major hip abductors and knee extensors to 70% of their healthy capacities in osteoporotic models (Sinaki et al., 2005), the peak plate stress and mean bone strains in ROIs were lowered. Applying 'the weakened muscle forces', condyle-spanning constructs reduced the amount of compressive force in the distal femur and resulted in greater increases in local compressive stiffness as compared with the osteoporotic models applying 'the normal muscle forces'. The combined effect of reduced compressive force and increased local compressive stiffness may be associated with the greater strain reductions in models with weakened muscles.

Several limitations regarding the methodology used in the current study need to be noted. Given the experimentally observed lack of relative displacement, fully-bonded contact was modeled at bone-screw and bone-stem interfaces (Chen et al., 2022a). Though the fully-bonded bone-screw interface effectively simulated the lack of motion between bone and screws during mechanical testing, future investigations will consider the effect of contact definition on the interfacial micromotion and load transfer between bone and screws.

Similarly, considering sliding contact between bone and stem could enable the simulation of an unstable stem as in the Vancouver type B2 fractures (Abdel et al., 2016; Duncan and Haddad, 2014). Future studies should consider both the experimental and the computational means to simulate and validate FE models of the unstable THA stem. This study simulated the combined weakening of hip abductors and knee extensors in osteoporotic femurs by reducing the forces in glutei and vastus muscles, which did not account for changes in kinematics that are associated with Trendelenburg gait. The re-adjustment of hip contact force and forces of other major muscles partially accounted for the changes in resultant force and moment in osteoporotic femurs as the result of the weakening of hip abductors and knee extensors. However, future studies should account for kinematics changes to better simulate the physiological loading environment in plate-implanted osteoporotic femurs.

5.5 CONCLUSION

The results of the current study showed the mechanical efficacy of using longer condyle-spanning plates in osteoporotic femurs to mitigate elevated strains in the distal femur when using shorter constructs. Between the two condyle-spanning constructs, the DSAP construct achieved higher percentages of strain reduction as compared with LCP18, while condylar fixation using multiple screws in DSAP avoided the potential bone strain concentration in the lateral condyle caused by the more distally transferred compressive forces. The combined experimental and computational methodology can be developed as the basis for a preclinical assessment of the fixation mechanics of femoral implants.

CHAPTER SIX. SUMMARY AND FUTURE DIRECTIONS

6.1 A BRIEF SUMMARY OF CURRENT UNDERSTANDINGS

The coupled musculoskeletal and FE model has been proved to be useful and effective tools for the simulation of the physiological strain state of the bone and the stress of the plate under loads of common ADLs (Chen et al., 2022b, 2022a, 2021). Coupled musculoskeletal and FE models were utilized throughout the studies of this thesis, while the results of those models were able to shed light on the mechanisms of the pathogenesis of PFFs and the risks of complications after the plate-screw fixation for a Vancouver type B1 PFF (Chen et al., 2022b, 2022a, 2021). The coupled models were also successfully utilized to evaluate and compare the fixation mechanics of different plating systems and different construct lengths in both healthy and osteoporotic femurs (Chen et al., 2022a). Through simulating physiological loads of three common ADLs, the condyle-spanning constructs of two plating systems were both able to reduce bone strains around the most distal diaphyseal screw and in the distal metaphysis as compared with their corresponding shorter diaphyseal constructs (Chen et al., 2022a). The model estimated strain reduction agreed with the clinically reported mitigated risks of femoral refractures distal to the shorter diaphyseal plate via condyle-spanning construct (Bryant et al., 2009; Moloney et al., 2014). Strain reduction was associated with the combined effect of decreased resultant force in

the bone and the increased local stiffness of the bone-implant system (Chen et al., 2022a). The coupled musculoskeletal and FE model was an efficient tool for the simulation of physiological ADL loads, however, it is inherently difficult to be validated due to the difficulty in recreating the complex muscle loads experimentally. As described previously, mechanical tests applying simplified loads were typically utilized in previous studies to assess the mechanics of THA and/or plate implanted femurs (Choi et al., 2010; Lenz et al., 2016b, 2016a; Lever et al., 2010; Moazen et al., 2014, 2013). Due to different study objectives, there is a lack of consensus on how the THA and/or plate-implanted femurs should be tested (Moazen et al., 2014; Wang et al., 2019). Nonetheless, evidence is lacking to show that the mechanical tests used in previous studies may accurately represent the physiological stress/strain state of the bone and/or the implant.

In this dissertation, based on the simulated femoral strains and plate stress under physiological muscle loads, several new mechanical tests were developed that were able to match the simulated strain/stress state of the bone-implant system under ADL-loading (Chen et al., 2022b, 2021). Those new mechanical tests were developed using an FE integrated optimization approach that uses the stress/strain state of the bone or the plate as the optimization objective (Chen et al., 2022b, 2021). The optimization approach was able to identify the key testing parameters that were essential for matching the strain/stress of the bone and/or the implant. Meanwhile, the fidelity of those simplified tests was demonstrated by achieving good agreement with the bone remodeling stimuli as compared with ADL-loading models and other clinical and modeling studies (Chapter Two), as well as by matching the stress state of the plate in ADL-loading models (Chapter Three). The

newly-developed axial compression test was further used in studies of this thesis (Chapters Four and Five) for the validation of THA and plate-implanted femur models (Chen et al., 2022a), where models of both the healthy and the osteoporotic femurs were shown to achieve good agreement with the experimentally measured bone and/or implant displacement. This newly-developed combined modeling and testing framework could be used as a pre-clinical platform for future evaluation and development of orthopedic fixation devices or implants.

6.2 CURRENT LIMITATIONS AND FUTURE DIRECTIONS

Throughout the studies in this thesis, several limitations have constrained the scope of this thesis, especially the limitations in the methodologies used in those studies. Such limitations include the contact definition of the bone-stem and the bone-screw interfaces, and the validation of FE models using the displacement of the femur and the plate. Meanwhile, studies in different chapters of this thesis have modeled both the healthy and the osteoporotic femurs, as well as different types of THA stems. However, previous chapters have not evaluated the risks of PFFs in osteoporotic femurs, nor did previous chapters compare the differences in mechanics between two different THA stems. Hence, the following sections will provide additional information on how the limitations may affect the scope of this thesis. Directions for future investigations were also proposed to address clinical and scientific questions regarding the mechanics of PFF fixation.

6.2.1 ANALYSES OF RISKS OF PFF IN OSTEOPOROTIC FEMURS

Studies in this thesis utilized the coupled musculoskeletal and FE model to estimate the strain state in implanted femurs under simulated loads of common ADLs. Chapter two has shown that the coupled musculoskeletal and FE model applying appropriately distributed muscle forces were able to agree with the radiographically measured and previous modeling study predicted bone remodeling stimuli (Fig. 2.2 in Chapter Two). Meanwhile, loads of common ADLs, especially the more demanding stair-descent may result in higher than fatigue level strains in bone elements adjacent to the tip of the implanted THA stem (Fig. 2.3 in Chapter Two).

Across the studies in this thesis, two different THA femoral components were modeled. The SUMMIT stem was modeled in studies described in Chapters Two and Three, while the CORAIL stem was used in Chapters Four and Five (Fig. 6.1A). Additionally, Chapter Five investigated the impact of bone health on the fixation mechanics of the plate-screw construct and showed that models of osteoporotic femurs resulted in a higher magnitude of strains as compared with healthy femurs (Fig. 5.4 and 5.5 in Chapter 5). However, given the scope of studies described in previous chapters, risks of PFFs were not evaluated in osteoporotic femurs.

According to previously described results and new additional simulations, risks of PFFs may be affected by different THA femoral components and the state of bone health (Fig. 6.1). Under simulated loads of stair-descent, the healthy femur hardly had bone elements exceeding the fatigue threshold of 2500 με, different femoral component clearly resulted in different distributions of maximum principal strain in the proximal and the middle

femoral shaft (Fig. 6.1A). The CORAIL stem resulted in a concentrated strain more proximally than the SUMMIT stem, which showed a higher maximum principal strain toward the middle of the femoral shaft (adjacent to the tip of the stem, Fig. 6.1A).

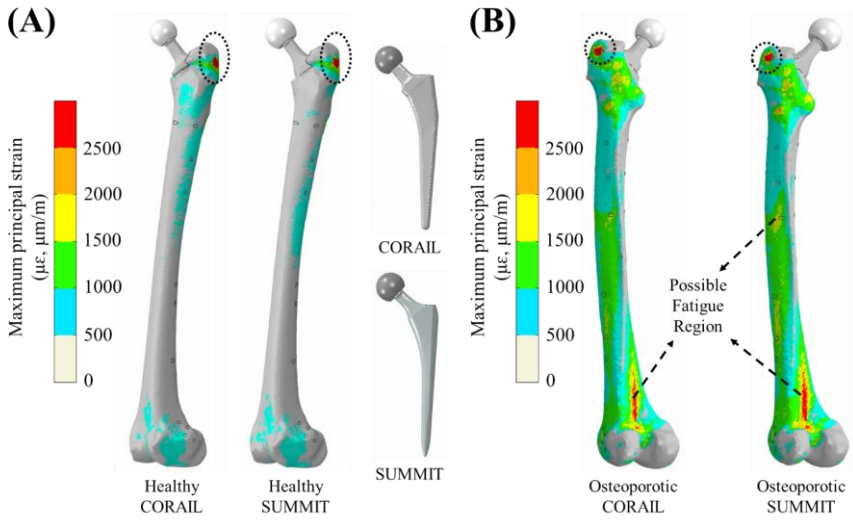

Fig. 6.1. Comparisons of maximum principal strain between a healthy femur and an osteoporotic femur that were implanted with two different THA femoral components (CORAIL and SUMMIT) under simulated loads of stair-descent. **(A)** Maximum principal strain of a healthy femur that were implanted with two different THA femoral components. **(B)** Maximum principal strain of an osteoporotic femur that were implanted with two different THA femoral components. Note that possible fatigue regions were identified as concentrated bone elements that showed beyond fatigue level maximum principal strain (> 2500 με). Regions in dashed ellipsoids were the location where the force of gluteus medius was applied. Due to the high magnitude of gluteus medius force (>120% bodyweight), regions in ellipsoids showed concentrated high maximum principal strain.

Models of CORAIL and SUMMIT implanted osteoporotic femur clearly showed higher maximum principal strain compared with the healthy femur (Fig. 6.1B). Models of the osteoporotic femur (in both CORAIL and SUMMIT implanted models) clearly showed a fatigue region (concentrated bone elements showing beyond 2500 με maximum principal strain) in the posterior aspect of the distal femoral shaft, which is indicative of fatigue/stress fracture at the location (Fig. 6.1B). The SUMMIT-implanted osteoporotic femur also showed a higher maximum principal strain in the middle femoral shaft compared with the CORAIL-implanted osteoporotic femur, the location is adjacent to the underlying tip of the stem (Fig. 6.1B).

The concentrated maximum principal strain in the posterior aspect of the distal femoral shaft was indicative of the risk of a Vancouver type C fracture (Fig. 1.1). Both the CORAIL and the SUMMIT stems were shown to result in the concentrated strain in the distal shaft of the osteoporotic femur, while the healthy femur did not show elevated strain in the same region (Fig. 6.1). As previously described in Chapter Two, the concentration of maximum principal strain in the middle femoral shaft may indicate an increased risk of the Vancouver type B PFF (Fig. 1.1). Both the SUMMIT-implanted healthy and osteoporotic femurs showed an elevated strain in the middle femoral shaft as compared with the CORAIL models, which may indicate elevated risks of the Vancouver type B PFF (Fig. 6.1).

The state of bone health and different types of THA stems may affect the risks and the types of Vancouver PFFs. Future studies may investigate more types of THA stem while evaluating the state of bone health to further the understanding of the mechanical pathogenesis of different Vancouver PFFs.

6.2.2 EFFECT OF CONTACT MODELING OF BONE-STEM INTERFACE ON PERIPROSTHETIC FEMORAL STRAINS

The studies throughout this thesis modeled both the bone-stem and the bone-screw interfaces as fully-bonded. Thereby, FE models in those studies were only able to simulate a well-fixed THA stem and the Vancouver type B1 PFF. However, the more prevalent Vancouver type B2 PFF requires the simulation of a loosened THA stem. Studies in this thesis could not investigate the mechanical mechanism underlying the pathogenesis of a type B2 PFF, nor the fixation mechanics with a loosened THA stem. Meanwhile, other investigators have shown that the fully-bonded bone-screw interface may over-estimate bone strains around the screws in the near cortex, while under-estimating bone strains in the far cortex. However, due to the lack of information in both modeling data and experimental measurements of bone strains around fixation screws, a consensus is lacking on how to appropriately represent the bone-screw interface.

Across studies in this thesis, the bone-stem interface and the bone-screw interface have been modeled as fully-bonded. Experimental tests in this thesis have shown a lack of relative motion of the THA stem, as well as the plate against the implanted femur, thereby the fully-bonded interfaces were deemed appropriate for current investigations. However, without a sliding-contact definition, the studies in this thesis were not able to simulate or investigate how a loosened stem may affect the risks of PFFs, nor the mechanics of the Vancouver type B2 and B3 PFFs, especially that type B2 PFF was the most prevalent PFF in all PFF cases (Abdel et al., 2016).

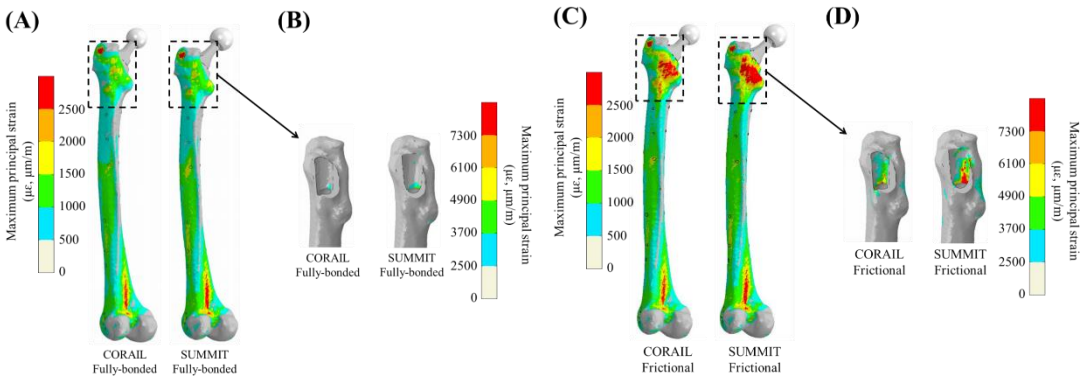

Fig. 6.2. Comparisons of maximum principal strain in a THA-implanted osteoporotic femur among two THA femoral components and two different contact definitions at the bone-stem interface. **(A)** Comparisons of maximum principal strain in a THA implanted osteoporotic femur between two THA components using fully-bonded bone-stem interface. **(B)** Comparisons of maximum principal strain at the fully-bonded bone-stem interface. **(C)** Comparisons of maximum principal strain in a THA-implanted osteoporotic femur between two THA components using sliding-contact bone-stem interface. **(D)** Comparisons of maximum principal strain at the sliding-contact bone-stem interface. Note that (B) and (D) used a larger-scaled strain legend to show bone elements that had maximum principal strain higher than the 2500 με fatigue threshold, while bone elements higher than the 7300 με yield threshold were shown in red.

As a preliminary investigation into the effect of contact definition on periprosthetic femoral strains, the sliding-contact was simulated for the bone-stem interface and compared with the fully-bonded interface. Using a THA-implanted osteoporotic femur as an example, a frictional contact (with a friction coefficient of 0.7) was modeled for the bone-stem interface. The modeled femur was one of the osteoporotic specimens in Chapter

Two, which had a DXA T-score of -2.6. Though the femur was implanted with the CORAIL stem previously, a SUMMIT stem was also implanted into the femur to compare the periprosthetic strain. The location of the femoral head was maintained the same in the SUMMIT-implanted model as in the CORAIL-implanted model. The orientation of the SUMMIT stem mimicked the CORAIL stems by maintaining the position of the taper.

Under simulated loads of stair-descent, models with frictional bone-stem interface showed a higher periprosthetic strain in the proximal femur than models with fully-bonded bone-stem interface (Fig. 6.2). Few bone elements exceeded the fatigue threshold of 2500 με of maximum principal strain at the fully-bonded bone-stem interface (Fig. 6.2B). In contrast, the frictional contact models clearly showed much more bone elements at the bone-stem interface beyond the fatigue threshold in maximum principal strain (Fig. 6.2D). Compared with the CORAIL-implanted frictional contact models, the SUMMIT-implanted models showed more bone elements exceeding the fatigue threshold at the bone-stem (Fig. 6.2D) interface, as well as in the proximal femur (Fig. 6.2C). In addition, some periprosthetic elements in the SUMMIT-implanted model had a maximum principal strain even higher than the yield threshold of 7300 με (Fig. 6.2D).

The concentrated bone elements exceeding the fatigue threshold at the bone-stem interface are indicative of elevated risks of fatigue/stress fractures at the location (Morgan et al., 2018). Especially in osteoporotic femurs, the results may indicate elevated risks of type A fractures (Fig. 1.1 in Chapter One). The frictional contact was shown to mainly affect the magnitude and distribution of maximum principal strain in bony elements surrounding the implanted stem (Fig. 6.2). The frictional contact did not affect the

concentrated maximum principal strain in the posterior aspect of the distal femur (Fig. 6.2) as described in the previous section (Section 6.2.1).

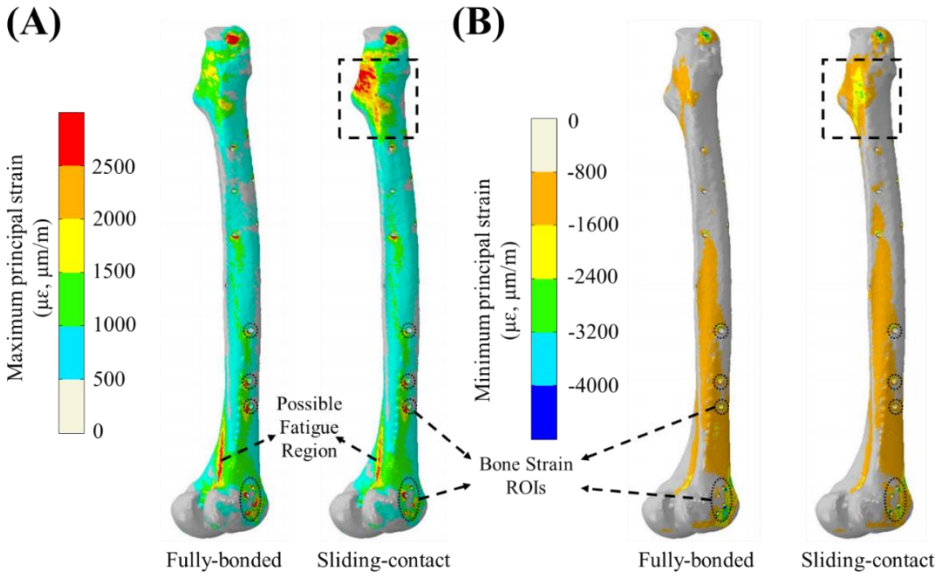

Fig. 6.3. Comparisons of maximum principal strain **(A)** and minimum principal strain **(B)** between two different bone-stem contact definitions in a THA (the CORAIL stem) and DSAP implanted osteoporotic femur. Regions in dashed rectangles indicated regions in the proximal femur that experienced concentrated high strains in the frictional-contact model. Regions in dashed ellipsoids were locations of bone strain ROIs that were used in previous chapters for the comparison of bone strains between different plating systems and construct lengths.

When the bone-stem frictional contact was modeled in a THA and plate-implanted osteoporotic model, the frictional contact was shown to mainly result in elevated maximum and minimum principal strains in the proximal femur in bone elements adjacent to the implanted stem (Fig. 6.3). Similar to the THA-implanted osteoporotic model (Fig. 6.1 and

6.2), the bone-stem frictional contact did not affect the possible fatigue region in the distal femur (Fig. 6.3). In addition, the bone-stem friction contact showed little effect on the magnitude of maximum (Fig. 6.3A) and minimum principal strains (Fig. 6.3A) in the bone strain ROIs around the distal fixation screws.

Given the number of bone elements experiencing fatigue level periprosthetic strains, future studies should consider modeling the plastic deformation of bone elements in periprosthetic bone, especially in osteoporotic femurs. By considering the plastic behavior of bone elements, future studies would be able to simulate the behavior of a loosened stem to investigate the mechanics of Vancouver type B2 and B3 PFFs. Similarly, future studies should evaluate the effect of contact definition at the bone-screw interface, thereby further investigating the mechanisms of screw loosening.

6.2.3 FUTURE DIRECTIONS FOR MODEL VALIDATION

The results of this thesis showed that validation of THA and plate-implanted femur FE models using the displacement profile of bone and the plate were able to distinguish the mechanical behavior of different specimens and different implanted conditions. Especially specimen-specific models were shown to be able to distinguish different femur geometries and material distribution in the bone. Good agreement in displacement between model predictions and experimental measurements was associated with the accurate replication of the *in situ* implanted positions of the THA stem and the plate, as well as the appropriately modeled material distribution in the femur.

Studies in this thesis used digitized geometries as references (obtained either using an optical motion capture system as described in Chapters Two and Three, or a 3D scanner as in Chapters Four and Five), and applied a point-cloud-based algorithm in matlab, models of the THA and plate implanted femurs were able to accurately match the *in situ* implanted positions of the THA stem and the plate. Especially, geometries obtained from the 3D scanner were shown to achieve a closer match with the geometries in FE models. In addition, all the specimens used in this thesis were CT scanned with a density phantom, which enabled the calculation of specimen-specific Hounsfield unit to bone mineral density conversion for each femur model. This specimen-specific conversion was shown to well represent the nonhomogeneous distribution of Young's moduli in each tested and modeled cadaveric femur, thereby achieving good agreement in displacement profiles.

The displacement profiles of the bone and the plate were measurements that characterized the deformation of the entire bone-implant system. By matching the deformation behavior of the entire bone-implant system, FE models showed a high gradient of bone strains in small surface regions around the implanted fixation screws. Due to the large field of view that was required to measure the displacement of the entire anterolateral surface of the femur and the full length of the plate, experimental tests in this thesis could not capture changes in surface strains in small surface areas around fixation screws. In addition, screws were physically covered by the plate once implanted in the femur, it was difficult to establish good views of the bone surface around screws using the DIC system.

To enable the direct experimental validation of bone strains, future studies should consider either performing DIC measurements in a smaller field of view to record surface

strain in the high gradient region around the screws, or utilizing other testing devices, such as surface strain gauges to measure bone strains around the screws. The direct measurement of bone strains around fixation screws could provide more detailed information on the strains in those high gradient regions, thereby better facilitating the investigation into contact definition at the bone-screw interface as described in section 6.2.2.

Future studies may also consider using cyclic loads to measure the relative displacement between bone and plate, as well as between bone and screws over time. Screw loosening has been reported to initiate due to fatigue level strains and micro-damages to the bone while progressing over a long period of cyclic loading as a result of repetitive common daily activities (Feng et al., 2019; Sugiura et al., 2000). Therefore, the measurement of bone-screw and bone-plate displacement over time may provide information not only on the level of interfacial strains that may initiate bone damage, but also on the elastic-plastic behavior, and even the viscoelasticity of the bone-screw interface. Those measurements can be used to further improve the strategies in contact modeling and material modeling of the femur-THA-plate system.

BIBLIOGRAPHY

Abdel, M.P., Watts, C.D., Houdek, M.T., Lewallen, D.G., Berry, D.J., 2016. Epidemiology of periprosthetic fracture of the femur in 32 644 primary total hip arthroplasties: A 40-year experience. Bone Jt. J. 98B, 461–467. https://doi.org/10.1302/0301-620X.98B4.37201

ASTM F138-13a, 2013. Standard Specification for Wrought 18Chromium-14Nickel-2.5Molybdenum Stainless Steel Bar and Wire for Surgical Implants (UNS S31673). ASTM Int. 1–6. https://doi.org/10.1520/F0138-19.2

ASTM International, 2008. Standart Specification and Test Method for Metallic Bone Plates F382-99 1–12. https://doi.org/10.1520/F0382-17.Copyright

Avval, P.T., Samiezadeh, S., Bougherara, H., 2016. Long-term response of femoral density to hip implant and bone fracture plate: Computational study using a mechano-biochemical model. Med. Eng. Phys. 38, 171–180. https://doi.org/10.1016/j.medengphy.2015.11.013

Be'ery-Lipperman, M., Gefen, A., 2005. Contribution of muscular weakness to osteoporosis: Computational and animal models. Clin. Biomech. 20, 984–997. https://doi.org/10.1016/j.clinbiomech.2005.05.018

Boesmueller, S., Baumbach, S.F., Hofbauer, M., Wozasek, G.E., 2015. Plate failure following plate osteosynthesis in periprosthetic femoral fractures. Wien. Klin. Wochenschr. 127, 770–778. https://doi.org/10.1007/s00508-015-0818-3

Brech, G.C., Alonso, A.C., Luna, N.M.S., Greve, J.M., 2013. Correlation of postural balance and knee muscle strength in the sit-to-stand test among women with and without postmenopausal osteoporosis. Osteoporos. Int. 24, 2007–2013. https://doi.org/10.1007/s00198-013-2285-x

Bryant, G.K., Morshed, S., Agel, J., Henley, M.B., Barei, D.P., Taitsman, L.A., Nork, S.E., 2009. Isolated locked compression plating for Vancouver Type B1 periprosthetic femoral fractures. Injury 40, 1180–1186. https://doi.org/10.1016/j.injury.2009.02.017

Chan, S.M.T., Neu, C.P., Komvopoulos, K., Reddi, A.H., Di Cesare, P.E., 2011. Friction and wear of hemiarthroplasty biomaterials in reciprocating sliding contact with articular cartilage. J. Tribol. 133, 1–7. https://doi.org/10.1115/1.400476

Chantarapanich, N., Sitthiseripratip, K., Mahaisavariya, B., Siribodhi, P., 2016. Biomechanical performance of retrograde nail for supracondylar fractures stabilization. Med. Biol. Eng. Comput. 54, 939–952. https://doi.org/10.1007/s11517-016-1466-0

Chen, X., Andreassen, T.E., Myers, C.A., Clary, C.W., Coombs, D., DeWall, R.J., Fritz, B., Bracey, D.N., Hedge, V., Rullkoetter, P.J., 2022a. Impact of periprosthetic femoral fracture fixation plating constructs on local stiffness, load transfer, and bone strains. J. Mech. Behav. Biomed. Mater. 125, 104960. https://doi.org/10.1016/j.jmbbm.2021.104960

Chen, X., Myers, C.A., Clary, C.W., Dewall, R.J., Fritz, B., Blauth, M., Rullkoetter, P.J., 2022b. Simplified Mechanical Tests Can Simulate Physiological Mechanics of a Fixation Construct for Periprosthetic Femoral Fractures. J. Biomech. Eng. 144, 1–9. https://doi.org/10.1115/1.4052372

Chen, X., Myers, C.A., Clary, C.W., DeWall, R.J., Fritz, B., Blauth, M., Rullkoetter, P.J., 2021. Development of axial compression and combined axial compression and torque loading configurations to reproduce strain in the implanted femur during activities of daily living. J. Biomech. 120, 110363. https://doi.org/10.1016/j.jbiomech.2021.110363

Choi, J.K., Gardner, T.R., Yoon, E., Morrison, T.A., Macaulay, W.B., Geller, J.A., 2010. The effect of fixation technique on the stiffness of comminuted vancouver B1 periprosthetic femur fractures. J. Arthroplasty 25, 124–128. https://doi.org/10.1016/j.arth.2010.04.009

Corten, K., Vanrykel, F., Bellemans, J., Reynders Frederix, P., Simon, J.P., Broos, P.L.O., 2009. An algorithm for the surgical treatment of periprosthetic fractures of the femur around a well-fixed femoral component. J. Bone Jt. Surg. - Ser. B 91, 1424–1430. https://doi.org/10.1302/0301-620X.91B11.22292

Dhason, R., Roy, S., Datta, S., 2020. A biomechanical study on the laminate stacking sequence in composite bone plates for vancouver femur B1 fracture fixation. Comput. Methods Programs Biomed. 196, 105680. https://doi.org/10.1016/j.cmpb.2020.105680

Doube, M., Kłosowski, M.M., Arganda-carreras, I., Fabrice, P., 2010. UKPMC Funders Group BoneJ : free and extensible bone image analysis in ImageJ. Bone 47, 1076–1079. https://doi.org/10.1016/j.bone.2010.08.023.BoneJ

Duda, G.N., Heller, M., Albinger, J., Schulz, O., Schneider, E., Claes, L., 1998. Influence of muscle forces on femoral strain distribution. J. Biomech. 31, 841–846. https://doi.org/10.1016/S0021-9290(98)00080-3

Duncan, C.P., Haddad, F.S., 2014. The Unified Classification System (UCS): Improving our understanding of periprosthetic fractures. Bone Jt. J. 96 B, 713–716. https://doi.org/10.1302/0301-620X.96B6.34040

Ebrahimi, H., Rabinovich, M., Vuleta, V., Zalcman, D., Shah, S., Dubov, A., Roy, K., Siddiqui, F.S., Schemitsch, E.H., Bougherara, H., Zdero, R., 2012. Biomechanical properties of an intact, injured, repaired, and healed femur: An experimental and computational study. J. Mech. Behav. Biomed. Mater. 16, 121–135. https://doi.org/10.1016/j.jmbbm.2012.09.005

Feng, X., Lin, G., Fang, C.X., Lu, W.W., Chen, B., Leung, F.K.L., 2019. Bone resorption triggered by high radial stress: The mechanism of screw loosening in plate fixation of long bone fractures. J. Orthop. Res. 37, 1498–1507. https://doi.org/10.1002/jor.24286

Franklin, J., Malchau, H., 2007. Risk factors for periprosthetic femoral fracture. Injury 38, 655–660. https://doi.org/10.1016/j.injury.2007.02.049

Giovanni, V., Davide, B., Giuseppe, S., Massimiliano, C., Alberto, B., Antonio, D.A., Oronzo, D.C., Biagio, M., 2020a. Periprosthetic femoral re-fractures pathogenesis, classification, and surgical implications. Injury 1–7. https://doi.org/10.1016/j.injury.2020.11.030

Giovanni, V., Davide, B., Giuseppe, S., Massimiliano, C., Alberto, B., Antonio, D.A., Oronzo, D.C., Biagio, M., 2020b. Periprosthetic femoral re-fractures pathogenesis, classification, and surgical implications. Injury 1–7. https://doi.org/10.1016/j.injury.2020.11.030

Glowacki, J., Hurwitz, S., Thornhill, T.S., Kelly, M., Leboff, M.S., 2003. Osteoporosis and Vitamin-D Deficiency among Postmenopausal Women with Osteoarthritis Undergoing Total Hip Arthroplasty. J. Bone Jt. Surg. - Ser. A 85, 2371–2377. https://doi.org/10.2106/00004623-200312000-00015

Henriksen, M., Aaboe, J., Simonsen, E.B., Alkjær, T., Bliddal, H., 2009. Experimentally reduced hip abductor function during walking: Implications for knee joint loads. J. Biomech. 42, 1236–1240. https://doi.org/10.1016/j.jbiomech.2009.03.021

Jitprapaikulsarn, S., Chantarapanich, N., Gromprasit, A., Mahaisavariya, C., Patamamongkonchai, C., 2021. Single lag screw and reverse distal femur locking compression plate for concurrent cervicotrochanteric and shaft fractures of the femur: biomechanical study validated with a clinical series. Eur. J. Orthop. Surg. Traumatol. https://doi.org/10.1007/s00590-020-02868-z

Karachalios, T.S., Koutalos, A.A., Komnos, G.A., 2020. Total hip arthroplasty in patients with osteoporosis. HIP Int. 30, 370–379. https://doi.org/10.1177/1120700019883244

Kersh, M.E., Martelli, S., Zebaze, R., Seeman, E., Pandy, M.G., 2018. Mechanical Loading of the Femoral Neck in Human Locomotion. J. Bone Miner. Res. 33, 1999–2006. https://doi.org/10.1002/jbmr.3529

Khoo, B.C.C., Brown, K., Cann, C., Zhu, K., Henzell, S., Low, V., Gustafsson, S., Price, R.I., Prince, R.L., 2009. Comparison of QCT-derived and DXA-derived areal bone mineral density and T scores. Osteoporos. Int. 20, 1539–1545. https://doi.org/10.1007/s00198-008-0820-y

Labuda, A., Papaioannou, A., Pritchard, J., Kennedy, C., DeBeer, J., Adachi, J.D., 2008. Prevalence of Osteoporosis in Osteoarthritic Patients Undergoing Total Hip or Total Knee Arthroplasty. Arch. Phys. Med. Rehabil. 89, 2373–2374. https://doi.org/10.1016/j.apmr.2008.06.007

Laurer, H.L., Wutzler, S., Possner, S., Geiger, E. V., El Saman, A., Marzi, I., Frank, J., 2011. Outcome after operative treatment of Vancouver type B1 and C periprosthetic femoral fractures: Open reduction and internal fixation versus revision arthroplasty. Arch. Orthop. Trauma Surg. 131, 983–989. https://doi.org/10.1007/s00402-011-1272-y

Lenz, M., Stoffel, K., Gueorguiev, B., Klos, K., Kielstein, H., Hofmann, G.O., 2016a. Enhancing fixation strength in periprosthetic femur fractures by orthogonal plating - A biomechanical study. J. Orthop. Res. 34, 591–596. https://doi.org/10.1002/jor.23065

Lenz, M., Stoffel, K., Kielstein, H., Mayo, K., Hofmann, G.O., Gueorguiev, B., 2016b. Plate fixation in periprosthetic femur fractures Vancouver type B1—Trochanteric hook plate or subtrochanterical bicortical locking? Injury 47, 2800–2804. https://doi.org/10.1016/j.injury.2016.09.037

Leonidou, A., Moazen, M., Lepetsos, P., Graham, S.M., Macheras, G.A., Tsiridis, E., 2015. The biomechanical effect of bone quality and fracture topography on locking plate fixation in periprosthetic femoral fractures. Injury 46, 213–217. https://doi.org/10.1016/j.injury.2014.10.060

Lever, J.P., Zdero, R., Nousiainen, M.T., Waddell, J.P., Schemitsch, E.H., 2010. The biomechanical analysis of three plating fixation systems for periprosthetic femoral fracture near the tip of a total hip arthroplasty. J. Orthop. Surg. Res. 5, 1–8. https://doi.org/10.1186/1749-799X-5-45

Lindahl, H., Malchau, H., Odén, A., Garellick, G., 2006. Risk factors for failure after treatment of a periprosthetic fracture of the femur. J. Bone Jt. Surg. - Ser. B 88, 26–30. https://doi.org/10.1302/0301-620X.88B1.17029

Lindahl, H., Oden, A., Garellick, G., Malchau, H., 2007. The excess mortality due to periprosthetic femur fracture. A study from the Swedish national hip arthroplasty register. Bone 40, 1294–1298. https://doi.org/10.1016/j.bone.2007.01.003

Mäkinen, T.J., Alm, J.J., Laine, H., Svedström, E., Aro, H.T., 2007. The incidence of osteopenia and osteoporosis in women with hip osteoarthritis scheduled for cementless total joint replacement. Bone 40, 1041–1047. https://doi.org/10.1016/j.bone.2006.11.013

Marsland, D., Mears, S.C., 2012. A Review of Periprosthetic Femoral Fractures Associated With Total Hip Arthroplasty. Geriatr. Orthop. Surg. Rehabil. 3, 107–120. https://doi.org/10.1177/2151458512462870

Miettinen, S.S.A., Törmä, S. V., Lappalainen, J.M., Sund, R., Kröger, H., 2021. Retrospective Population-Based Cohort Study of Incidence, Complications, and Survival of 202 Operatively Treated Periprosthetic Femoral Fractures. J. Arthroplasty 36, 2591–2596. https://doi.org/10.1016/j.arth.2021.02.060

Min, B.-W., Lee, K.-J., Cho, C.-H., Lee, I.-G., Kim, B.-S., 2020. High Failure Rates of Locking Compression Plate Osteosynthesis with Transverse Fracture around a Well-Fixed Stem Tip for Periprosthetic Femoral Fracture. J. Clin. Med. 9, 3758. https://doi.org/10.3390/jcm9113758

Moazen, M., Jones, A.C., Jin, Z., Wilcox, R.K., Tsiridis, E., 2011. Periprosthetic fracture fixation of the femur following total hip arthroplasty: A review of biomechanical testing. Clin. Biomech. 26, 13–22. https://doi.org/10.1016/j.clinbiomech.2010.09.002

Moazen, M., Leonidou, A., Pagkalos, J., Marghoub, A., Fagan, M.J., Tsiridis, E., 2016. Application of Far Cortical Locking Technology in Periprosthetic Femoral Fracture Fixation: A Biomechanical Study. J. Arthroplasty 31, 1849–1856. https://doi.org/10.1016/j.arth.2016.02.013

Moazen, M., Mak, J.H., Etchels, L.W., Jin, Z., Wilcox, R.K., Jones, A.C., Tsiridis, E., 2014. Periprosthetic femoral fracture - a biomechanical comparison between vancouver type B1 and B2 fixation methods. J. Arthroplasty 29, 495–500. https://doi.org/10.1016/j.arth.2013.08.010

Moazen, M., Mak, J.H., Etchels, L.W., Jin, Z., Wilcox, R.K., Jones, A.C., Tsiridis, E., 2013. The effect of fracture stability on the performance of locking plate fixation in periprosthetic femoral fractures. J. Arthroplasty 28, 1589–1595. https://doi.org/10.1016/j.arth.2013.03.022

Moloney, G.B., Westrick, E.R., Siska, P.A., Tarkin, I.S., 2014. Treatment of periprosthetic femur fractures around a well-fixed hip arthroplasty implant: Span the whole bone. Arch. Orthop. Trauma Surg. 134, 9–14. https://doi.org/10.1007/s00402-013-1883-6

Morgan, E.F., Bayraktar, H.H., Keaveny, T.M., 2003. Trabecular bone modulus-density relationships depend on anatomic site. J. Biomech. 36, 897–904. https://doi.org/10.1016/S0021-9290(03)00071-X

Morgan, E.F., Unnikrisnan, G.U., Hussein, A.I., 2018. Annual Review of Biomedical Engineering Bone Mechanical Properties in Healthy and Diseased States. https://doi.org/10.1146/annurev-bioeng-062117

Mündermann, A., Asay, J.L., Mündermann, L., Andriacchi, T.P., 2008. Implications of increased medio-lateral trunk sway for ambulatory mechanics. J. Biomech. 41, 165–170. https://doi.org/10.1016/j.jbiomech.2007.07.001

Myers, C.A., Laz, P.J., Shelburne, K.B., Judd, D.L., Huff, D.N., Winters, J.D., Stevens-Lapsley, J.E., Rullkoetter, P.J., 2018. The impact of hip implant alignment on muscle and joint loading during dynamic activities. Clin. Biomech. 53, 93–100. https://doi.org/10.1016/j.clinbiomech.2018.02.010

Ottesen, T.D., McLynn, R.P., Galivanche, A.R., Bagi, P.S., Zogg, C.K., Rubin, L.E., Grauer, J.N., 2018. Increased complications in geriatric patients with a fracture of the hip whose postoperative weight-bearing is restricted: An analysis of 4918 patients. Bone Jt. J. 100B, 1377–1384. https://doi.org/10.1302/0301-620X.100B10.BJJ-2018-0489.R1

Panagiotopoulos, E., Fortis, A.P., Millis, Z., Lambiris, E., Kostopoulos, V., Vellios, L., 1994. Pattern of screw loosening in fractures fixed with conventional and functional plates. Injury 25, 515–517. https://doi.org/10.1016/0020-1383(94)90092-2

Pletka, J.D., Marsland, D., Belkoff, S.M., Mears, S.C., Kates, S.L., 2011. Biomechanical Comparison of 2 Different Locking Plate Fixation Methods in Vancouver B1 Periprosthetic Femur Fractures. Geriatr. Orthop. Surg. Rehabil. 2, 51–55. https://doi.org/10.1177/2151458510397609

Randelli, F., Pace, F., Priano, D., Giai Via, A., Randelli, P., 2018. Re-fractures after periprosthetic femoral fracture: A difficult to treat growing evidence. Injury 49, S43–S47. https://doi.org/10.1016/j.injury.2018.09.045

Raschke, M.J., Schliemann, B., 2020. Periprosthetic fractures. Chirurg 91, 793. https://doi.org/10.1007/s00104-020-01269-6

Reid, I.R., 2020. A broader strategy for osteoporosis interventions. Nat. Rev. Endocrinol. 16, 333–339. https://doi.org/10.1038/s41574-020-0339-7

Rikkonen, T., Sirola, J., Salovaara, K., Tuppurainen, M., Jurvelin, J.S., Honkanen, R., Kröger, H., 2012. Muscle strength and body composition are clinical indicators of osteoporosis. Calcif. Tissue Int. 91, 131–138. https://doi.org/10.1007/s00223-012-9618-1

Schileo, E., Dall'Ara, E., Taddei, F., Malandrino, A., Schotkamp, T., Baleani, M., Viceconti, M., 2008. An accurate estimation of bone density improves the accuracy of subject-specific finite element models. J. Biomech. 41, 2483–2491. https://doi.org/10.1016/j.jbiomech.2008.05.017

Schindelin, J., Arganda-Carrera, I., Frise, E., Verena, K., Mark, L., Tobias, P., Stephan, P., Curtis, R., Stephan, S., Benjamin, S., Jean-Yves, T., Daniel, J.W., Volker, H., Kevin, E., Pavel, T., Albert, C., 2009. Fiji - an Open platform for biological image analysis. Nat. Methods 9. https://doi.org/10.1038/nmeth.2019.Fiji

Shah, S., Kim, S.Y.R., Dubov, A., Schemitsch, E.H., Bougherara, H., Zdero, R., 2011. The biomechanics of plate fixation of periprosthetic femoral fractures near the tip of a total hip implant: Cables, screws, or both? Proc. Inst. Mech. Eng. Part H J. Eng. Med. 225, 845–856. https://doi.org/10.1177/0954411911413060

Sidler-Maier, C.C., Waddell, J.P., 2015. Incidence and predisposing factors of periprosthetic proximal femoral fractures: a literature review. Int. Orthop. 39, 1673–1682. https://doi.org/10.1007/s00264-015-2721-y

Sinaki, M., Brey, R.H., Hughes, C.A., Larson, D.R., Kaufman, K.R., 2005. Balance disorder and increased risk of falls in osteoporosis and kyphosis: Significance of kyphotic posture and muscle strength. Osteoporos. Int. 16, 1004–1010. https://doi.org/10.1007/s00198-004-1791-2

Speirs, A.D., Heller, M.O., Duda, G.N., Taylor, W.R., 2007a. Physiologically based boundary conditions in finite element modelling. J. Biomech. 40, 2318–2323. https://doi.org/10.1016/j.jbiomech.2006.10.038

Speirs, A.D., Heller, M.O., Duda, G.N., Taylor, W.R., 2007b. Physiologically based boundary conditions in finite element modelling. J. Biomech. 40, 2318–2323. https://doi.org/10.1016/j.jbiomech.2006.10.038

Sugiura, T., Horiuchi, K., Sugimura, M., Tsutsumi, S., 2000. Evaluation of threshold stress for bone resorption around screws based on in vivo strain measurement of miniplate. J. Musculoskelet. Neuronal Interact. 1, 165–70.

Taddei, F., Schileo, E., Helgason, B., Cristofolini, L., Viceconti, M., 2007. The material mapping strategy influences the accuracy of CT-based finite element models of bones: An evaluation against experimental measurements. Med. Eng. Phys. 29, 973–979. https://doi.org/10.1016/j.medengphy.2006.10.014

Takahashi, D., Noyama, Y., Asano, T., Shimizu, T., Irie, T., Terkawi, M.A., Iwasaki, N., 2021. Finite element analysis of double-plate fixation using reversed locking compression-distal femoral plates for Vancouver B1 periprosthetic femoral fractures. BMC Musculoskelet. Disord. 22, 1–8. https://doi.org/10.1186/s12891-021-04152-5

Taylor, M., Tanner, I., Freemant, M., Yettram, A., 1996. Elsevicr Science Lrd for IPEMB Stress and strain distribution within the intact femur: compression or bending? Med. Eng. Hys 18, 122–131.

Varga, P., Schwiedrzik, J., Zysset, P.K., Fliri-Hofmann, L., Widmer, D., Gueorguiev, B., Blauth, M., Windolf, M., 2016. Nonlinear quasi-static finite element simulations predict in vitro strength of human proximal femora assessed in a dynamic sideways fall setup. J. Mech. Behav. Biomed. Mater. 57, 116–127. https://doi.org/10.1016/j.jmbbm.2015.11.026

Wang, K., Kenanidis, E., Miodownik, M., Tsiridis, E., Moazen, M., 2019. Periprosthetic fracture fixation of the femur following total hip arthroplasty: A review of biomechanical testing – Part II. Clin. Biomech. 61, 144–162. https://doi.org/10.1016/j.clinbiomech.2018.12.001

Warren, J., Sundaram, K., Anis, H., McLaughlin, J., Patterson, B., Higuera, C.A., Piuzzi, N.S., 2019. The association between weight-bearing status and early complications in hip fractures. Eur. J. Orthop. Surg. Traumatol. 29, 1419–1427. https://doi.org/10.1007/s00590-019-02453-z

Weinans, H., Huiskes, R., Grootenboer, H.J., 1992. Effects of material properties of femoral hip components on bone remodeling. J. Orthop. Res. 10, 845–853. https://doi.org/10.1002/jor.1100100614

Weinhandl, J.T., Irmischer, B.S., Sievert, Z.A., 2017. Effects of Gait Speed of Femoroacetabular Joint Forces. Appl. Bionics Biomech. 2017. https://doi.org/10.1155/2017/6432969